ADVANCED FUNCTIONAL MATERIALS
www.afm-journal.de

Spectrally Tunable 2D Material-Based Infrared Photodetectors for Intelligent Optoelectronics

Junheon Ha, Yingshan Ma, Yong Nam An, Sung-Un An, Hyeon Hak Jung, Suvi-Tuuli Varjamo, Jiwon Yoo, Junho Min, Hanvit Kim, Faisal Ahmed, Sang Hoon Chae, Young Min Song, Weiwei Cai, Tawfique Hasan, Zhipei Sun, Dong-Ho Kang, Hyeon-Jin Shin,* Yunyun Dai,* and Hoon Hahn Yoon**

The evolution of intelligent optoelectronic systems is driven by artificial intelligence (AI). However, their practical realization hinges on the ability to dynamically capture and process optical signals across a broad infrared (IR) spectrum. Central to this capability are IR photodetectors (PDs) based on 2D materials (2DMs), which offer tunable spectral responsivity and wavelength-resolved multiparameter optical information. This review examines the fundamental mechanisms and design strategies that enable spectral tunability at the frontier of 2DM-based IR PDs, elucidating how they offer unique opportunities to tailor spectral responses across a broad wavelength range through symmetry-breaking induced by geometric (geometrically tunable spectral engineering) and electric-field (electrically tunable spectral engineering) effects. These approaches collectively enable simultaneous optimization of spectral tunability and sensitivity without compromising wavelength coverage, speed, power efficiency, or scalability, while also providing polarization sensitivity, multiband detection, and self-powered operation for edge-integrated AI platforms, including computational spectroscopy, artificial vision, computing, and communications. This review outlines the key processes and integration requirements for scalable manufacturing, which are essential for establishing spectrally tunable 2DM-based IR PDs as core building blocks of intelligent optoelectronics. Ultimately, the development of spectrally tunable 2DM-based IR PDs will transform intelligent optoelectronic platforms for or with AI

1. Introduction

Broadband photodetectors (PDs), which can detect invisible information, particularly covering the infrared (IR) spectrum from 0.75 to 15 μm, play a pivotal role in various applications, including spectroscopy, thermography, remote sensing, automotive driving assistance, industrial inspection, optical communication, security, environmental monitoring, and military defense. With the advent of the artificial intelligence (AI) era, the development of intelligent optoelectronics, combined with IR application technologies, has become increasingly important. As illustrated in **Figure 1**, excellent examples of intelligent optoelectronics include computational spectroscopy,[1, 2] artificial vision,[3–8] computing,[9–13] and communication.[14–16]

Although AI emerges as a transformative enabler, leveraging computational techniques to overcome inherent physical barriers, a key feature of hardware systems is the ability of a PD to tune its spectral responsivity across different wavelength bands

J. Ha, Y. N. An, S.-U. An, H. H. Jung, J. Yoo, J. Min, D.-H. Kang, H.-J. Shin, H. H. Yoon
Department of Semiconductor Engineering
Department of Electrical Engineering and Computer Science
Gwangju Institute of Science and Technology
Gwangju 61005, Republic of Korea
E-mail: donghokang@gist.ac.kr; hyeonjin.shin@gist.ac.kr; hoonhahnyoon@gist.ac.kr

The ORCID identification number(s) for the author(s) of this article can be found under https://doi.org/10.1002/adfm.202519542

DOI: 10.1002/adfm.202519542

Y. Ma, Y. Dai
School of Integrated Circuits and Electronics
Beijing Institute of Technology
Beijing 100081, China
E-mail: yunyundai@bit.edu.cn

Y. Dai
Advanced Research Institute of Multidisciplinary Sciences
Beijing Institute of Technology
Beijing 100081, China

S.-T. Varjamo
VTT Technical Research Centre of Finland
Tietotie 3, Espoo 02150, Finland

H. Kim
Digital Biomedical Research Division
Electronics and Telecommunications Research Institute
Daejeon 34129, Republic of Korea

on a chip or obtain wavelength-specific multiple optical information. For example, computational spectroscopy reconstructs a spectrum by computing the trained tunable spectral response of a PD, and artificial vision extracts insightful spectral information for inspection and analysis by processing multi-dimensional spectral data captured by a spectrally tunable PD.

However, conventional IR PDs have limited utility in intelligent optoelectronics due to a fixed spectral response stemming from the intrinsic material properties and integration constraints, which impose critical limitations such as cryogenic cooling requirements, rigid spectral profiles, and minimal post-fabrication tunability. These constraints could be overcome by IR PDs based on two-dimensional materials (2DMs), which offer unparalleled advantages, including spectral tunability and dynamic reconfigurability, making them ideal hardware platforms for AI-integrated optoelectronics. 2DM-based IR PDs create a virtuous synergetic cycle, unlocking unprecedented adaptability in IR sensing through AI algorithms and providing the physical foundation for next-generation AI-driven functionalities.

This review provides a guide to the advantages of 2DMs by exploring their underlying physics and key performance metrics of state-of-the-art IR PDs. Here, we present a comprehensive overview of various engineering strategies for implementing their pixel-by-pixel tunable spectral response on a chip, along with scalable manufacturing approaches. Finally, we discuss intelligent optoelectronic applications of 2DM-based IR PDs, including those for or in conjunction with AI, such as computational spectroscopy, artificial vision, computing, and communication.

1.1. Overview of Spectrally Tunable IR PDs

A tunable spectral response indicates that an IR PD can tune spectral responsivity over a broad wavelength range. When such tunability is achieved in situ in the active region of a PD, it can be defined as in situ tunable spectral response, which can further advance intelligent optoelectronics.[1–16]

Most typical IR PDs have been optimized to suppress dark current and improve detection performance. For example, commercial IR PDs require cryogenic cooling to mitigate thermal noise and enhance IR sensitivity with particular device architectures, such as InGaAs quantum cascade[17, 18] and InAs/InAsSb strained superlattice.[19] However, the complex fabrication steps and the need for refrigeration equipment significantly complicate their practical integration, thereby raising overall manufacturing and system costs. HgCdTe photoconductors and photodiodes enable high-performance IR detection at temperatures down to 200 K, but have the disadvantages of high material cost, limited array size, and device fragility.[20, 21] Above all, the band alignment of HgCdTe cannot be tuned after device fabrication, hindering tunable spectral engineering on a chip. Although microbolometers and thermopiles, which rely on thermal changes rather than direct photodetection, can eliminate the need for cooling, they generally suffer from slow response times and a limited spectral range, which constrains their tunable spectral response.[22–24] IR PDs integrated with plasmonic and nanophotonic devices, such as metasurface, cavity, and antenna, have been presented with enhanced responsivity of specific IR regimes. Still, they are difficult to tune in situ on a chip, and each wavelength requires a dedicated footprint, leading to array integration and high process costs.

In short, spectral tuning of conventional IR PDs typically requires bulk band structure engineering or complex module integration, which increases production costs and poses integration challenges. Tunable spectral engineering of 2DM-based IR PDs is a powerful game-changer that improves system efficiency and reduces costs. For example, the spectral response is electrically tunable through 2DMs on a chip via electrical gating or biasing, even after device fabrication,[25–31] allowing a single PD to in situ tune their response across multiple spectral bands without relying on optical or mechanical components, such as PD/filter arrays, waveguide/modulator-integrated components, and rotational gratings. These are essential for applications requiring in situ spectral tunability, such as in-pixel spectral imaging, adaptive sensing, in-sensor computing, and wavelength-division multiplexed optical interconnects.

1.2. IR Detection Mechanisms

IR PDs employ various IR detection mechanisms that convert incident IR light into an electrical signal, typically a photocurrent, depending on their material combination and device structure.[32] In general, the IR detection mechanisms can be broadly categorized into photon-based and thermal-based mechanisms. Photon-based detection includes mechanisms such as photoconductive effect (PCE), photovoltaic effect (PVE), and photogating effect (PGE). Thermal-based detection encompasses the photo-thermoelectric effect (PTE), the photo-bolometric effect (PBE), and the photo-pyroelectric effect (PPE), as summarized in **Figure 2**. A variety of IR detection mechanisms can be combined to produce a synergistic effect.[33]

F. Ahmed, Z. Sun
QTF Centre of Excellence
Department of Electronics and Nanoengineering
Aalto University
Espoo 02150, Finland
S. H. Chae
School of Electrical and Electronic Engineering
School of Materials Science and Engineering
Nanyang Technological University
Singapore 639798, Singapore
Y. M. Song
School of Electrical Engineering
Korea Advanced Institute of Science and Technology
Daejeon 34141, Republic of Korea
Y. M. Song, H.-J. Shin
GIST InnoCORE AI-Nano Convergence Institute for Early Detection of Neurodegenerative Diseases
Gwangju Institute of Science and Technology
Gwangju 61005, Republic of Korea
W. Cai
School of Mechanical Engineering
Shanghai Jiao Tong University
Shanghai 200240, China
T. Hasan
Cambridge Graphene Centre
University of Cambridge
Cambridge CB3 0FA, UK

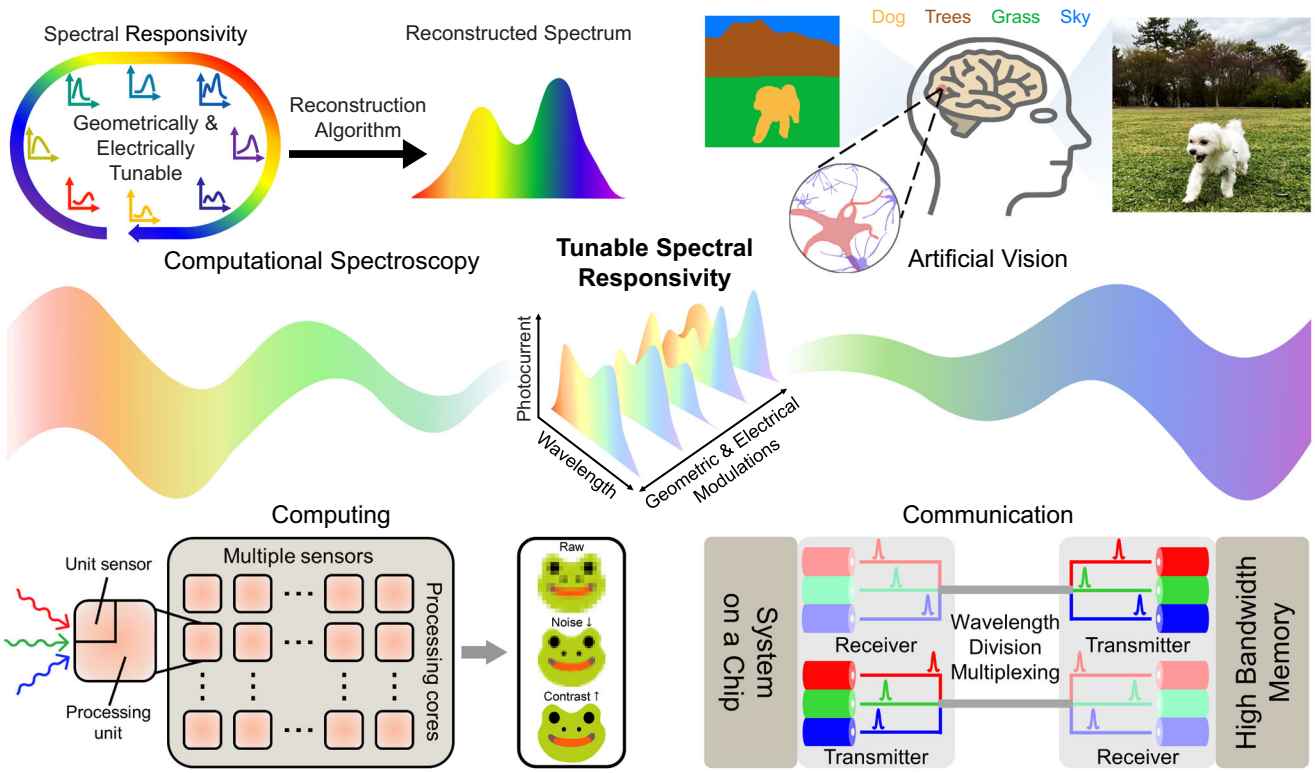

Figure 1. Intelligent optoelectronic applications enabled by tunable spectral engineering of 2DM-based IR PDs. The schematic highlights the benefits of spectrally tunable photoresponse in 2DM-based IR PDs, along with their applications in computational spectroscopy, artificial vision, computing, and communications.

1.2.1. Photoconductive Effect

Figure 2a depicts PCE, showing that photon absorption generates additional electron–hole pairs in the semiconductor, thereby increasing the electrical conductivity. This change in electrical conductivity $\Delta\sigma$ can be expressed with the elementary charge constant q, the carrier mobility of the channel μ, and the density variation in free carriers Δn.

$$\Delta\sigma = q\mu\Delta n\ [\mathrm{S}\cdot\mathrm{m}^{-1}] \tag{1}$$

An external bias separates the photogenerated carriers, contributing to the photocurrent i_{ph}.[34] Under illumination, $\Delta\sigma$ can be converted to i_{ph} by the bias voltage V, where L is the channel length and A is the cross-sectional area perpendicular to the current flow.

$$i_{ph} = \frac{VA}{L}\Delta\sigma\ [\mathrm{A}] \tag{2}$$

1.2.2. Photovoltaic Effect

As illustrated in Figure 2b, the PVE refers to the generation of a voltage in a material under light illumination, driven by an internal electric field. When a p-type and an n-type semiconductor are brought into contact, majority charge carriers (electrons in n-type and holes in p-type) diffuse across the junction. This diffusion creates a region depleted of free charge carriers, called the depletion region, which establishes an electric field and forms a built-in potential.

The open-circuit voltage (V_{oc}) is the voltage measured at the terminals of a PVE-type PD when no current is flowing (i.e., an open circuit). The short-circuit current (i_{sc}) is the current through a PVE-type PD when its terminals are shorted (i.e., zero voltage). These parameters are crucial for understanding and characterizing the performance of PVE-type PDs, especially for solar cell applications.

1.2.3. Photogating Effect

The PGE is a phenomenon in which photoexcited electron–hole pairs become trapped in localized states, often associated with impurities or vacancies within the semiconductor. These trapped charges change the electrical properties of PGE-type PDs.[35] As shown in Figure 2c, if the holes are trapped near the band edge and act as an additional local gate, these carriers induce an electric field effect that shifts the Fermi level, which, in turn, increases the electron density. This reduces channel resistance, allowing more photocurrent to flow through the device. As a result, the photoresponse is governed by the dynamics of these trap states. The high responsivity associated with PGE typically comes at the expense of low response speed, as prolonged carrier trapping can delay carrier release and collection.[36] However,

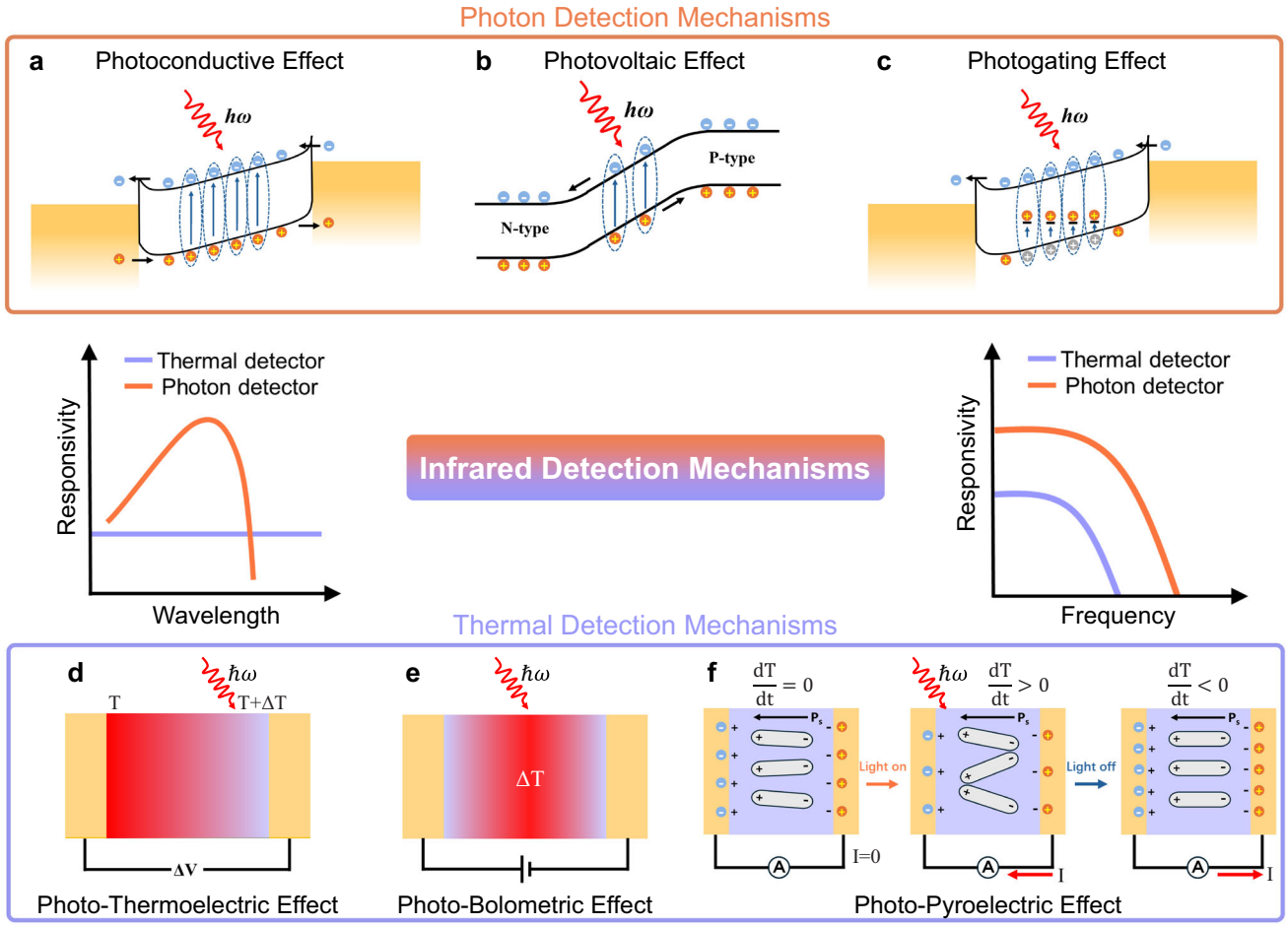

Figure 2. Schematic illustration of IR detection mechanisms. Detectors can be classified into photon detectors and thermal detectors according to the detection mechanism. Photon-based types include PCE, PVE, and PGE, while thermal-based types comprise PTE, PBE, and PPE. Photon-based PDs are usually wavelength-dependent and operate over a broad wavelength range. In contrast, thermal-based PDs are intrinsically wavelength-independent, with no cutoff in the wavelength range.

this trade-off can be mitigated by bias-tunable operation, which allows dynamic control of the trapping and detrapping processes.

1.2.4. Photo-Thermoelectric Effect

The PTE refers to the generation of a potential difference when localized temperature gradients are induced by incident light across different regions of a material, as illustrated in Figure 2d. In this process, charge carriers respond to the thermal gradient, producing a potential difference. This leads to the voltage V_{PTE} across the two regions, which is defined by the Seebeck coefficients of each region, S_1 and S_2, and the temperature difference ΔT between them.

$$V_{PTE} = (S_1 - S_2) \triangle T \text{ [V]} \tag{3}$$

The Seebeck coefficient is intrinsically linked to the material's electrical conductivity and quantifies the thermoelectric response to a temperature gradient. The Mott equation represents this relation, where k_B is the Boltzmann constant, T_e is the electron temperature, e is the elementary charge, σ is the electrical conductivity, and ϵ_F is the Fermi energy.

$$S = -\frac{\pi^2 k_B^2 T_e}{3e\sigma} \frac{\partial \sigma}{\partial \epsilon_F} [\text{V} \cdot \text{K}^{-1}] \tag{4}$$

1.2.5. Photo-Bolometric Effect

Figure 2e depicts the PBE, which refers to a phenomenon in which the illumination of light leads to photon absorption, increasing the electron temperature and consequently changing the electrical resistance of the material. The PBE-type PDs based on 2DMs can be used to determine the power of incident electromagnetic radiation, such as IR illumination. The PBE-type PDs must operate under external bias and thermal resistance R_h, where T is the temperature of the material and P is the incident light power. R_h measures the opposition to the heat current in a material, indicating how much temperature

difference is required to transfer a unit of heat current through the material.

$$R_h = \frac{dT}{dP}\ [\mathrm{K}\cdot\mathrm{W}^{-1}] \tag{5}$$

1.2.6. Photo-Pyroelectric Effect

As illustrated in Figure 2f, PPE is a phenomenon in which a material with spontaneous polarization changes its polarization due to heat when exposed to light and can be commonly observed in ferroelectric materials. When they absorb IR radiation, their polarization changes over time as temperature changes.[37, 38] This temporal change in polarization generates a pyroelectric current i_{pyro} even in the absence of an external bias voltage, where p is the pyroelectric coefficient and A is the cross-sectional area of the electrode. Here, dT/dt represents the temporal rate of change in temperature in the material.

$$i_{pyro} = pA\frac{dT}{dt}\ [\mathrm{C}\cdot\mathrm{s}^{-1}] \tag{6}$$

1.3. Figure of Merit of IR PDs

The performance and versatility of IR PDs are governed by several critical parameters that determine their suitability across diverse domains of intelligent optoelectronic applications. Here, we highlight the physical basis, formulation, and noise-related performance metrics, which are crucial for understanding the nature of the underlying noise that determines them, especially for IR PDs.[39, 40]

1.3.1. Noise Sources in IR PDs

Johnson–Nyquist (or thermal) noise current i_{th} originates from the thermally induced random motion of carriers in resistive components, where k_B is the Boltzmann constant, T is the temperature, Δf is the bandwidth, R_L is the load resistor. This expression can be alternatively understood via its corresponding power spectral density $S_{th}(f)$. Note that thermal noise occurs when current flows through the resistive channel, so it can be mitigated by lowering parasitic resistance elements or normalizing the backscatter signal at low temperatures.

$$i_{th} = \sqrt{\frac{4k_BT\Delta f}{R_L}}\ [\mathrm{A}] \tag{7}$$

$$S_{th}(f) = \frac{4k_BT}{R_L}\ [\mathrm{A}^2\cdot\mathrm{Hz}^{-1}] \tag{8}$$

Shot noise current i_{shot} arises from the statistical random fluctuation, such as the discrete charge carriers under bias or the discrete nature of light like the random arrival of photons into PDs, where q denotes the electric charge, i_d is the dark current, and i_{ph} is the photocurrent. This expression can also be interpreted in terms of the corresponding power spectral density $S_{sh}(f)$, assuming a white shot noise spectrum. A balanced photodetection method can be used to reduce or cancel random fluctuations in i_{ph} by using two matched PDs, separated by a delay, to measure the same optical signal split into two paths. By subtracting the photocurrents from the two PDs, common-mode noise, including shot noise, can be effectively canceled out.

$$i_{shot} = \sqrt{2q(i_d + i_{ph})\Delta f}\ [\mathrm{A}] \tag{9}$$

$$S_{sh}(f) = 2q(i_d + i_{ph})\ [\mathrm{A}^2\cdot\mathrm{Hz}^{-1}] \tag{10}$$

Flicker noise dominates at low frequencies and scales approximately as $S_{1/f}(f)\propto 1/f^{\gamma}$ with $\gamma \approx 1$. Since flicker noise arises from both carrier-number fluctuations due to trapping/detrapping in defects and mobility fluctuations associated with material nonuniformity, it is intrinsic to semiconductor devices, including PDs and readout electronics, where amplifiers typically contribute their own $1/f$ terms.[41] In the time domain, individual traps produce discrete two-level switching (random telegraph signal, RTS) governed by Shockley–Read–Hall capture/emission kinetics. In the frequency domain, a single RTS yields a Lorentzian spectrum, and a broad distribution of time constants superposes to yield the $1/f$ behavior.[42] RTS time constants depend on trap energy/position, carrier density, temperature, and electric field. Flicker noise can stem from surfaces, interfaces (including border traps), contacts, and bulk states, and it coexists with thermal and shot noise. To mitigate flicker noise, the signal is often modulated above the corner frequency f_c, where $S(f_c)$ equals the white noise floor, and then synchronously detected by a lock-in amplifier. Furthermore, chopper-stabilized or auto-zero amplifiers are widely used to suppress noise originating from the amplifier.

To ensure reproducible and fair comparisons, it is essential to understand the noise sources of a specific IR PD and extract key performance parameters at the same operating bias, temperature, and bandwidth, which must be reported along with the noise power spectral density $S(f)$, the integrated root-mean-square noise over the measurement bandwidth, and the $1/f$ corner frequency.

$$S_{1/f}(f) \propto \frac{1}{f^{\gamma}}\ [\mathrm{A}^2\cdot\mathrm{Hz}^{-1}] \tag{11}$$

1.3.2. Performance Metrics in IR PDs

Photoconductive gain G is an essential factor in R_λ, which quantifies the number of charge carriers collected per incident photon and is given by the ratio of $\tau_{trapped}$ to $\tau_{transit}$, where $\tau_{trapped}$ and $\tau_{transit}$ are the lifetime of the trapped carrier and the carrier transit time, respectively. Thus, G is 1 when the absorption of a single photon leads to the generation of an electron–hole pair. If carriers do not contribute to i_{ph} due to the electron–hole recombination process, G is reduced. A substantial G can be achieved when photogenerated carriers become trapped and modulate the channel conductivity through electrical gating.

$$G = \frac{\tau_{trapped}}{\tau_{transit}} \tag{12}$$

Response speed indicates how quickly a PD converts incident light to i_{ph} and is determined by carrier mobility, built-in

potential, device architecture, and signal-processing circuits. Response time is defined by the rise and fall times, τ_{rise} and τ_{fall} respectively, are measured as the time it takes for the output current to change from 10 % to 90 % and 90 % to 10 % of the final value based on changes in light input. Faster response speeds and shorter response times are desirable for a PD to follow temporal fluctuations in light intensity, making it suitable for applications that require high temporal resolution and capture transient optical signals with greater precision. Photocarrier trapping mechanisms, such as PGE, enhance R_λ, while trapping and detrapping processes delay the response time and contribute to RTS noise. Therefore, even if a higher value of R_λ is generally desirable, R_λ must be evaluated together with the noise parameters to assess the overall quality of a PD.

Note that bandwidth Δf is the frequency range over which a PD can respond with a meaningful output signal. It is typically defined by the –3 dB point, where the output signal falls to $1/\sqrt{2}$ (≈ 0.707) of its maximum value. This parameter is closely related to the temporal response characteristics of a PD. The broader Δf implies a faster response to rapid variations in incident optical signals, but it gives rise to a trade-off relation. Broad Δf leads to an expansion of the noise power, resulting in a higher *NEP* and, consequently, a reduction in D^*. The cutoff frequency f_{-3dB} refers to the frequency that serves as the reference point for Δf, and is determined by $\tau_{transit}$, R_L, and load capacitance C_L.

$$f_{-3dB} = \sqrt{\left(\frac{3.5}{2\pi\tau_{transit}}\right)^2 + \left(\frac{1}{2\pi R_L C_L}\right)^2}\ [\mathrm{Hz}] \tag{13}$$

At a specific incident light wavelength λ, responsivity R_λ essentially represents how well a PD converts light into an electrical signal, defined as i_{ph} generated per incident optical power P_λ.[43] R_λ can be expressed by external quantum efficiency η_e, the ratio of the number of charge carriers collected by a PD to the number of incident photons, indicating how efficiently a PD converts photons into electron–hole pairs and then collects those carriers. Note that the frequency dependence of responsivity R_f can also be considered due to the correlation between the Δf and the temporal response of a PD. For a linear-response PD, the R_f is governed by the frequency of the light source f, the steady-state responsivity R_0, and $\tau_{transit}$.

$$R_\lambda = \frac{i_{ph}}{P_\lambda} = \eta_e \frac{e\lambda}{hc}\ [\mathrm{A \cdot W^{-1}}] \tag{14}$$

$$R_f = \frac{R_0}{\sqrt{1 + (2\pi f \tau_{transit})^2}}\ [\mathrm{A \cdot W^{-1}}] \tag{15}$$

Signal-to-noise ratio *SNR* is described as the signal power ($\propto i_{ph}^2$) per the total noise power ($\propto i_{noise}^2 = i_{shot}^2 + i_{th}^2 + i_{others}^2$), where i_{others} denotes low-frequency noise.[44] Thus, *SNR* is an indicator of the signal relative to the total noise, and a higher value of *SNR* in PD implies a PD with low noise and high sensitivity. If we assume that the dominant noise source is the shot noise of i_d ($i_{noise} \approx \sqrt{2qi_d\Delta f}$), we can simplify *SNR* by considering that the shot noise prevails ($i_{shot} >> i_{th}$) and the optical power is low ($i_d >> i_{ph} = i_{noise}\sqrt{SNR}$).

$$SNR = \frac{i_{ph}^2}{i_{noise}^2} = \frac{i_{ph}^2}{2q(i_d + i_{ph})\Delta f + \frac{4k_B T\Delta f}{R_L} + i_{others}^2} \approx \frac{i_{ph}^2}{2qi_d\Delta f} \tag{16}$$

Noise equivalent power *NEP* is defined as the minimum incident optical power required to produce an *SNR* of 1, where $i_{ph} = i_{noise}$ in a bandwidth of 1 Hz. In other words, a lower *NEP* indicates a more sensitive PD, capable of detecting weaker signals, which is critical in low-level signal applications such as thermal imaging, astronomy, and biosensing.[44] Similarly, if we assume that the shot noise of i_d contributes mainly to the overall noise in a PD, a higher i_d leads to a higher *NEP*, degrading the sensitivity of a PD.

$$NEP = \frac{P_\lambda}{SNR\sqrt{\Delta f}} = \frac{i_{noise}}{R_\lambda\sqrt{SNR}\sqrt{\Delta f}} \approx \frac{\sqrt{2qi_d}}{R_\lambda\sqrt{SNR}}\ [\mathrm{W \cdot Hz^{-0.5}}] \tag{17}$$

Specific detectivity D^* is the reciprocal of *NEP*, normalized per square root of the active area A of a PD and a bandwidth Δf, providing a way to assess the ability of a PD to distinguish weak signals from background noise as a crucial comparative basis for PDs.[44] D^* is commonly used as a benchmark metric for comparing the performance of different PDs. In essence, understanding the various noise sources and their impact on D^* is crucial for designing and optimizing highly sensitive IR PDs, particularly for long-range IR communication or low-light imaging.

$$D^* = \frac{\sqrt{A}}{NEP} = \frac{R_\lambda\sqrt{A}\sqrt{SNR}\sqrt{\Delta f}}{i_{noise}} \approx R_\lambda\frac{\sqrt{A}\sqrt{SNR}}{\sqrt{2qi_d}}$$
$$[\mathrm{cm \cdot Hz^{0.5} \cdot W^{-1}\ or\ Jones}] \tag{18}$$

The shot-noise-limited assumption is valid only if a PD has internal gain, such as a photomultiplier or avalanche photodiode, so the shot noise exceeds the thermal (or other) noise at the detection threshold by a significant margin.[39, 40, 45] In practice, especially in 2DM-based back-gated phototransistors, i_{noise} is often dominated by flicker noise due to inevitable traps on the surface of the amorphous dielectric substrate or at the interface in contact with electrodes, which fluctuates the 2DM channel even if the surface 2DM is almost defect-free and dangling-bond-free.[46–48] Therefore, for a fair evaluation of D^*, each component of i_{noise} should be evaluated and *NEP* derived accordingly. Neglecting noise contributions other than shot noise can sometimes lead to a significant overestimation of the performance of a PD, including *NEP* and D^*, which may result in incorrect comparisons with the literature.

Dynamic range *DR* is an indicator of the range in which a PD can accurately measure light intensity and is defined as the ratio of the maximum light power P_{max} before photocurrent saturation to the minimum light power P_{min} that a PD can detect, which is closely related to *NEP*. A high *DR* allows a PD to function

stably across a broad range of light intensities, ranging from dim to bright environments.

$$DR = 20\log\left(\frac{P_{\max}}{P_{\min}}\right) \tag{19}$$

The wavelength range denotes the effective wavelength range that spans from λ_{min} to λ_{max} to which a PD can generate a measurable photoresponse, typically determined by the band structure and absorption spectrum of the materials in the active region.

In general, materials with narrower bandgaps can detect photons with longer wavelengths (lower energy), thereby extending their detection range into the MIR or FIR. However, narrow-bandgaps also lead to higher intrinsic carrier concentrations, which significantly increase i_d and, in turn, raise *NEP*, ultimately reducing *D**. The trade-off between extending the wavelength range and enhancing sensitivity presents a fundamental challenge in IR PD design.

1.4. Conventional IR-Sensitive Materials and Their PDs

Although some emerging materials exhibit strong IR absorption at specific wavelengths, their spectral response remains fixed due to their inherent band structures, which determine their electrical and optical properties.[49–59] Moreover, they exhibit reliability and stability concerns, which make them unsuitable for long-term applications in tunable IR PDs.

1.4.1. Semiconducting Organic Compounds

IR PDs based on semiconducting organic compounds rely on molecular electronic transitions. However, their spectral response is predetermined by the molecular composition and remains fixed after fabrication. They suffer from rapid environmental degradation, particularly when exposed to humidity and oxygen, resulting in a shorter operational lifetime. Their low charge-carrier mobility further reduces efficiency, leading to slower response times and higher noise levels. Recent advances have explored several strategies, such as molecular doping and interface engineering, to enhance stability and performance, yet achieving long-term operational reliability remains a significant challenge.[60]

1.4.2. Colloidal Quantum Dots

Colloidal quantum dots, such as HgTe and PbS, are promising for IR detection due to their size-dependent bandgap energy tunability resulting from quantum confinement.[61, 62] This quantum confinement allows the spectral response to be engineered during synthesis. However, post-fabrication spectral tunability remains challenging, as the bandgap is fixed once the quantum dots are synthesized. Moreover, PDs based on quantum dots suffer from surface trap states, oxidation, and charge-carrier recombination, leading to device instability and reduced efficiency. They require chemical modifications to alter their absorption spectra, posing significant challenges to spectral tunability while maintaining device stability. The difficulties further hinder their integration into large-scale, long-term, and stable IR detection systems, which require maintaining uniform dispersion and reliable charge transport.

1.4.3. Perovskite Composites

IR PDs based on perovskite composites that utilize sub-bandgap absorption and intraband transitions have attracted attention for their strong IR absorption and bandgap-tuning capabilities via compositional engineering.[63–65] Due to the relatively wide bandgap of hybrid organohalide perovskites, the photodetection bandwidth of organohalide-based PDs has been limited to the near-IR (NIR) regime.[63] On the contrary, hybrid organic-inorganic perovskite composites, such as $MAPbI_3$ and $CsPbBr_3$, have been reported to offer high quantum efficiency, making them attractive candidates for IR PDs.[64] Besides, mixed Sn-Pb perovskite composites-based PDs have achieved external quantum efficiency over 70 % around the NIR regime (from 0.75 to 1.4 μm) and extend response up to the mid-IR (MIR) regime (from 3 to 8 μm) by mixing narrow-bandgap semiconductors. Recently, the atomic-precision lift-off of ultrathin membranes without artificial release layers has enabled the high-throughput production of diverse, less than 10 nm-thick ultrathin perovskite membranes for cooling-free PDs that can cover a spectral range beyond 15 μm.[66] Despite these advantages, IR PDs based on perovskite composites still face challenges related to environmental stability, ionic migration, and performance degradation. In particular, their solution process is associated with significant stability issues due to their sensitivity to moisture, heat, and ion migration, leading to rapid degradation and hysteresis effects.[65] Overcoming these challenges requires advancements in passivation or encapsulation techniques, compositional modifications, and improved interfacial engineering to enhance longevity and operational reliability in photodetection applications, rendering them unsuitable for tunable spectral engineering.

2. 2DM-Based IR PDs

This section highlights 2DMs as a promising building block for high-performance, versatile, reliable, and tunable PDs, especially in the IR range, compared with commercial IR PDs (InGaAs quantum cascades, InAs/InAsSb strained superlattices, HgCdTe photoconductors and photodiodes, bolometers, thermopiles, etc.) and conventional IR-sensitive materials (semiconducting organic compounds, colloidal quantum dots, perovskite composites, etc.). Commercial IR PDs achieve excellent sensitivity but are still expensive to manufacture and typically require cooling systems for operation.[67, 68] Organic semiconductors suffer from rapid degradation and low mobility. Quantum dots have fixed bandgaps and are prone to trapping and oxidation.[69] Perovskites exhibit environmental and operational instabilities, particularly under moisture exposure, elevated temperatures, and ion migration.[70] In contrast, 2DMs exhibit high mobility, ambient stability, and tunable band structures through gating, stacking, or strain. Therefore, 2DM-based IR PDs can address the trade-off between sensitivity and speed in light detection,[71–86]

while offering giant gate tunability,[25–31] broadband photoresponse coverage,[49–59] bi-directional response,[13, 87–96] and integration compatibility with nanophotonics.[97–101] These advantages and versatility allow for tuning of the spectral response of 2DM-based IR PDs on a chip, opening up a wide range of potential applications.

2.1. Exotic Physics in IR-Sensitive 2DMs

The burgeoning field of 2DMs has revolutionized IR detection by providing an unprecedented platform for tailoring light-matter interactions at the atomic scale. Conventional materials are 3D bulk materials with out-of-plane dangling bonds at their surfaces, leading to surface states that degrade the diffusion length and the optoelectronic performance of IR PDs based on them. In contrast, 2DMs exhibit strong in-plane bonding but weak out-of-plane van der Waals (vdW) forces. They are atomically thin, have an atomically abrupt heterogeneous interface, exhibit quantum confinement effects, and are free of dangling bonds. Confined 2D surface states benefit from high carrier mobility, long lifetime, and long mean free path.[102–105] Thus, 2DMs and their vdW heterostructures are highly sensitive to external stimuli like gate voltage,[25–31] offering precise modulation of carrier density, band alignment, and interlayer coupling.[106–109] In addition, an exciton, a bound electron–hole pair, can move in 2DMs or across their heterostructures before its recombination with an opposite charge carrier or dissipation. These features are generally absent for 3D bulk materials, which has propelled 2DMs to the forefront of next-generation IR detection.

2.1.1. Exciton, Plasmon, and Phonon Polaritons

Exciton polariton, plasmon polariton, and phonon polariton represent three classes of hybrid light-matter quasiparticles that govern nanoscale optical phenomena in 2DMs.[110] Each quasiparticle arises from unique interactions between photons and material degrees of freedom, enabling tailored IR optoelectronics.[110]

A polariton is a bosonic quasiparticle formed through strong coupling between a photon and a collective excitation. Such collective excitation modes can arise from various physical phenomena, including lattice vibrations, metal-plasma oscillations, and excitons. When the dispersion relation of the electromagnetic wave strongly interacts with the dispersion characteristics of the material's internal resonance mode, an anti-crossing appears in the energy levels, leading to the formation of new hybridized normal modes. This hybrid state is the polariton, which possesses physical properties distinct from those of a pure photon or a pure material mode. In the strong coupling regime, photons do not propagate freely; instead, they hybridize with intrinsic material resonances to form polaritons. As a result, they exhibit intrinsic quantum effects in aspects such as energy dispersion characteristics and field confinement. These unique properties enable diverse applications and give rise to various types of polaritons, such as exciton-polaritons, plasmon-polaritons, and phonon-polaritons, depending on the coupled mode.

An exciton is a bound electron–hole pair that dominates light-matter interactions in semiconducting 2D systems like TMDs, which is formed when an electron is excited through an interband transition, leaving a hole in the valence band that binds with the excited electron via Coulomb attraction.[111] When the electron and hole are bound within the same layer, they form an intralayer exciton. In contrast, when they are bound across different layers, they form an interlayer or Moiré exciton. Intralayer excitons exhibit strong light-matter interactions and high PL efficiency, while interlayer and Moiré excitons, with spatially separated electrons and holes, offer advantages in terms of longer lifetime and electrical controllability. As shown in **Figure 3a**, beyond intralayer excitons, interlayer and Moiré excitons in vdW heterostructures (e.g., $MoSe_2/WSe_2$) bring long lifetimes (> ≈100 ns) and electrical tunability.[112, 113] Excitons can be stabilized by strong quantum confinement and reduced dielectric screening to exhibit exceptional binding energies (> ≈0.3 eV in monolayer MoS_2) at room temperature.[114] In the vicinity of the excitonic resonance, strong light absorption arises due to enhanced optical transitions, resulting in pronounced peaks in absorption and photoluminescence (PL) spectra.[115–118] When strong coupling between excitons and photons is established, exciton–polaritons form, producing Rabi splitting that separates the dispersion relation into upper and lower polariton branches with a distinct anti-crossing gap.[119] Exciton-polaritons bring about the light mass and mobility of photons while maintaining the strong interaction of excitons, leading to nonlinear phenomena such as blue shifts and refractive index changes. At high densities, their bosonic nature allows Bose-Einstein condensation, enabling coherent polariton lasers with ultralow thresholds.[120] Valley-selective optical selection rules enable the generation and manipulation of valley-polarized excitons with circularly polarized light, opening avenues toward valleytronic information processing.[121, 122] Their applications span from visible (VIS) to IR ranges, including ultrathin light emitters,[123] exciton-driven optical switches,[124, 125] and quantum emitters.[126]

A plasmon is a quantized collective oscillation of free charge carriers in a material. In 2D conductors, such as graphene, plasmonic oscillations strongly couple with incident photons, giving rise to plasmon polaritons that confine electromagnetic energy well below the diffraction limit, as illustrated in Figure 3b.[129] Unlike surface plasmon resonance in bulk metals, 2D plasmons exhibit tunable resonances by electrostatic gating and chemical doping, spanning the MIR to FIR, with extreme field confinement. For example, graphene plasmons compress light to 1/100th of its wavelength.[130] A plasmon-polariton is formed when plasmons strongly couple with photons, creating hybrid modes with photonic and electronic oscillation properties. However, due to momentum mismatch at the metal/dielectric interface, plasmons typically cannot directly couple with free-space photons. Momentum-matching techniques, such as prism or grating coupling, are employed to overcome this limitation. At plasmon-polariton resonance, a strong coupling occurs due to the anti-crossing of the dispersion curve. The spatial confinement of the electromagnetic field in hybrid mode enhances light-matter interactions, holding promise for highly sensitive biochemical sensing. In particular, stacking twisted bilayer graphene encapsulated with h-BN can improve the quality factor (Q_p > ≈970) compared to that of pristine graphene plasmon[131] and produce Moiré-modulated, topologically protected plasmon bands.[132, 133] Furthermore, 2D semiconductors

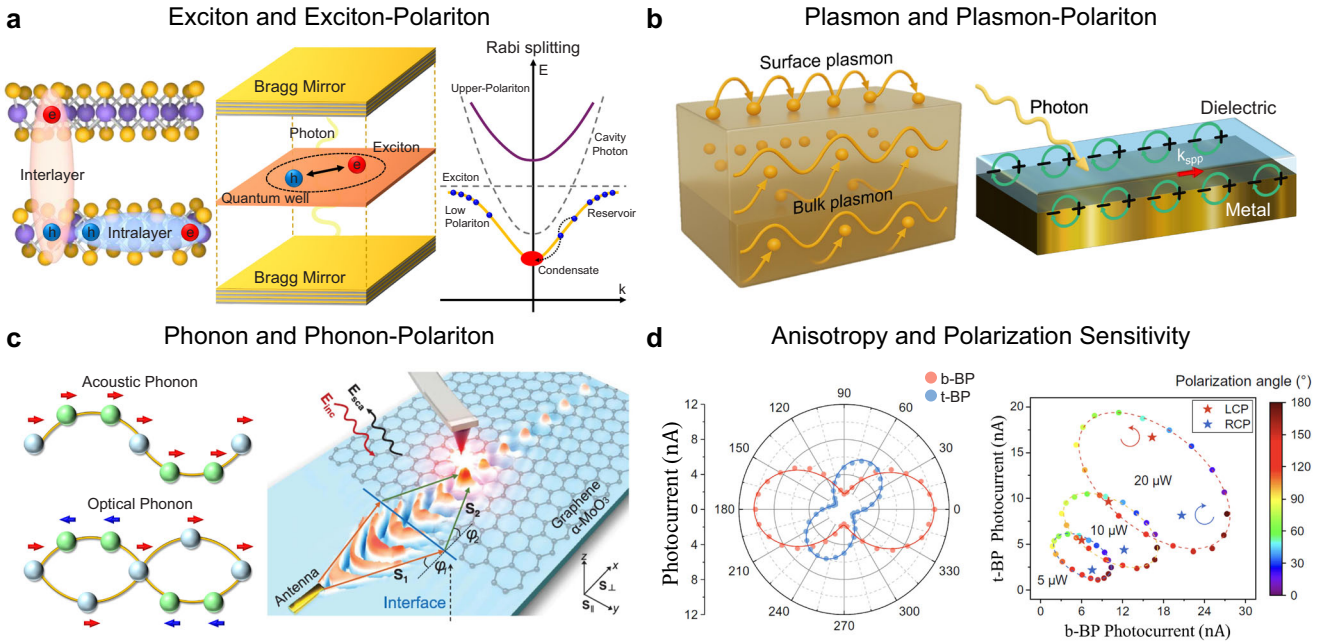

Figure 3. Diverse phenomena associated with photoresponse in 2DMs. a) Left: intralayer and interlayer excitons of a vdW heterostructure consisting of 2DMs. Center: strong coupling of the exciton-polariton in a microcavity. Right: Rabi-splitting induced by the exciton-polariton. b) Left: surface and bulk plasmons. Right: plasmon-polaritons at the metal/dielectric interface. c) Left: acoustic and optical phonons. Right: negative refraction of the phonon-polariton in a hyperbolic dielectric. d) Left: Polar plots of the polarized photocurrent generated in the two twisted b-P (b-BP: bottom b-P and t-BP: top b-P) as a function of the linear polarization angle. Right: Photocurrents generated in b-BP and t-BP under light illumination of different polarization angles. (c) Reproduced from ref. [127]. (Right) Copyright 2023, AAAS. (d) Reproduced from ref. [128]. Copyright 2022, AAAS under the CC BY-NC 4.0.

integrated with metallic plasmonic nanostructures have reduced optical loss and enhanced field confinement compared to conventional metallic gratings, leading to a higher photoelectric conversion efficiency.[134–138] Such properties in 2DMs enable a variety of IR applications, including subwavelength metamaterials for molecular fingerprinting,[139] enhanced PDs via plasmonic resonances,[140] and compact THz waveguides for on-chip signal processing.[141]

A phonon, a quantized collective vibration of atoms within a crystal lattice, fundamentally mediates thermal and vibrational properties. Phonons can be divided into acoustic phonons, where atoms move in the same direction, and optical phonons, where atoms move in opposite directions. Acoustic phonons are low-frequency sound modes and, being non-IR-active, do not hybridize with photons to form polaritons. In contrast, optical phonons strongly interact with light because their dispersion intersects with that of photons, especially within the reststrahlen band, where the permittivity becomes negative, enabling the formation of polaritons. Hyperconfined electromagnetic waves coupled to phonons in hyperbolic dielectrics, such as h-BN[142–146] and α-MoO_3,[127, 147] carry intense electric dipole moments in optical phonon, resonantly coupling with MIR light and enabling long-lived low-loss phonon polaritons to overcome the diffraction limit.[148, 149] Recently, electrostatic gating in α-MoO_3 demonstrated dynamic tuning of phonon polaritons for actively reconfigurable MIR nanophotonics.[127] As illustrated in Figure 3c, anisotropic permittivity in hyperbolic dielectrics results in the spectral regimes where different tensor components have opposite signs, giving rise to negative refraction of MIR light. Therefore, MIR phonon-polaritons unlock a wide range of optical and thermal applications, including super-resolution IR imaging, signal processing, thermal transport control, heat management at the nanoscale, highly sensitive molecular sensing, and nanophotonic integrated circuits.[127, 148, 149]

2.1.2. Anisotropy and Polarization Sensitivity

The anisotropic nature of 2DMs, arising from their low-symmetry crystal lattices and lattice-directional-dependent electronic or optical properties, has unlocked unprecedented opportunities in polarization-resolved photodetection.[150–153] Unlike conventional isotropic semiconductors, anisotropic 2DMs, such as b-P,[154–158] ReS_2[159], $GeAs_2$,[160] and GeSe[161] exhibit distinct directional disparities in their ultrathin atomic arrangements, leading to orientation-dependent band structures, effective carrier masses, and absorption coefficients. These anisotropies manifest as dichroic light-matter interactions, in which linearly polarized light with specific electric-field orientations selectively excites electronic transitions along crystallographic axes.[162] For instance, b-P demonstrates an eightfold difference in absorption between its armchair and zigzag directions due to anisotropic lattice geometry.[163] This intrinsic polarization selectivity enables miniaturized PDs that can directly decode the polarization state of light without requiring external optical components, such as polarizers or waveplates.[164–167] Recently, twisted b-P heterostructure has been demonstrated for polarization detection, as shown in Figure 3d.[128] 2D plots of photocurrents generated from the

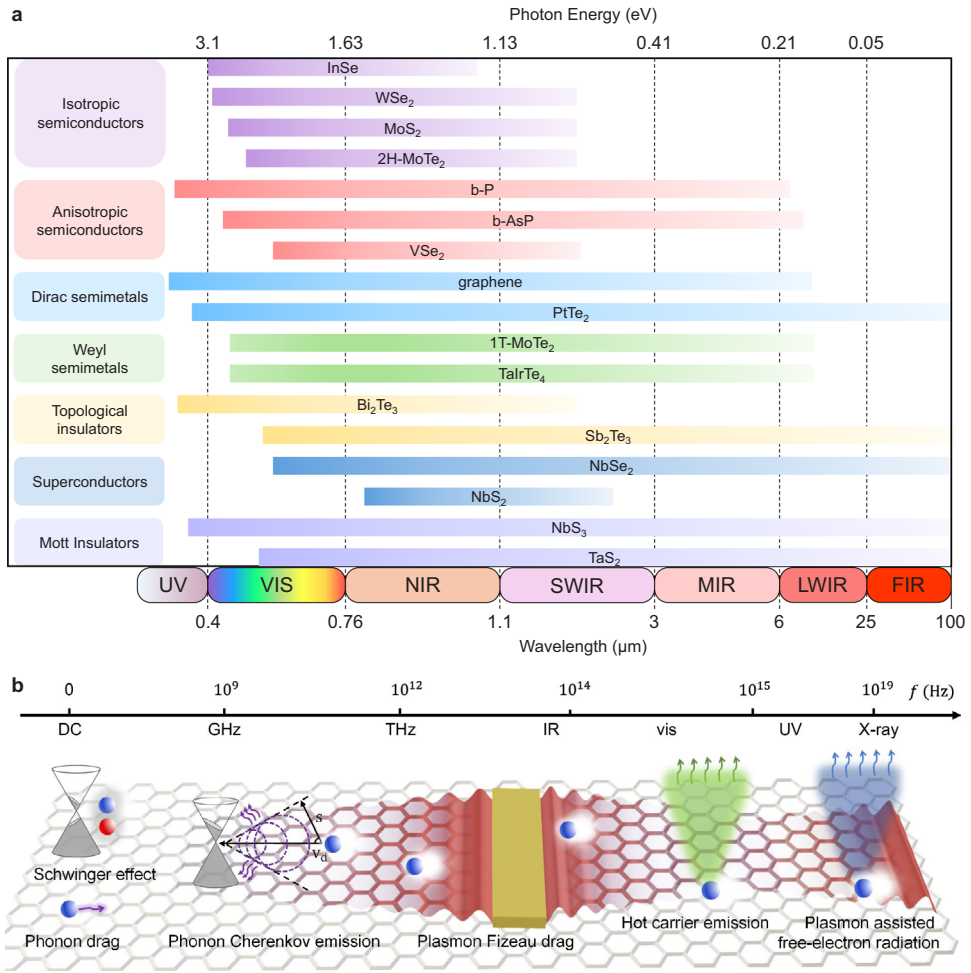

Figure 4. 2DM library spanning a broad IR wavelength range. a) Photoresponse coverage corresponding to wavelength and photon energy of representative IR-sensitive 2DMs, such as isotropic semiconductors (InSe,[168] MoS_2,[169] WSe_2,[170] 2H-$MoTe_2$[171]), anisotropic semiconductors (b-P,[172, 173] b-AsP,[174, 175] VSe_2,[176]), Dirac semimetals (graphene,[177, 178] $PtTe_2$,[179, 180]), Weyl semimetals (1T-$MoTe_2$,[181] $TaIrTe_4$[182]), topological insulators (Bi_2Te_3,[183] Sb_2Te_3[184]), superconductors ($NbSe_2$,[185, 186] NbS_2[187]) and Mott insulators (NbS_3,[72, 76] TaS_2[188]). b) Broadband spectrum of photoresponse in high-current-driven graphene at various frequencies. (b) Reproduced from ref. [189]. Copyright 2025, Springer Nature under the CC BY-NC-ND 4.0.

twisted b-P indicate the simultaneous detection of polarization angle and light power, paving the way for integrated polarimetric imaging and optical communication.

2.1.3. Broadband Photoresponse Spectrum

2DMs have been demonstrated ultrabroadband response,[49–59] as visualized in **Figure** 4a. Beyond their tunable light-matter interaction[25–31] and fast relaxation,[71–86] the unique properties of Dirac Fermions hosted by topological semimetals offer unique photoresponse across a broad energy spectrum.

For example, graphene exhibits intrinsic broadband absorption and ultrafast photocarrier dynamics due to its gapless linear dispersion and the massless Dirac Fermions, which can be modulated by electrostatic gating.[177, 190–193] Tuning the Fermi level effectively suppresses interband transitions for photon energies below $\hbar\omega < 2E_f$ due to Pauli blocking.[194, 195] As described by a Drude-like frequency dependence, activating intraband transitions enhances absorption in the IR regime.[196, 197] This process increases the energy of conduction-band electrons, leading to an increase in photo-induced conductivity, which is evident in the IR range.[49] Since the Fermi level in graphene is known to be electrically tunable up to ≈0.9 eV, controlling the cut-off of interband transitions through gating has potential for applications in tunable modulators and broadband PDs. Figure 4b illustrates that quasi-steady-states emerge in high-current-driven non-equilibrium conditions in graphene, manifesting across a broad energy spectrum. This phenomenon holds significant promise for IR detection, as it induces highly sensitive photocurrent driven by hot carriers, reveals pronounced nonlinear optical phenomena, and provides stable broadband performance by stabilizing hot carriers.

In the DC regime, nonlinear transport behaviors arise from mechanisms such as the Schwinger effect and phonon drag. The Schwinger effect is a non-perturbative prediction of

quantum electrodynamics, where charged particle-antiparticle pairs are created in a vacuum under a strong electric field.[198] However, observing this effect in vacuum has been difficult because it requires an electric field on the order of 10^{16} V· cm^{-1}. On the contrary, undoped graphene, where the Fermi level lies close to the Dirac point, allows the Schwinger effect to emerge at much lower electric fields than the vacuum.[199] Meanwhile, the phonon drag in graphene is closely related to the thermoelectric effect, where a thermal gradient induces a non-equilibrium phonon flow, which in turn moves electrons together through electron-phonon coupling, causes an additional contribution to the current, and increases the Seebeck coefficient.[200, 201] Cherenkov phonon emission is a non-equilibrium phenomenon that occurs when the drift velocity of electrons exceeds the speed of sound in the medium, which increases the phonon population since the stimulated emission of phonons dominates absorption. Thus, Cherenkov phonon emission induces asymmetric plasmon damping and additional photocurrents in graphene,[189, 202] typically observed in the GHz to THz frequency range.[203] In particular, the low effective mass and carrier density of Dirac Fermions in graphene result in a plasmon resonance frequency that lies near the IR region. Consequently, the Fizeau drag effect, in which electron flow is dragged by quasi-particles such as plasmons and surface plasmon polaritons, dominates in the IR regime.[204, 205]

Furthermore, plasmons in graphene can interact with electrons to emit radiation spanning the IR to X-ray range. Electrically excited hot carriers in high-energy states can emit plasmons via the quantum Cherenkov effect.[206] Since photon emission can occur through transverse electron oscillations arising from the interaction between free electrons injected into graphene and plasmons in graphene, local electron injection induces hot carrier emission,[207] enabling bright and stable light emitters in suspended graphene from the VIS to the IR range.[208] These highlight the unique light–matter interaction in graphene across a broad range of energies and underscore the potential for leveraging hot carrier dynamics in advanced optoelectronic applications.[209]

2.2. Extensive Library of IR-Sensitive 2DMs

Figure 5 categorizes an extensive library of 2DMs, encompassing semiconducting, metallic, insulating, ferroelectric, ferromagnetic, superconducting, and topological states, which is very attractive for flexible heterostructure design to overcome the intrinsic limitations of conventional bulk semiconductors in IR spectral detection.[210–213] This unique versatility has spurred the discovery of diverse IR-sensitive 2DM families that exploit distinct mechanisms. Narrow-bandgap semiconductors achieve IR detection through direct bandgap transitions that match the energies of IR photons, while TSMs and insulators leverage protected surface states for a broadband response. Superconductors offer noise-suppressed detection, and Mott insulators utilize strong electron correlations to abrupt metal-insulator transitions for IR detection. The expanding material toolkit enables IR PDs with programmable spectral selectivity, from NIR to THz range.[49–59]

2.2.1. 2D Narrow-Bandgap Semiconductors

2D narrow-bandgap semiconducting transition metal dichalcogenides (TMDs) are promising for IR PDs, leveraging their engineered bandgaps that bridge critical IR photon energies from 0.1 to 1 eV, like $MoTe_2$,[171] VSe_2,[176] $ReSe_2$,[223] $PdSe_2$,[224–227] and $TiSe_2$.[228] The most commonly utilized non-TMD 2D narrow-bandgap semiconductors include InSe,[168, 229, 230] Te,[231–236] black phosphorus (b-P),[46, 172, 173, 237–241] and black arsenic phosphorus (b-AsP).[174, 175, 242] The unique thickness-bandgap correlation enables bandgap engineering for tunable spectral response. For example, b-P and its alloyed derivative, b-AsP, exhibit layer-dependent bandgap engineering from 0.3 eV (bulk, MIR-sensitive) to 2.0 eV (monolayer, VIS-responsive) and provide broadband photoresponse.[237] Moreover, b-P and b-AsP feature strong in-plane anisotropy, leading to pronounced polarization-dependent responses for IR detection. For example, a room-temperature MIR detector based on a b-AsP/MoS_2/b-P heterojunction achieves polarization-resolved detection with an extinction ratio of ≈35.5 at 4.6 µm.[243] This value significantly exceeds extinction ratios typically obtained via other approaches, such as polarization-selective nanostructures.[244] Such polarization sensitivity holds significant promise for IR imaging, polarization-encoded communication, and target recognition.

2.2.2. 2D Topological Semimetals

Topological semimetals (TSMs) are classified into Dirac semimetals (DSMs), Weyl semimetals (WSMs), and nodal-line semimetals (NLSMs), distinguished by their distinct band-crossing configurations related to the spin-degeneracy.[188, 245–252] DSMs like graphene,[177, 178, 190, 226, 253–256] $PtTe_2$,[179, 180, 257–260] $PdTe_2$,[261–263] and Cd_3As_2[264–266] demonstrate quadruple-degenerate Dirac cones in momentum space,[246] hosting massless Dirac Fermions with ultrahigh mobility. DSMs can realize IR PDs that operate at room temperature with high sensitivity and fast operation, as photocarriers in DSMs produce a significant G and enhanced R_λ attributed to PTE.[177, 258] Hence, PDs based on $PdTe_2$/WSe_2,[262] and $PdTe_2$/Si,[263] heterojunctions exhibit a broad IR response with high D^* at room temperature. In particular, under IR illumination, type-II DSMs, such as $PtTe_2$ and $PdTe_2$, with a tilted Dirac cone along specific momentum directions, have a strong anisotropic dispersion relation with free carrier intraband transition.[260, 261] The strong coupling at the Fermi surface and the subsequent excitation of nonequilibrium carriers lead to field-selective chiral anomaly, strong spin-orbital interaction, and high spin Hall conductivity.[257, 259] Moreover, WSMs, such as Te,[267] 1T-WTe_2[268] and 1T-$MoTe_2$[181, 269, 270], feature spin-polarized nodes with opposite chirality, breaking time-reversal or inversion symmetry, generating topologically protected Fermi arc surface states, and enabling ultrafast helicity-dependent i_{ph}.[245] The nontrivial Berry curvature in WSM $TaIrTe_4$[182, 271] converts photon polarization into transverse currents via circular photogalvanic effect, achieving an anisotropy ratio of 1.92. Owing to symmetry-protected band crossings, gapless linear dispersion, and robust surface states, WSMs support broadband IR absorption while minimizing carrier scattering and

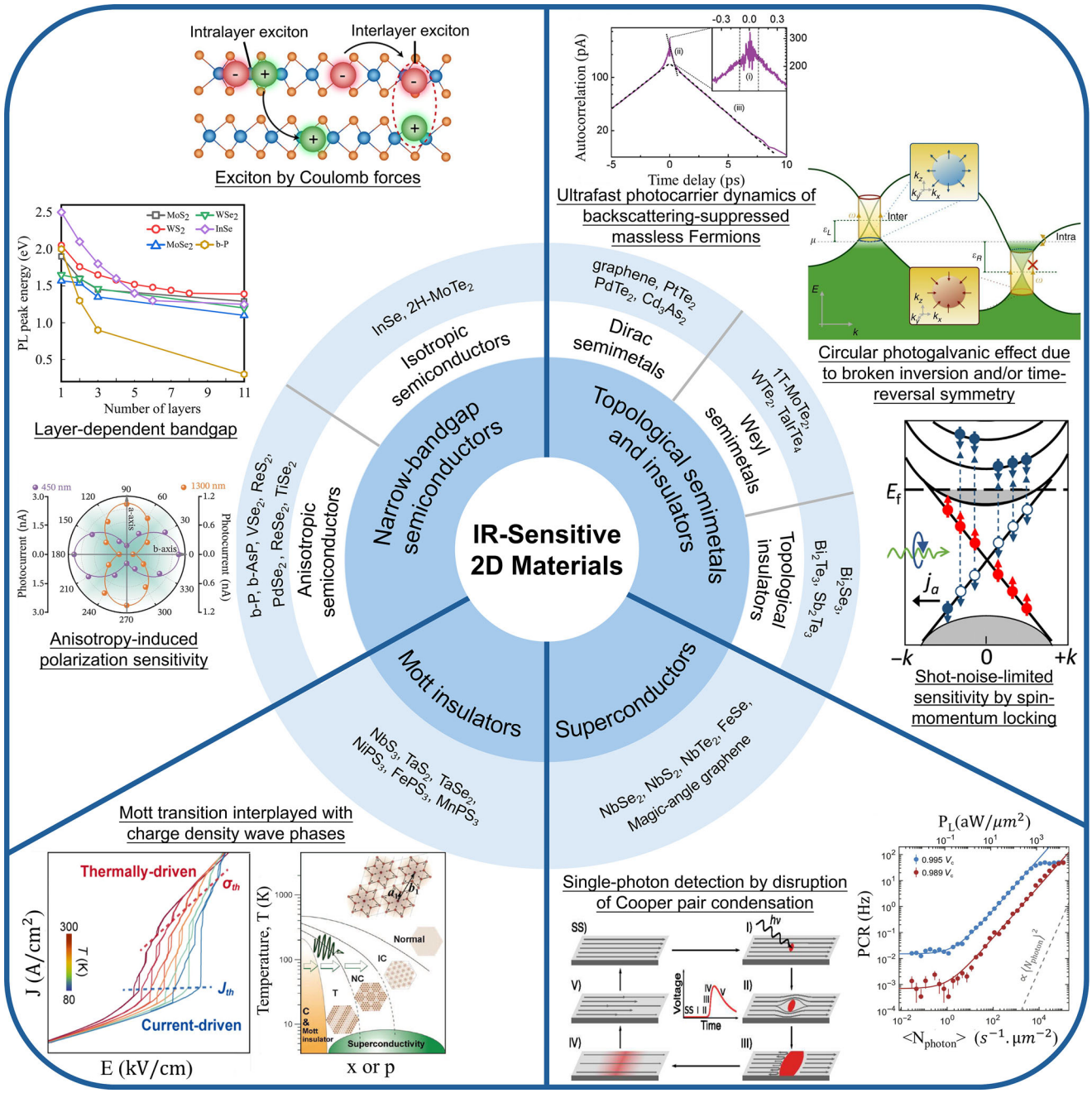

Figure 5. Classification and characteristics of IR-sensitive 2DMs. The schematic categorizes 2DMs into four major classes: narrow-bandgap semiconductors, topological semimetals and insulators, superconductors, and Mott insulators. Each class exhibits distinct electronic and optical band structures, offering diverse functionalities for IR PD applications. Narrow-bandgap semiconductors: Reproduced with permission.[214] Copyright 2023, American Chemical Society. Reproduced from [215]. Copyright 2024, UESTC and John Wiley & Sons Australia, Ltd under the CC BY 4.0. Topological semimetals and insulators: Reproduced from [216]. Copyright 2011, American Chemical Society under the CC BY 4.0. Reproduced from [217]. Copyright 2017, Springer Nature under the CC BY 4.0. Reproduced with permission.[218] Copyright 2021, AAAS. Superconductors: Reproduced from [219]. Copyright 2021, AIP Publishing under CC BY 4.0. Reproduced from [220]. Copyright 2024, AAAS under the CC BY 4.0. Mott insulators: Reproduced with permission.[221] Copyright 2024, American Chemical Society. Reproduced from [222]. Copyright 2015, AAAS under the CC BY-NC 4.0.

recombination losses. Lastly, NLSMs, represented by Cu_2Si[272], exhibit symmetry-protected band crossings that form closed 1D loops in momentum space, characterized by high mobility and the preservation of nodal-line topology against structural imperfections and external perturbations.

2.2.3. 2D Topological Insulators

Topological insulators (TIs) present a quantum phase distinguished by their topology-protected spin-momentum-locked Dirac surface states that coexist with insulating bulk states, which

is distinct from 2D semiconductors. The surface states of 2D TIs protected by time-reversal symmetry exhibit ultrahigh carrier mobility due to suppression of backscattering induced by defects and impurities, maintain shot-noise-limited conditions, and reduce noise sources by ≈3 orders of magnitude compared to conventional PDs. Therefore, the typical TIs, including Bi_2Se_3,[47, 234, 254, 273, 274] Bi_2Te_3,[183, 275, 276] Sb_2Te_3,[184, 277–281] and $GeBi_4Te_7$,[282] are promising candidates for sensitive IR detection.[283] Notably, a Sb_2Te_3 PD exhibits a high D^* of ≈1.22 × 10^{11} Jones at 980 nm, which is attributed to the ultrahigh carrier mobility and low noise properties of the topological surface states.[277] Furthermore, spin-momentum locking suppresses backscattering while enabling spin-polarized photocarrier generation and transport. In a TI-based PD, the helicity of incident light couples directly to surface electrons, generating directional spin-polarized photocurrents that reverse direction with propagation via the circular photogalvanic effect (CPGE).[218] Such intrinsic spin-momentum locking offers passways toward shot-noise-limited sensitivity, enabling fast and polarization-resolved IR detection. These topological properties position TIs as foundational materials for noise-immune IR optoelectronics and topological photonic circuits.

2.2.4. 2D Superconductors

2D superconductors, such as $NbSe_2$, NbS_2, $NbTe_2$, and FeSe, exhibit zero-resistance states below their critical temperatures, with superconducting-to-normal state transitions induced by exposure to IR light, enabling ultra-sensitive detection.[284, 285] When an external perturbation (e.g., photon absorption) disrupts Cooper pair condensation, the phase transition triggers resistance spikes that exceed ≈10^4-fold changes, enabling quantum-limited sensing, such as single-photon detection. Notably, magic-angle twisted bilayer graphene is a superconductor that enables single-photon detection at 1500 nm at temperatures as low as 0.8 K.[220] Recent breakthroughs, such as those achieved with $FeSe/SrTiO_3$, have resulted in an elevated T_c of over 60 K, which is compatible with liquid hydrogen systems.[286, 287] Likewise, 2D superconducting PDs exhibit low noise, high speed, and broadband IR response.

2.2.5. 2D Mott Insulators

2D Mott insulators, such as NbS_3, TaS_2, $TaSe_2$, $NiPs_3$, $FePs_3$, and $MnPs_3$, are strongly correlated quantum materials where strong Coulomb interactions dominate band transport, producing insulating states despite incomplete band filling.[288–291] The absorption spectrum of 2D Mott insulators, such as TaS_2[292–294] and NbS_3,[295] consists of a broadband and a sharp central peak due to the spin-charge interplay inherent in the strong correlation region. IR light can induce a phase transition in the charge-density-wave order of 2D Mott insulators. For example, 1T-TaS_2 exhibits a polymorphic charge density wave sequence, which undergoes current-driven and thermally driven phase transitions by applying an electric field and illumination of NIR light.[221] Phase transitions of charge density waves (CDWs) induced by IR light illumination can cause significant resistive switching, leading to a highly sensitive photoresponse. This strategy opens up new avenues for designing highly sensitive IR PDs. Recent studies demonstrate reconfigurable optoelectronic logic devices via charge-density-wave phase engineering, offering a promising approach for next-generation communication and AI hardware.[288, 290]

2.2.6. 2D vdW Heterostructures

Photodetection with 2DMs has the advantage of high sensitivity and fast response due to the strong light-matter interaction and the atomically abrupt interface.[71–86] Although tuning the photoresponse of a single 2DM by modulating the Fermi level with an external field is limited, the variety of vdW heterostructures formed by 2DMs based on an extensive library of their bandgaps and band offsets,[109, 296] coupled with the interlayer dynamics of photoexcited carriers across the interface,[297–302] facilitates the efficient separation of photoexcited carriers and provides an ideal platform for tunable IR PDs.

2.3. Progress and Prospect of 2DM-Based IR PDs

Here, we review representative IR detection mechanisms governing 2DMs and explore key innovations that drive the state-of-the-art 2DM-based IR PDs. Understanding these fundamental principles, which underpin their unique optoelectronic properties, is crucial for integrating them into novel device structures or advanced processes to design high-performance, innovative IR PDs that push the boundaries of IR technology.

2.3.1. IR Detection Mechanisms in 2DMs

2D narrow-bandgap semiconductors, b-P and b-AsP, utilize PCE as their photodetection mechanism. The narrow bandgap bridges the gap between graphene and TMDs, positioning it as a promising candidate for NIR-to-MIR detection. PCE-type PDs based on b-P and b-AsP have been extensively studied owing to their high responsivity and broadband absorption capabilities.[237, 242] For example, a b-P phototransistor operating at a 2 μm wavelength achieved a peak responsivity of 8.5 $A \cdot W^{-1}$.[46] The dominant photocurrent mechanism was identified as the PCE when the channel was lightly p-doped, enabling efficient separation and collection of photogenerated carriers under the applied bias. Very recently, a transient electric-field-driven polarity inversion in photoconductivity has been demonstrated in a $MoTe_2$/Pt Schottky junction that responds to alternating voltage inputs, achieving an extraordinary photocurrent response time of ≈3.8 ps. The photoconductivity transition from negative to positive is governed by the dynamic interplay between photoexcited carriers and the internal electric field at the interface, which a minimal variation in the applied reverse bias voltage can tune.[90]

The built-in potential separates photogenerated electron–hole pairs and attracts them toward their respective electrodes to produce photocurrent, playing a key role in PVE-type PDs.[25, 26, 34] PVE-type PDs can operate under zero-bias conditions (i.e., self-powered) in photovoltaic mode, eliminating the need for an external power source and effectively converting photon energy into

electrical energy. 2DM-based PVE-type IR PDs generally present excellent R_λ due to V_{oc} and i_{sc} in the IR region.[159, 224, 234, 303–309] Unlike the formation of a built-in potential by contacting two types of materials, Janus-type 2DMs have recently emerged as promising candidates for IR detection due to their out-of-plane polarity, enabling vertical PVE within a single channel. With asymmetric elemental distributions on both top and bottom surfaces, they exhibit intrinsic out-of-plane asymmetry, which induces a dipole moment and enables the spontaneous separation of photocarriers.[310, 311]

PGE induced by photocarrier traps can be identified by observing the horizontal shift of the transfer curves with and without light illumination in 2DM-based IR PDs.[28, 35, 49, 312] The PGE can be combined with field-induced tunneling to achieve high sensitivity and high speed simultaneously.[27, 254, 313] For example, the WSe_2/Ta_2NiSe_5 heterojunction-based PD utilizes PGE-assisted tunneling to achieve a simultaneous boost in both sensitivity ($\approx 10^3 A \cdot W^{-1}$) and fast response time (≈ 1 µs).[314] The tunnel barrier of the metal/semiconductor interface is tunable by charge transfer depending on the channel doping level due to PGE, where the photo-trapped charge modulates the Fermi level of WSe_2. Furthermore, the dependence of the photoresponse on both bias and wavelength enables the device to distinguish different wavelengths by sweeping the bias.

V_{PTE} typically ranges from tens of µV to tens of mV with gate-tunable response and spatial sensitivity to position-dependent thermal gradients, featuring selective control and localized detection. This makes PTE-based mechanisms attractive for applications requiring low-power operation and spatially resolved IR detection.[235, 236, 315] PTE-type PDs have been implemented with various 2DM combinations and structural designs, exhibiting excellent performance in terms of high sensitivity, low-power operation, broadband response, and further extending their potential applications coupled with plasmonic metasurfaces, such as polarimetric imaging,[316–318] wavelength selection,[191] energy harvesting,[319] and spin optoelectronics.[320]

Recent studies have highlighted the significance of the PBE in graphene-based PDs.[192, 321–323] Graphene exhibits low electronic heat capacity and a weak electron-phonon interaction, which extends beyond its capability for broadband wavelength detection. As a result, upon light exposure, the electron temperature rises rapidly, while thermal equilibrium with the lattice temperature is established relatively slowly. This electron-lattice thermal separation makes the channel resistance sensitive to small changes in the electron temperature, enabling bolometric detection of photons. An example of this concept is the dual-gated bilayer graphene hot-electron bolometer, which employs a tunable bandgap and electron-temperature-sensitive resistance to detect IR light and achieves noise-equivalent power of $\approx 33\ fW/Hz^{1/2}$ and sub-nanosecond response time at 5 K.[322] Notably, their performance significantly surpasses that of conventional Si and superconducting bolometers. A PBE-type PD with graphene/TiO_x/Al tunnel junctions is reported to exhibit strong bolometric responses due to the ultralow electronic heat capacity and thermal isolation by superconducting contacts, enabling a high R_λ of $\approx 10^5$ V W^{-1} and ultrafast response time of ≈5 ps under RF illumination.[323] A recent study explores that the photocurrent generation across the graphene/h-BN/graphene tunnel barriers under MIR illumination is dominated by thermally induced modulation of tunneling probability.[321] Thus, the photocurrent is found to be proportional to the electron temperature rise, serving as a sensitive probe of bolometric and thermoelectric effects at the tunnel barrier.

The PPE in ferroelectric 2DMs, such as In_2Se_3, $CuInP_2S_6$, and $LiNbO_3$ offers a fast temporal response and a broadband photoresponse across a wide wavelength range, further enhancing its applicability in IR PDs. Furthermore, PPE-type PDs do not rely on photon-induced carrier generation but instead operate via thermally induced mechanisms at room temperature. This characteristic makes PPE-type 2DM-based IR PDs particularly suitable for detecting long-wave IR (LWIR) and far-IR (FIR) radiation in uncooled conditions.[37, 38] Note that conventional LWIR and FIR PDs require a cryogenic cooling system to reduce thermal noise to achieve a sufficient signal-to-noise ratio.

Beyond individual photodetection mechanisms, they can be synergistically combined to enable hybrid modes,[33] such as PCE-PGE-PPE coupled,[324] PCE-PVE switching,[325] PVE-PGE switching,[254] PVE-PTE coupled,[253, 326] PVE-PPE,[327] PGE-assisted tunneling,[314] PGE-PPE coupled,[38] and PTE-PPE coupled.[328] For example, an InSe/$NbTe_2$ heterostructure demonstrated switchable photoresponse from PCE under forward bias to PVE under reverse bias due to the modulated band bending at the interface, leading to a high R_λ of $\approx 84\ A \cdot W^{-1}$.[325] A synergistic PD constructed by a quasi-freestanding hybrid structure of organic ferroelectric on MoS_2 has also been demonstrated to exhibit an ultrabroad wavelength range from 375 nm to 10 µm by coupling the mechanisms of PPE with PCE and PGE.[324] Another example involves hybrid mechanisms combining PVE and PPE in a heterostructure composed of 1D SnO_2 nanoneedles and 2D SnS_2 nanoflowers[327] and PTE and PPE in a γ-InSe PD.[328]

2.3.2. Evolution of 2DM-Based IR PDs

There have been numerous efforts to enhance IR detection by leveraging the unique properties of 2DMs.[71–86] The introduction of 2D vdW heterostructures and their integration with nanophotonic architectures have further enabled hybrid of IR detection mechanisms,[49–59] improving performance metrics of IR PDs.[39, 40] The evolution of 2DM-based IR PDs, driven by key innovations such as functionalized surfaces, interfacial barriers, and plasmonic structures, is summarized in **Figure 6**. The discovery of various 2DMs accompanies such key innovations.

The unique zero bandgap band structure of graphene, characterized by a linear dispersion shaped by a Dirac cone featured in the energy-momentum realtion, allows graphene to be placed as an ideal platform for tunable, ultrafast, and broadband PDs.[177, 190–193] However, due to its semimetallic nature associated with the absence of a bandgap, photocurrent generation in pristine graphene is primarily dominated by PTE. Thus, the performance of graphene-based PD has been limited mainly by the low absorption, resulting in a significant i_d and low D^*.

Various strategies to introduce other photodetection mechanisms, such as PGE, into graphene have been explored to produce a substantial G. A representative example is a hybrid PD incorporating a QD PbS surface layer on the graphene channel, achieving a $D^* \approx 2.5 \times 10^{10}$ Jones at 1,450 nm.[329] To

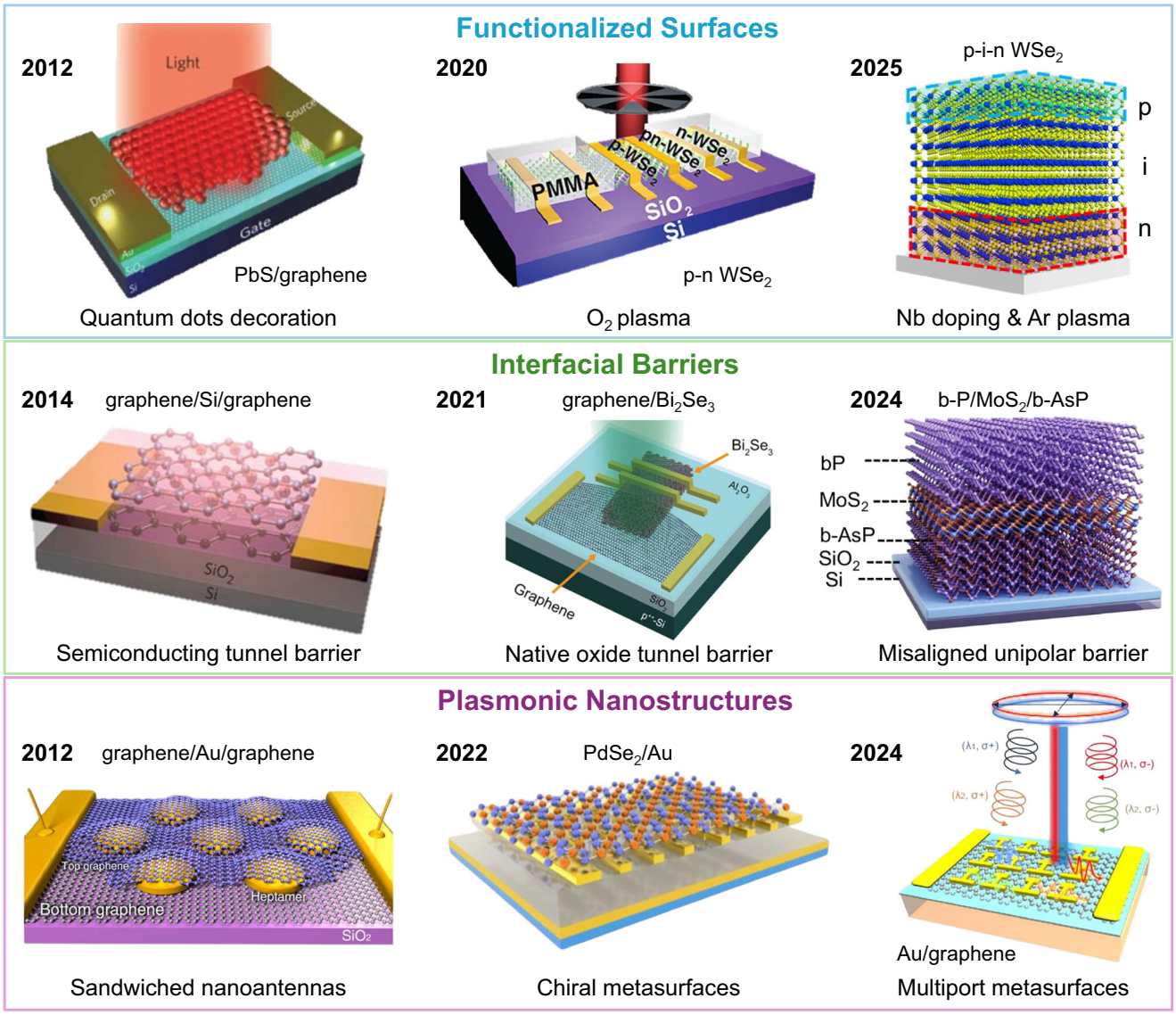

Figure 6. Technology progress and prospect of 2DM-based IR PDs. Timeline illustration of representative strategies employed to enhance the performance of IR PDs. Functionalized surfaces (e.g., quantum dots decoration, plasma treatment, and chemical doping) enable enhanced R_λ. Interfacial barriers (e.g., tunnel and unipolar barriers) are used to suppress noise and to improve D^* and the extended wavelength range. Plasmonic nanostructures (e.g., nanoantennas and metasurfaces) induce resonance at specific wavelengths and polarization sensitivity. Reproduced with permission. [329] Copyright 2012, Springer Nature. Adapted from [330]. 2020, American Chemical Society. Adapted from [331]. 2025, Springer Nature under the CC BY-NC-ND 4.0. Reproduced with permission.[193] Copyright 2014, Springer Nature. Adapted from [254]. Copyright 2021, American Chemical Society under the CC BY 4.0. Adapted from [332]. 2024, Springer Nature under the CC BY 4.0. Reproduced with permission.[333] Copyright 2012, American Chemical Society. Reproduced from [317]. Copyright 2022, American Chemical Society under the CC BY 4.0. Reproduced from [334]. Copyright 2024, Springer Nature under the CC BY-NC-ND 4.0.

address the lack of bandgap in graphene, 2D vdW heterostructures combining graphene with semiconducting TMDs, such as MoS_2 and WSe_2, have been implemented.[335] The bandgap of the absorption material fundamentally determines the achievable wavelength range of a PD. For example, MoS_2 and WSe_2 are suitable for VIS and NIR detection,[36, 330] while b-AsP and HgCdTe can extend the wavelength range to MIR.[332, 336]

TMD monolayers with direct bandgaps of 1–2 eV offer high sensitivity through excitonic absorption and a fast response. Incorporated into vdW heterostructures, they enable efficient separation of photoexcited carriers based on PVE. The photocarriers can be separated by built-in electric fields, leading to zero-bias operation and low *NEP*. Furthermore, graphene/TMD heterostructures can integrate the broadband and high-speed characteristics of graphene with the enhanced R_λ in TMDs.

In parallel, b-P has also garnered significant attention since 2014. b-P features a narrow and tunable bandgap (≈0.3 eV) and high carrier mobility ($\geqslant \approx 1000\ cm^2 \cdot V^{-1} \cdot s^{-1}$), making it highly promising for MIR detection. In particular, the anisotropic in-plane crystal structure leads to polarization-resolved detection,

further enhancing its potential for multifunctional IR detection. Remarkably, b-P-based PDs demonstrated in 2017 achieved room-temperature operation and broadband response.[173] Despite these advantages, b-P is chemically unstable in ambient conditions, exhibiting rapid degradation due to oxidation in the presence of oxygen and moisture. This limits its practical use and necessitates the implementation of passivation layers, encapsulation techniques, or material modifications to enhance environmental stability. To overcome this limitation, b-AsP alloys have emerged as a promising alternative by partially replacing phosphorus atoms with arsenic (As), retaining a similar band structure and broadband IR absorption to b-P while significantly improving air stability. Recently, b-AsP-based PDs have demonstrated broadband response (extending beyond ≈8 μm), excellent detectivity, and long-term operational reliability, positioning them as strong candidates for MIR detection.[175]

Achieving high sensitivity while maintaining low noise, high speed, and broadband coverage requires a multilayer strategy. 2DMs are particularly advantageous in this context due to their tunable bandgap and ease of heterojunction formation, which enable the separation of photodetection functions. This decoupling enables the optimization of material combinations and device structures based on bandgap and carrier mobility. This hybrid multilayer strategy allows for customizable engineering for 2DM-based IR PDs, such as functional separation (absorption in the active channel and balanced transport of the photocarriers from the channel to each electrode), noise suppression (minimized i_d with reduced traps at the interface or defects in the channel), and efficient photoexcited carrier separation (maximized built-in electric field and self-powered operation with complete depletion of the intrinsic layer to facilitate high-speed carrier drift).[71–86] Typically, narrow-bandgap semiconductors (e.g., $MoTe_2$, $PdSe_2$, b-P b-AsP, etc.) serve as the IR-absorbing layer, while wide-bandgap semiconductors or semimetals (e.g., MoS_2, WSe_2, graphene, etc.) act as low-noise charge transport channels.[46, 337, 338] Upon photoexcitation in the absorption layer, photogenerated carriers are selectively transferred to the transport channel across the favorable band alignment,[296] enhancing both photocarrier generation efficiency and charge separation, effectively addressing the high *NEP* and low *D** limitations often observed in single-channel 2DM PDs. Hence, the design flexibility enables tailored spectral response across a broad IR range.

Despite the inherent trade-off between high responsivity and fast response speed, recent studies have demonstrated strategies to enhance trade-off parameters concurrently.[193, 254, 317, 329–334] For example, vertical p-i-n photodiodes have been developed to exhibit enhanced performance metrics through a groundbreaking fabrication approach.[331] Specifically, for n-type WSe_2, selenium vacancies were created by plasma treatment with Ar in pristine WSe_2, which was then transferred to an Ag bottom electrode. The fabricated p-i-n photodiodes achieved maximum optical absorption in the intrinsic layer, efficient photocarrier separation, and high drift velocity. Interestingly, their photodetection performance has been further optimized by adjusting the thicknesses and Ar plasma treatment recipes for both p-type and n-type WSe_2 layers. Like this strategy, there has been a growing emphasis on simultaneous improvement across various performance metrics in 2DM-based IR PDs.

The standards and methodologies used to evaluate key performance metrics of IR PDs are critical, and several considerations must be carefully addressed in measurements.[39, 40] As the incident light wavelength increases, a fundamental trade-off often occurs, that is, due to increased i_d, higher *NEP*, and lower *D**.[36, 339] Nevertheless, as summarized in **Table 1**, recent developments have demonstrated IR PDs that maintain or even enhance *D** evaluated at the IR range but extend their wavelength range.[340, 341] Note that another critical trade-off between R_λ and response speed, which is attributed to the inherent limitation of the G-Δf product, is not covered here but is still essential. Furthermore, an accurate comparison of *D** requires a precise determination of the effective photoactive area and incident power density, alongside comprehensive noise characterizations, including dependence of G-Δf product and $1/f$ noise, and a consistent measured range of Δf to prevent performance overestimation.[39, 40]

3. Tunable Spectral Engineering of 2DM-Based IR PDs

Beyond the key performance metrics discussed so far, the emerging capabilities of IR PDs reflect a paradigm shift in developing 2DM-based IR PDs, such as spectrally tunable photoresponse, self-powered operation, polarization sensitivity, low-power operation, etc.[173, 193, 313, 335, 345–347] Coupling across diverse multiphysical domains can be used to synergistically tune the spectral response of 2DMs, including their band structure, carrier mobility, and dynamics of photoinduced carriers.[33] Likewise, various 2DM-based IR PDs have been engineered for high *D** across the IR range. Although some of them cannot provide spectral tunability after device fabrication, as their material combination and device structure determine the tunability of their bandgap or band alignment, several spectral engineering routes based on 2DMs offer significant versatility to IR PDs because their spectral response is geometrically and electrically tunable, as summarized in Table 2.[25–31]

3.1. Geometrically Tunable Spectral Engineering

We explore various strategies for implementing geometrically tunable spectral engineering in 2DM-based IR PDs. Fundamental symmetries, such as inversion, rotational, time-reversal, and gauge symmetries, can be engineered to tune the spectral response. Breaking spatial symmetry via local geometry can fundamentally alter the physical properties of 2DMs, including charge distribution, Fermi level, band structure, built-in electric field, and photocarrier dynamics, thereby influencing the spectral response of 2DM-based PDs.[355] Thus, geometrically tunable spectral engineering relies on engineering fabrication processes or introducing geometric asymmetries, leading to spatially controlled band alignments and optoelectronic characteristics, which inherently stem from geometry-driven symmetry breaking.

3.1.1. Heterostructure Engineering

Heterostructure engineering offers a compelling strategy to broaden the spectral range and enhance the overall

Table 1. Figure of merits of 2DM-based IR PDs. Higher R_λ and D^*, along with lower *NEP*, indicate better sensitivity and less noise, shorter rise and fall times indicate faster photoresponse, and a wider λ_{min} - λ_{max} represents a broadband photoresponse. Note that recent advances in 2DM-based IR PDs have demonstrated improved D^* evaluated in the IR range while extending their wavelength range λ_{min} - λ_{max}, overcoming the fundamental trade-off between them.[39, 40]

Year	Device structure	R_λ [A · W^{-1}]	*NEP* [W · Hz$^{-0.5}$]	D^* [Jones]	Evaluated λ [nm]	λ_{min} - λ_{max} [nm]	Rise time [µs]	Fall time [µs]
2013	MoS_2[36]	≈880	≈1.8×10^{-15}	≈7.86×10^{10}	561	400 – 680	≈4×10^6	≈9×10^6
2016	b-P[339]	≈82	≈5.6×10^{-12}	≈5.05×10^7	3,390	532 – 3390	τ≈1.6×10^2 (at 2.2 kHz)	τ≈3.2×10^2 (at 1.1 kHz)
2020	p-n WSe_2[330]	≈2	≈1.57×10^{-14}	≈7.2×10^{10}	852	400 – 900	≈5.37×10^4	≈1.028×10^6
2021	$PdSe_2$/InSe[342]	≈58.8	≈1.92×10^{-12}	≈10^{10}	1,650	532 – 1650	≈1.6×10^4	≈1.8×10^4
2021	PbSe/MoS_2[343]	≈137.6	≈2.18×10^{-14}	≈7.7×10^{10}	2,550	1200 – 3000	τ≈4.0×10^4 (at 1,310 nm)	
2022	graphene/Bi_2Te_3/GaAs[275]	≈0.668	≈7.93×10^{-12}	≈3.1×10^{12}	785	405 – 4500	≈5.1	≈3.7
2022	b-P/HgCdTe[336]	≈0.168	≈5.95×10^{-14}	≈1.81×10^{10}	4,300	520 – 4300	≈1.5×10^2 (at 637 nm)	≈1.1×10^2 (at 637 nm)
2024	b-P/MoS_2/b-AsP[332]	≈0.857	≈1.17×10^{-13}	≈2.3×10^{10}	3,745	2500 – 4200	≈5.0×10^{-1} (at 1,550 nm)	≈5.0×10^{-1} (at 1,550 nm)
2024	Nitride-doped MoS_2[344]	≈34	≈1.98×10^{-15}	≈5.92×10^{10}	1,550	300 – 2200	≈9.9×10^2	≈2.71×10^3
2025	graphene/b-P/MoS_2[345]	≈0.66	≈1.72×10^{-14}	≈2.38×10^{11}	3,600	325 – 3800	≈2.4×10^{-3} (at 1,550 nm)	≈8.8×10^{-3} (at 1,550 nm)
2025	$PdSe_2$/$MoTe_2$[307]	≈0.395	≈2.12×10^{-11}	≈1.92×10^{11}	980	300 – 4050	≈3.37×10^2	≈2.67×10^2
2025	HgTe/graphene[340]	≈1.2×10^4	≈3.7×10^{-15}	≈2.4×10^{11}	3,250	1500 – 5000	≈1.5×10^4	≈1.2×10^5
2025	$MoSe_2$/$PdSe_2$[341]	≈10^5	≈1.89×10^{-17}	≈4.1×10^{13}	785	532 – 10 600	≈2.56×10^2	≈2.78×10^2

performance of IR PDs based on 2DMs. By stacking 2D layers[356–358] or integrating them with materials of different dimensionalities,[329, 348, 359–363] the band alignment and interfacial charge dynamics are engineered to enable broadband IR detection with enhanced responsivity. This approach overcomes the intrinsic limitations of individual 2D semiconductors, enabling photodetection across the VIS to NIR and even MIR regions. These advances are particularly valuable for developing wavelength-selective or multispectral sensors with high sensitivity and tunability.

A hybrid MoS_2 phototransistor with PbS QDs has been reported to exhibit low-noise IR detection.[348] The device presented broadband response from 400 to 1,500 nm, achieving a maximum $R_\lambda \approx 6 \times 10^5$ A · W^{-1} at 635 nm. The MoS_2 functions as a high-mobility transport channel, while the PbS QDs serve as a size-tunable light absorption. Moreover, the spectral response range is extended into the NIR region owing to the narrow bandgap of the PbS QDs. Photogenerated electrons are efficiently transferred to MoS_2, while holes remain trapped in the quantum dots, leading to high photogain via PGE. Notably, the device operates in depletion mode, which helps maintain a low i_d and thereby improves *SNR*. These results show that integrating 2D semiconductors with quantum dot absorbers can enable sensitive detection over a broad wavelength range.

Mixed-dimensional vdW heterostructures, which combine materials of different dimensionalities, offer unique opportunities for engineering charge transfer dynamics and excitonic behaviors. For example, a monolayer WSe_2 has been integrated with

Table 2. Spectral response tunability of 2DM-based IR PDs. The spectral, geometric, and electrical tuning ratios are defined as the ratio of the maximum change (%) of the response (responsivity, photovoltage, or PL intensity) to the wavelength, pitch (µm) or strain (%), and gate or bias voltage (V), respectively. A higher ratio indicates greater geometric and electrical tunability per device, enabling enhanced spectral response tunability through spectral engineering.

Geometrically tunable spectral engineering		
Device structure (Strategy)	Spectral tuning ratio	Geometric tuning ratio
MoS_2/PbS[348] (Heterostructure)	≈5.6×10^{-4} %/nm	–
WSe_2 pn homojunction[330] (Local doping)	≈2×10^{-4} %/nm	≈6.8×10^{-2} %/µm
MoS_2[349] (Strain)	≈8.2×10^{-4} %/nm	≈5.0^{-2} %/%
MoS_2 Grating/InSe[138] (Photonic nanostructure)	≈5.1 %/nm	–
Metasurface-mediated graphene[253] (Photonic nanostructure)	–	≈8.0×10^{-3} %/µm
Electrically tunable spectral engineering		
Device structure (Strategy)	Spectral tuning ratio	Electrical tuning ratio
MoS_2/WSe_2[350] (Gate-tunable interlayer transport)	≈8×10^{-4} %/nm	≈1.5^{-2} %/V
MoS_2/b-P[351] (Bias-tunable thermionic emission and tunneling)	≈3.5×10^{-4} %/nm	≈6.0^{-2} %/V
b-P channel[352] (Gate-tunable bandgap due to Stark effect)	≈5.4×10^{-5} %/nm	≈4.0^{-2} %/V
p-i-n WSe2 homojunction[353] (Bias-tunable nonlinear memristive photoresponse)	≈4.6×10^{-3} %/nm	≈5.3×10^{-1} %/V
Semi-floating MoS_2 homojunction[354] (Gate-tunable photocurrent and relaxation time)	≈3.5×10^{-4} %/nm	≈7.9×10^{-5} %/V

1D PbI_2 nanowires to control over excitonic emission by tailoring the crystallographic orientation at the interface.[360] Two distinct contact geometries were studied. One is edge-standing, where PbI_2 is oriented perpendicular to the surface of WSe_2, and the other is layer-by-layer, where PbI_2 and WSe_2 are in parallel contact. In the edge-standing configuration, efficient charge transfer through the edges of the nanowire leads to the localized excitonic states, resulting in a pronounced redshift exceeding ≈40 meV in the PL spectrum, centered near ≈1.6 eV. In contrast, the layer-by-layer junction exhibits strong PL quenching, which is attributed to deep midgap states formed under type-II band alignment.

3.1.2. Local Doping Engineering

Conventional doping processes, such as ion implantation, face fundamental challenges due to structural damage or inadequate doping precision, [364, 365] and their alternative have been developed to accommodate the distinct physical characteristics of 2DMs.[366–371] Local doping engineering enables local modulation of carrier polarity and band alignment through chemical or plasma-based doping methods,[372, 373] such as the incorporation of substitutional elements[374] and surface functionalization.[375] From a spectral engineering perspective, local doping can also extend the spectral response beyond the intrinsic bandgap, particularly into the NIR range,[344] by introducing extrinsic sub-bandgap states[376] or enabling junction-assisted carrier collection.[377]

Plasma treatment locally induces surface doping on pristine 2DMs, forming a lateral p-n homojunction that enables gate-tunable spectral response from the VIS to NIR.[330, 344] For example, as illustrated in **Figure 7a**, a localized nitrogen-doping transformed the surface of naturally n-type MoS_2 into a p-type shell while preserving a high-mobility intrinsic n-type channel underneath, promoting effective photocarrier separation and transport. Importantly, nitrogen-induced defect states introduced sub-bandgap energy levels, enabling $D^* \approx 5.92 \times 10^{10}$ Jones at 1550 nm. This work highlights that spatially confined doping is beneficial for extrinsic detection, extending it to the NIR range.

In another study, vanadium doping in monolayer WSe_2 enabled fine control of the Fermi level to achieve various quantum tunneling behaviors across a $WSe_2/SnSe_2$ heterostructure, such as forward and backward diode operation, negative differential resistance, and ohmic switching.[382] This demonstration highlights precisely tuned local doping to design optoelectronic interfaces beyond conventional p-n junctions.

3.1.3. Asymmetric Contact Engineering

Asymmetric contact improves the performance of 2DM-based PDs by inducing built-in electric fields that facilitate efficient carrier separation and broaden the spectral response.[239, 251, 378, 383–388] Self-powered, low-noise PDs can be implemented with edge contacts[251] or asymmetric contacts.[95, 96, 239, 249, 347, 378, 383, 384, 389]

To enhance the bulk PVE, an edge-contacted semimetallic bismuth electrode has been employed with 3R phase MoS_2, enabling broadband photodetection.[251] Their device architecture contrasts conventional top-contacted geometries by fully exposing the in-plane polarization of the 3R-MoS_2 layers, which is otherwise inaccessible due to centrosymmetric stacking. This contact-induced strain, combined with efficient charge transfer at the edge interface, led to a more than 100-fold enhancement in the bulk PVE-driven i_{ph} across VIS and NIR regions.

A polarization-sensitive $ReSe_2$ PD with geometry-asymmetric Schottky contacts has been demonstrated to achieve self-powered operation and broadband spectral response, as illustrated in Figure 7b.[378] The asymmetry in contact area between source and drain created a Schottky barrier height difference, which led to efficient charge separation under illumination without external bias. Remarkably, the device generated a strong photocurrent under 808 nm illumination, demonstrating its ability to detect NIR light. This built-in field-driven separation mechanism, enabled solely by geometric asymmetry, played a key role in broadening the spectral detection range while maintaining low power consumption.

In addition, asymmetric Au and Ag contacts on a WSe_2 transistor have been employed to leverage the plasmonic hot-electron effect, thereby enhancing self-powered photodetection across a broad spectral range.[387] This asymmetric contact configuration also extended the detectable wavelength range into the NIR region, enabling successful detection at 1550 nm. Asymmetric contacts have also been implemented in a PTE-type PD of the $PdSe_2$ channel to enable sensitive LWIR detection at room temperature.[384] The work function difference between the two contacts, combined with their dissimilar thermal conductivities, induced a built-in temperature gradient and electric field under light exposure. In addition, b-P, combined with asymmetric graphene contacts, facilitated efficient injection of both electrons and holes, resulting in strong emission near ≈3.6 µm.[239]

3.1.4. Strain Engineering

2DMs have outstanding mechanical flexibility at their atomic scale thickness and exhibit exceptional strain tolerance. At high exciton densities in 2DMs, recombination is governed by exciton-exciton annihilation. This non-radiative process imposes fundamental limits on the optical performance of materials. Still, strain engineering can overcome this limitation by maintaining a near-unity PL quantum yield regardless of the exciton density of 2DMs[390] and strain-induced structural modifications to 2DMs effectively tune their local optoelectronic properties.[391–395] Several strain engineering techniques involve introducing strain during the fabrication processes or via bulk substrates.[394, 396–398]

As depicted in Figure 7c, the direct band gap of a trilayer MoS_2 can be blue-shifted for ≈300 meV per 1 % strain by applying biaxial compressive strain to a trilayer MoS_2 supported by a piezoelectric substrate and covered by a transparent graphene electrode.[349] A hybrid PL peak can also be induced in an $InSe/WSe_2$ heterojunction under strain through interlayer recombination processes.[399] As strain increases, the dominant channel of charge carrier transport shifts from the edge of heterojunction to the junction area, leading to more efficient recombination, as evidenced by the two distinct transconductance peaks and the coexistence of two conduction pathways.

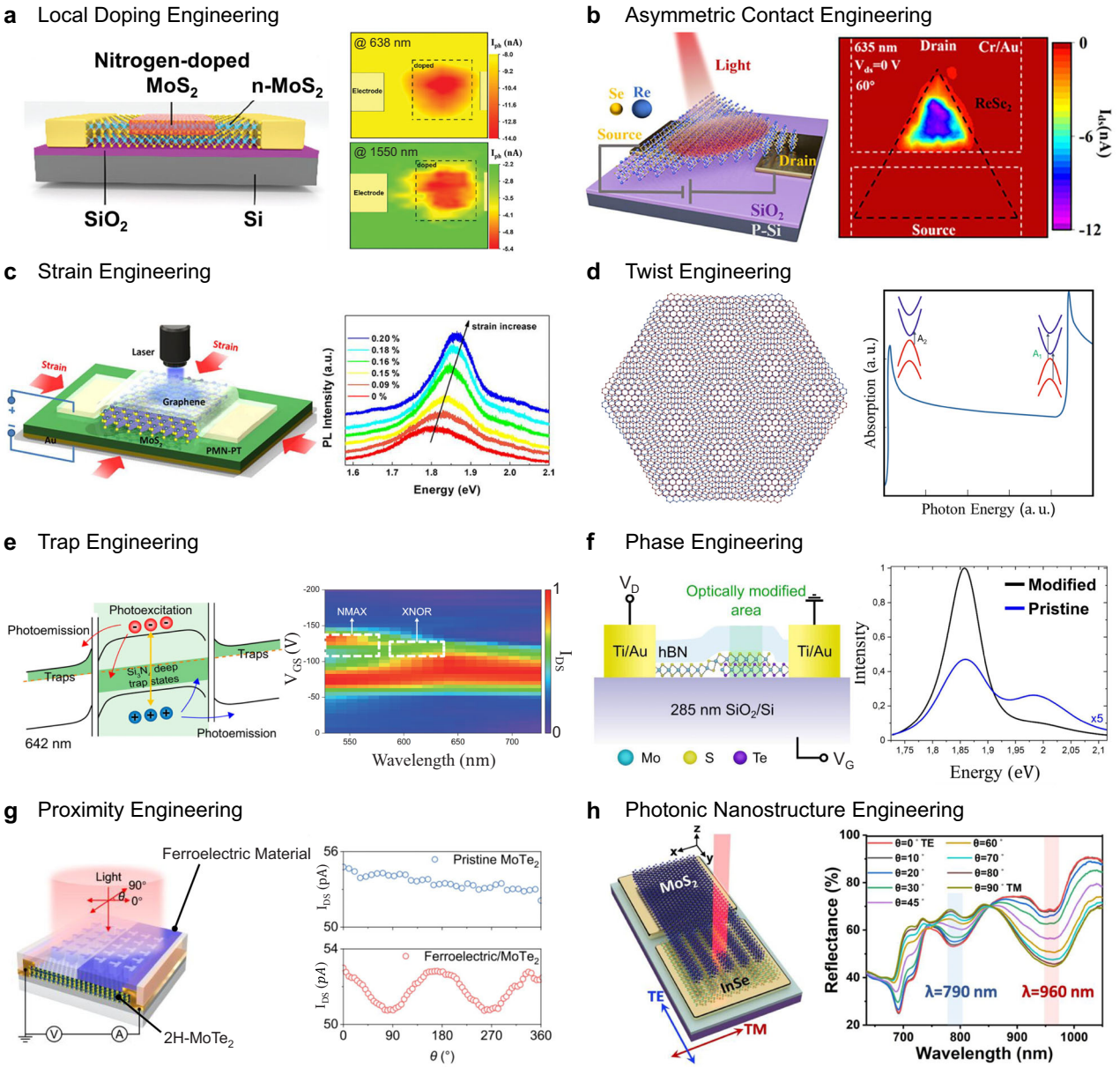

Figure 7. Geometrically tunable spectral engineering. a) A MoS_2 homojunction by localized nitrogen doping. b) Asymmetric metal contact to $ReSe_2$. c) Strain-induced enhanced PL of graphene/MoS_2. d) Moiré pattern and atomic registries of TBG. (Left) Absorption spectrum of TBG. (Right) TBG band structure highlighting A_1 (interlayer splitting) and A_2 (crystal field gap) transitions. e) CF_2 plasma-induced trap states for wavelength-dependent photoresponse. f) Optical modification to enhance PL intensity. g) Symmetry-breaking of 2H-$MoTe_2$ by patterned ferroelectric domain. h) MoS_2 grating on InSe for polarization-sensitive spectral reflectance. (a) Reproduced from [340]. Copyright 2024, Wiley-VCH under the CC BY 4.0. (b) Reproduced with permission.[378]. 2024, Wiley-VCH under the CC BY 4.0. (c) Reproduced with permission.[349] Copyright 2013, American Chemical Society. (d) Inspired by [346]. (e) Reproduced with permission.[379] Copyright 2024, AIP Publishing. (f) Reproduced from [358]. Copyright 2025, American Chemical Society under the CC BY 4.0. (g) Reproduced from [359]. Copyright 2024, Springer Nature under the CC BY-NC-ND 4.0. 2024, American Chemical Society. (h) Reproduced from [138]. Copyright 2025, American Chemical Society under the CC BY 4.0.

In particular, bandgap tuning in b-P from 0.22 to 0.53 eV was achieved by applying controlled strain for IR PDs.[400, 401] Specifically, modulation of the cutoff wavelength in photodetection was demonstrated through strain-induced tunability. Under 0.4 % compressive strain, the cutoff wavelength extended to ≈4.32 μm, while 1.0 % tensile strain shifted it to 2.44 μm. This strain-tunable b-P PD offers two key advantages: high D^* ≈ 8.45 × 10^9 Jones at 2000 nm under ≈1 % tensile strain at room temperature and broadband spectral tunability.

Furthermore, localized strain to 2DMs induced by patterned plasmonic structures, such as crumpled graphene or Au nanopillar arrays, enables spectral tunability or enhances optoelectronic performance.[402–404] For example, crumpled graphene structures

enable broad spectral tunability for plasmonic resonances from the NIR to the MIR region and strong confinement of plasmons with a high near-field intensity enhancement of ≈10^4.[402] A h-BN-encapsulated MoS_2 monolayer can experience ≈0.15 % local tensile strain by using geometrically confined recrystallization of patterned Au nanopillars.[404] The annealing recrystallizes Au into thicker, more crystalline structures, increasing a 65-fold-enhanced PL intensity of MoS_2 due to the Funnel effect, Fabry-Pérot interference, and Purcell effect.

3.1.5. Twist Engineering

Twist engineering of 2DMs creates tunable Moiré superlattices by manipulating the rotation angle between interlayers as a new degree of freedom in 2D vdW heterostructures, leading to novel phenomena, such as superconductivity,[405] ferromagnetism,[406, 407] Mott transitions,[408] and Moiré excitons[409, 410] for spectral tuning of broadband IR detection.

For example, magic-angle twisted bilayer graphene (TBG) has been shown to exhibit a tunable MIR bulk PVE,[411] which is attributed to Berry curvature and quantum-metric contributions induced by the Moiré superlattice. In 1.2°-TBG, the strong interlayer Moiré potential gives rise to a rich variety of states from multiple minibands. In particular, possible strain or interactions may lead to symmetry-breaking in TBG, thereby altering the bulk PVE. Besides, the intensity and polarity of the bulk PVE can be flexibly adjusted by the gate voltage. While small-angle twisted structures exhibit enhanced Moiré interactions and symmetry-breaking that give rise to unique quantum phenomena, larger twist angles offer distinct advantages through their tunable interlayer coupling. In 15°-TBG, the 400 meV interlayer-split band (A1) and 10 meV crystal-field-induced gap (A2) synergistically enable enhanced absorption by interband optical transitions, as shown in Figure 7d.[346] Additionally, the two BLG layers act as dual screening gates, which suppresses electron–hole collisions and increases carrier mobility, achieving a R_λ ≈4 A · W^{-1} at 11.07 μm, one order of magnitude higher than that of bilayer graphene. Bias optimization further increases η_e, reaching ≈40 % at a bias voltage of 2 V. These novel mechanisms in twisted vdW heterostructures of 2DMs benefit ultra-high R_λ[412, 413] and polarization sensitivity[128, 414].

3.1.6. Trap Engineering

Trap engineering has become a key enabler in extending the spectral range and enhancing functionality by introducing extrinsic trap states through chemical modifications and plasma treatment.[379, 415, 416] Trap-associated PGE holds strong potential for spectral engineering, and photocarriers can be temporarily captured, resulting in prolonged lifetimes and persistent photoconductivity, which is particularly effective for enhancing detection in the NIR, where limited photon energy typically hinders carrier excitation. In addition, traps provide a means to modulate carrier recombination dynamics, enabling wavelength-selective gain, memory effects, and even logic-level differentiation.

A Ta_2NiSe_5/SnS_2 heterojunction has been explored for broadband in-memory sensing in physisorption-assisted optoelectronic synaptic transistors, covering a spectral range from 375 to 1310 nm.[416] O_2 and H_2O molecules physisorbed on SnS_2 introduced additional localized trap states, significantly prolonging the lifetime of photogenerated electrons and amplifying PPC with PGE. Notably, even after the light source was removed, the gradual detrapping of holes from the interfacial barrier continued to result in a continuously decaying photocurrent, underscoring the persistent influence of trap-assisted dynamics on device performance. As a result, the device achieved a $R_\lambda \approx 5.6 \times 10^3$ A · W^{-1} and $D^* \approx 4.1 \times 10^{14}$ Jones at 405 nm, and also maintained notable $R_\lambda \approx 14.4$ A · W^{-1} and $D^* \approx 1.1 \times 10^{12}$ Jones at 980 nm.

A wavelength-configurable anti-ambipolar and bi-anti-ambipolar photoresponses have been proposed in an InSe transistor with a Si_3N_4 charge-trap layer, wherein trap states were introduced through CF_4 plasma treatment, as illustrated in Figure 7e.[379] These trap states, embedded within the InSe channel, enabled charge trapping and detrapping during gate voltage sweeps, which generated a distinctive anti-ambipolar peak in the transfer curve. In particular, the interplay of these trap-induced processes enabled switching between anti-ambipolar and bi-anti-ambipolar photoresponses, featuring single- and dual-transconductance peaks, respectively, depending on the incident light wavelength. This optical modulation enabled the realization of multi-valued logic gate operations, such as NMAX and XNOR, in a single device, significantly enhancing data density by factors of 6 and 19, respectively. These results highlight how spatially and spectrally engineered trap states can serve as functional selectors for wavelength-dependent logic operations.

3.1.7. Phase Engineering

The interaction between light and 2DMs leads to a variety of interesting physicochemical phenomena.[417, 418] Among them, laser-based optical modification has emerged as a rapid and versatile technique. Prior studies have demonstrated enhanced fluorescence emission,[419] transitions between anti-ambipolar and bi-anti-ambipolar photoresponses[380], and enhanced third-harmonic generation through phase transitions.[420]

Optical and structural modifications of WS_2 monolayers have been achieved through a focused laser beam, resulting in an approximately ninefold enhancement in fluorescence intensity following laser-induced treatment.[419] Selective modification implements power-dependent direct laser writing to realize "micro-encryption" on WS_2 monolayers. Building on these, a concept has been extended to heterostructures to demonstrate diverse optical functionalities through continuous-wave laser-induced modifications, offering a promising route to overcome the intrinsic limitations of monolayer 2DMs.[380] The modification of a $MoTe_2/MoS_2$ heterostructure using a 532 nm continuous-wave laser results in a ≈43-fold enhancement in PL and the emergence of anti-ambipolar behavior, as shown in Figure 7f. This enhancement is attributed to the simultaneous thinning of the MoS_2 layer and to the modification of the dielectric environment induced by Te clusters. The enhanced gate-tunable transfer characteristics observed after laser modification were hypothesized to arise from a combination of band alignment shifts, work function modulation, and dielectric screening effects introduced by the incorporation of tellurium clusters into the underlying SiO_2 substrate.

A Schottky diode was fabricated by inducing a polymorphic $MoTe_2$ junction via optical modification, wherein a partially metallic phase was locally formed within the semiconducting $MoTe_2$ channel.[420] This polymorphic engineering enabled the controlled transition from the 2H to the 1T' phase. Notably, the phase-transitioned 1T'-$MoTe_2$ exhibited a sevenfold enhancement in third harmonic generation intensity compared to its semiconducting 2H counterpart. Lateral heterojunctions leveraging the polymorphism of TMDs offer promising avenues for diverse applications. Due to the strong in-plane covalent bonding between atomic layers, lateral heterojunctions exhibit superior electronic performance compared to their vertically stacked counterparts, including lower contact resistance, higher carrier mobility, and a minimized contact area. Recently, a study demonstrated the phase transition of 2H-$MoTe_2$ to the 1T' phase by optimizing laser power and exposure duration.[421] Furthermore, a 1T'-to-T_d phase transition was observed at 230 K, highlighting the potential to engineer and tailor specific phase domains for targeted functionalities spatially.

3.1.8. Proximity Engineering

The proximity effect is a phenomenon in which the physical properties of one material influence those of another material without direct physical coupling when the two materials are brought into contact. In particular, extensive research has been conducted on heterostructures formed by interfacing graphene with TI, where the initially weak spin–orbit coupling of graphene is significantly enhanced via the proximity effect, resulting in the emergence of nontrivial spin textures in the graphene band structure.[422, 423]

For example, graphene integrated with TI has remarkable spintronic properties and features proximity-induced spin-charge conversion.[424–426] The nonlocal detection of photoexcited, valley-locked spin-polarized charges is demonstrated in a WSe_2/graphene/Bi_2Se_3 heterostructure at room temperature.[424] Combining inversion asymmetric WSe_2 and a spin-orbit coupled TI, enables helicity-dependent spin photocurrent generation and detection via proximity-induced spin-momentum locking. In particular, a gate-tunable spin-galvanic effect is observed in their vdW heterostructures at room temperature,[427] providing evidence for a proximity-induced, locally tunable spintronic response in hybrid bands.[425, 426]

In addition to spin-orbit coupling-driven proximity effects, geometric asymmetry at heterointerfaces has also emerged as an effective tool for engineering polarization-sensitive photoresponses. For instance, ferroelectric domains break the rotational symmetry, enabling 2D homojunctions defined by ferroelectric domains to detect IR-polarized light with an ultrahigh polarization sensitivity,[381, 428] as shown in Figure 7g. Furthermore, the incompatibility between C_3/C_2 symmetries at the heterointerface induces an in-plane electric polarization, generating a spontaneous photocurrent along the polarization axis.[429]

3.1.9. Photonic Nanostructure Engineering

2DM-based PDs combined with photonic nanostructures, such as metallic nanoantennas and dielectric nanocavities, exhibit enhanced photoresponse due to resonant light absorption at specific wavelengths and polarization sensitivity. Modifying their size, shape, material composition, and pattern geometry allows for precise tuning of the resonant wavelength, improving optical response at the target wavelength and enhancing performance in wavelength-selective sensing applications.[134–138, 140, 235, 276, 317, 318, 334, 430–453]

For example, the spectral response of WS_2/MoS_2 heterostructures has been enhanced by incorporating Au nanoparticles, resulting in a ≈25-fold improvement in R_λ while maintaining a fast response rate through surface plasmon resonance.[134] Besides, although WS_2 and MoS_2 individually exhibit limited sensitivity to IR light, the strong interlayer coupling within the heterostructure effectively extends their photoresponse into the IR regime.

As mentioned above, metallic plasmonic nanostructures are widely employed to enhance the inherently weak light–matter interactions in plasmonic engineering; however, their high optical losses in the IR region pose significant limitations. To address this issue, self-hybridized lateral pattern grating structures based on TMDs have been proposed. These architectures offer several advantages, including reduced optical loss, coordinated excitonic modes, polarization-dependence, and selective enhancement of light–matter interactions.[135–138] As illustrated in Figure 7h, a vdW heterostructure of MoS_2 grating and InSe flake stacked on metallic electrodes presented spectrally-selective polarization-sensitive photodetection in the NIR region, achieving a high dichroic ratio (≈1.61 at 790 nm and ≈1.88 at 960 nm).[138]

The strong coupling between TMD excitons and plasmonic resonances offers promising opportunities for next-generation optoelectronic and quantum photonic applications.[431, 447, 450, 451] In particular, exciton-plasmon interactions have been demonstrated using grating structures of nanopatterned TMDs fabricated on metallic substrates.[135–138] Tuning the geometric parameters of the WS_2 grating, such as its width, thickness, and period of grating, enables the control over exciton, cavity photons, and plasmon polaritons, and achieves the strong coupling with an effective energy separation exceeding ≈410 meV.[135]

Very recently, photonic bound states in the continuum (BICs) have emerged as a standout platform for strong light-matter interactions. For example, nanostructured bulk WS_2 has been demonstrated to give rise to BICs, exhibiting resonances with sharp, tailored linewidths and selective enhancement of light-matter interactions, delivering fundamental insights and practical device concepts for polaritonic applications.[137, 452]

3.2. Electrically Tunable Spectral Engineering

Unlike geometry-driven symmetry breaking, an electric field applied to 2DM-based IR PDs breaks the intrinsic symmetry by introducing an asymmetry in the physical properties of 2DMs. This subsection highlights recent strategies for tailoring the spectral response of 2DM-based IR PDs that utilize bias or gate voltage to tune band alignment, control interlayer transport, induce a Fermi-level shift, apply an electrical field along the out-of-plane direction to the semiconducting channel, and modulate the interfacial barrier height. These electrically tunable spectral

engineering schemes can in situ tune the spectral response of 2DM-based IR PDs, thereby reducing the footprint of spectrally tunable PD systems and offering versatility in intelligent optoelectronics.

3.2.1. Transport Engineering

As depicted in **Figure 8**a,b, transport engineering involves manipulating carrier dynamics, specifically photoexcited carrier transport across the interface, enabling in situ tuning of spectral responsivity.[345, 350, 454] 2D vdW heterostructures provide in situ control over carrier transport mechanisms, such as interlayer transition, interlayer recombination, direct tunneling, Fowler–Nordheim (FN) tunneling, and thermionic emission.[254, 304, 325, 342, 350, 455–457] The gate-tunable band alignment across the 2D vdW heterointerface enables the effective modulation of carrier transport. Variations in the majority-carrier concentration across layers under an applied gate voltage result in distinct changes in i_d and shifts in the dominant photoresponse region. Moreover, due to the unique density-of-states in each channel, the band-edge energy can also be modulated by both bias and gate voltages.[458–461] Furthermore, 2D vdW heterostructures exhibit stacking-order–dependent sensitivity to gate voltage. In a vertically stacked structure, the top layer typically shows reduced gate sensitivity compared to the bottom layer due to electrostatic screening. This behavior, combined with intrinsic material properties, such as dopant impurities arising from atomic vacancies, enables tunable spectral responsivity.

For example, a WSe_2/b-P/MoS_2 floating-base bipolar junction n-p-n phototransistor has facilitated efficient carrier injection and photo-amplification via internal gain, by adopting b-P as the base, lightly doped WSe_2 as the collector, and highly doped MoS_2 as the emitter.[356] As a result, the device exhibited enhanced $R_\lambda \approx 6.32\ A \cdot W^{-1}$ and $D^* \approx 1.25 \times 10^{11}$ Jones at 532 nm, $R_\lambda \approx 1.12\ A \cdot W^{-1}$ and $D^* \approx 2.21 \times 10^{10}$ Jones at 1,550 nm, respectively. This structural design effectively broadened the broadband response from the VIS to the IR range. Another example is a b-P/InSe heterojunction that exhibits a broken gap, and its critical band-to-band tunneling memory generates a cumulative negative photocurrent that persists even in the dark for incident light of various wavelengths.[465]

Most 2D TMDs exhibit layer-dependent momentum-indirect band structures that determine interlayer recombination characteristics. Numerous studies utilize this feature in IR PD, demonstrating the adoption of a momentum-matching strategy by adjusting the number of layers of each material.[342, 455–457] A momentum-aligned k-space driven direct bandgap can be realized through a 2D vdW heterojunction with indirect bandgaps, which enables interlayer transitions at the band edge, effectively extending the detection range to the IR region.

3.2.2. Exciton Engineering

The applied gate voltage not only governs various transport mechanisms but also modulates photoresponse across different wavelengths by shifting the Fermi level within the channel layer. Strong photoresponse at particular wavelengths is typically attributed to exciton absorption resonance. The exciton oscillator strength is maximized when the Fermi level approaches the charge-neutrality point, a condition under which Pauli blocking is minimized and Coulomb interactions experience reduced screening.

The large binding energy and long lifetime (≈μs) of interlayer excitons establish them as robust quasiparticles for next-generation excitonic PDs.[114, 466–469] Interlayer excitons in vdW heterostructures retain the spin and valley properties of constituent carriers and exhibit large electric dipole moments, enabling high tunability across energy and spatial scales.[470–472] Electroluminescence from interlayer excitons has been observed in $MoSe_2/WSe_2$ heterostructures, as shown in Figure 8c. The lower energy of interlayer excitons compared to their intralayer counterparts amplifies Coulomb interactions that drive exciton accumulation at heterointerfaces, facilitating efficient radiative recombination.[462]

In addition, the energy of interlayer excitons is typically smaller than intralayer excitons, extending the spectral range beyond the cutoff wavelength of individual materials. The optical response spectral range of a WS_2/HfS_2 heterojunction can be extended to ≈20 μm through electric field modulation of interlayer excitons.[213] The bias voltage will also affect the alignment of energy bands, adjusting exciton recombination behavior. As a result, the photoelectric characteristics of interlayer excitons can be tuned.

3.2.3. Stark Effect Engineering

Energy levels are fixed, but the Stark effect can shift them under an electric-field displacement, especially when a vertical electric field is applied along the out-of-plane direction of the semiconducting channel. The Stark effect is generally categorized into two types: the quantum-confined Stark effect and the giant Stark effect. The quantum-confined Stark effect describes the influence of an external electric field on the optical spectrum of quantum wells, typically resulting in a redshift and a reduction in oscillator strength.[473–475] In contrast, the giant Stark Effect refers to the significant and highly sensitive bandgap modulation observed in certain 2DMs under an external electric field, enabling substantial tuning of their spectral responsivity.

Stark effect engineering induces variations in bandgaps and excitonic features that are tuned by the applied field. As illustrated in the left panel of Figure 8, the giant Stark effect drives valence and conduction bands toward each other.[463] The Stark effect can effectively modulate energy distribution, wave function, and recombination rate of excitons. For instance, the Stark effect manipulates the wavefunction overlap of interlayer excitons across the WSe_2/InSe vdW interface due to strong interlayer coupling. As a result, the interlayer exciton emission tunes its energy as much as ≈180 meV, as shown in the right panel of Figure 8d.[455]

The bandgap of p-doped few-layer b-P depends on the applied displacement field induced by dual gates due to the giant Stark effect. This feature is particularly pronounced because b-P possesses an orthorhombic crystal lattice with a puckered honeycomb structure, where the conduction band minimum and valence band maximum are predominantly composed of localized

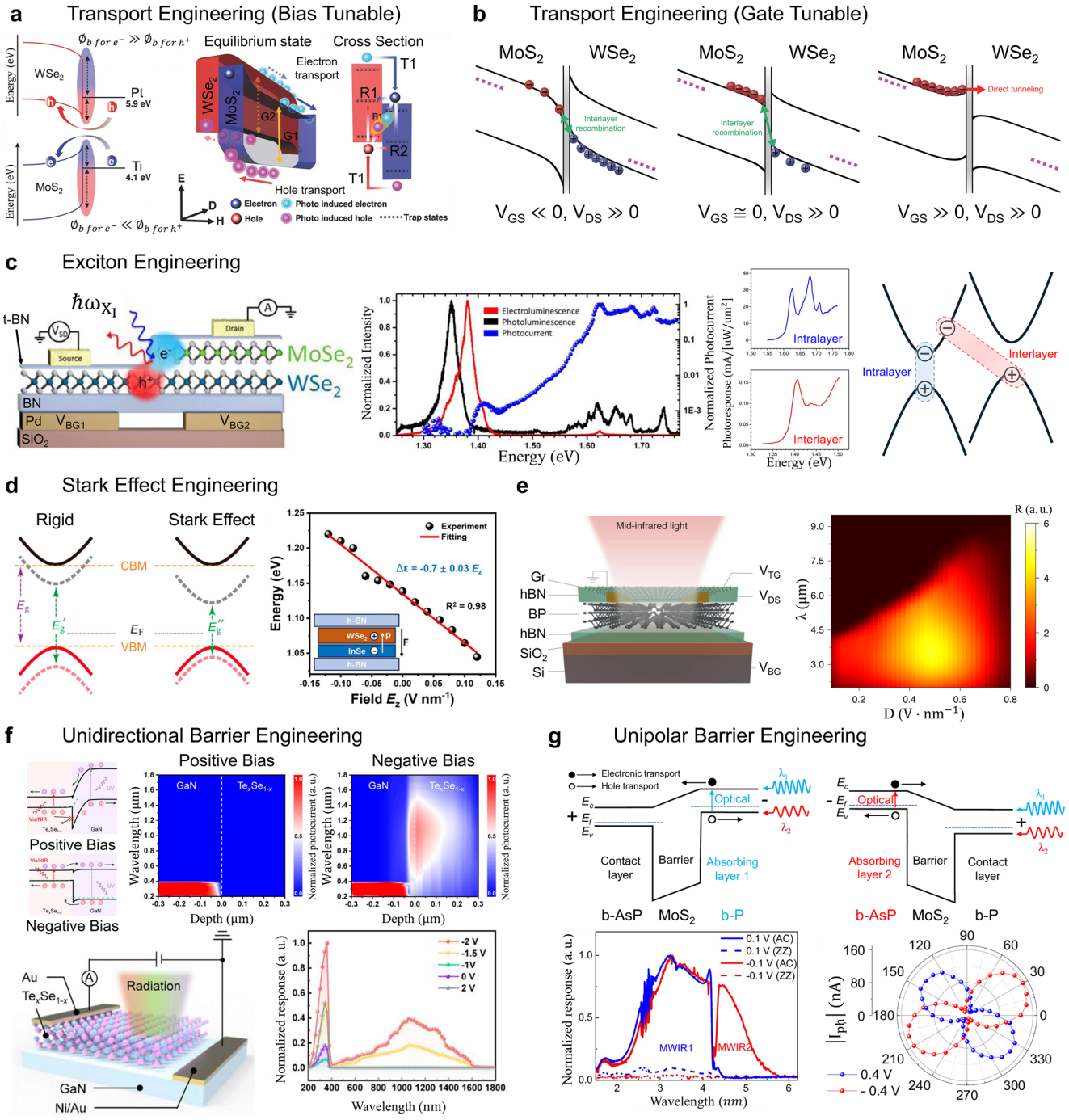

Figure 8. Electrically Tunable Spectral Engineering (a,b) Transport engineering of a MoS_2/WSe_2 heterostructure with bias tunable a) and gate tunable b) photoexcited carrier transport across the interface. c) Spectral response tuned by interlayer and intralayer excitons. d,e) Stark effect induced by displacement field applied to the 2DM channel, tuning its bandgap (d) and spectral responsivity (e). f) Tunable unidirectional barrier height, where IPE determines spectral responsivity through the interfacial barrier height. g) Tunable spectral responsivity due to the switchable absorption layer, depending on the bias voltage. (a) Reproduced with permission.[454] Copyright 2016, Wiley-VCH. (b) Reproduced with permission.[350] Copyright 2022, AAAS. (c) Reproduced with permission.[462] Copyright 2016, American Chemical Society. (d) Reproduced with permission.[463] Copyright 2017, American Chemical Society. (Left) Reproduced with permission.[455] Copyright 2024, American Chemical Society. (Right) (e) Reproduced with permission.[352] Copyright 2021, Springer Nature. (f) Reproduced from [458]. Copyright 2025, Wiley-VCH under the CC BY 4.0. (g) Reproduced from [332]. Copyright 2024, Springer Nature under the CC BY 4.0.

P $3p_z$ orbitals [476]. These orbitals are highly sensitive to a vertical electric field applied to the b-P channel, enabling a gate-tunable bandgap. Under the reverse bias, hole accumulation near the gate electrode forms a screening layer, keeping the bandgap constant. On the contrary, under the forward bias, electrons accumulate in the b-P layers near the gate electrode. Once the conduction band aligns with the Fermi level due to sufficient electron accumulation, further bandgap reduction is halted by the Fermi level pinning effect. This gate-tunable modulation of the bandgap, driven by the giant Stark effect, effectively tunes spectral responsivity from 2 to 9 μm, as shown in Figure 8e.[352]

3.2.4. Unidirectional Barrier Engineering

A gate-controlled Schottky barrier, known as a graphene barristor, has been demonstrated,[477] where the Fermi level of graphene can be effectively modulated by gate voltage when graphene is in contact with a semiconductor channel or substrate, thereby tuning the Schottky barrier height. Graphene barristors with wide bandgap semiconductors, such as GaN, feature heterojunctions with a unidirectional barrier that can block the photoresponse to light with wavelengths longer than the semiconductor bandgap under forward bias, and exhibit spectral responsivity to light with wavelengths shorter than it under reverse bias. Here, its spectral responsivity is primarily determined by the transport of photoexcited carriers across the graphene/semiconductor interface, namely internal photoemission (IPE) via the gate-tunable Schottky barrier height.[478–480] IPE exhibits unique wavelength dependence, where the probability of electrons being emitted from a material upon light illumination varies with the incident light wavelength. This dependence is primarily due to the energy of the incident photons, particularly the potential barrier at the interface.

A spectral response is tunable by modulating the Schottky barrier height in vertically stacked p-type and n-type graphene barristors.[478] Selective detection at different wavelength bands was achieved through gate-controlled *G*. Specifically, the device exhibits anti-ambipolar behavior in the dark and under light illumination, where light exposure shifts the anti-ambipolar transfer curves toward either the negative or the positive gate-voltage direction, depending on the polarity of the semiconductors. These gate- and wavelength-dependent transfer curves enabled multicolor detection.

A similar feature can be observed in a multispectral PD based on a Te_xSe_{1-x}/GaN heterojunction with a bias-tunable unidirectional barrier,[464, 481] as illustrated in Figure 8f. This enables bias-tunable spectral responsivity, which the IPE determines across the interfacial barrier height. Furthermore, phototransistors with double graphene/semiconductor Schottky barriers[480] or a gated metal/MoS_2 Schottky barrier[347] have also been reported, suggesting that the spectral responsivity can be tuned by unidirectional barrier height.

3.2.5. Unipolar Barrier Engineering

A unipolar barrier can suppress i_d by blocking the majority carriers, thereby achieving high performance at room temperature. These features eliminate the need for a filter array, previously thought necessary to detect different wavelength bands in a single PD selectively, enabling pixel-by-pixel tunable multi-spectral PDs.[254, 321, 332, 338, 482–492]

Unipolar barrier PDs with a tailored spectral response have been demonstrated in several ways. For example, tunnel-barrier-controlled band-engineered 2D vdW heterostructures can build unipolar barrier PDs,[254, 321, 483, 490, 491] by strategically designing each absorption, transport, and barrier layer to distinguish the UV, VIS, and IR ranges while suppressing surface leakage current, majority carrier dark current, and reinjected photocurrent. The absence of a depletion region minimizes generation–recombination current caused by Shockley–Read–Hall traps, and the unipolar barrier facilitates fast response times by enabling direct tunneling. In particular, a single PD with the unipolar barrier can switch the absorption layer and detect distinct cut-off wavelengths, enabling dual-band detection, as shown in Figure 8g.[332] Besides, a $Bi_2O_2Se/SnSe_2$ tunneling heterojunction has been explored operating across the VIS to NIR range.[490] Under reverse bias, enhanced IR absorption increases electron concentration and reduces the width of the space charge region. This light-assisted tunneling process offers excellent *D** and fast response speed.

A native oxidation layer can also be utilized to tune the spectral responsivity driven by photoexcited carrier transport across the interfacial tunnel barrier. For example, a graphene/Bi_2Se_3 heterointerface has been proposed for a hybrid photodetection mechanism that incorporates PVE and PGE, arising from the tunnel barrier formed at the interface due to the natural surface oxidation of Bi_2Se_3 during fabrication.[254] The interfacial tunnel barrier facilitates tunable carrier transport mechanisms from direct tunneling, FN tunneling, and thermionic emission. Furthermore, Dirac Fermions at the surfaces of graphene and Bi_2Se_3, with linear dispersion relations, enable broadband photodetection, extending to wavelengths of up to 4000 nm.

3.2.6. Reconfigurable Photonic Nanostructure Engineering

Unlike geometrically confined photonic nanostructures, whose spectral response is fixed during fabrication, reconfigurable photonic nanostructures enable post-fabrication electrical tunability, enhancing performance and enabling multifunctional operation.[493] These approaches leverage carrier-density modulation, excitonic resonance shifting, or plasmonic coupling in 2DMs.

For example, graphene has been explored for electrically tunable beam steering owing to its carrier-density-dependent optical conductivity. Whereas graphene is nearly transparent and offers broadband photoresponse,[494] the excitonic features of TMDs can be employed for beam steering, with h-BN acting as an atomically thin reflector, thereby enabling tunable phase patterning.[495] Metasurfaces integrated on the surface of graphene with a metallic back reflector are reported to feature channel conductivity modulated by the Fermi level, which governs single-gate electro-optic beam switching.[453] Furthermore, electronic states in layered structures shift the minimum of reflection spectra by free-carrier plasma resonance. For instance, embedding TMDs into microcavities, photonic crystals, and

Table 3. Comparison of requirements for scalable manufacturing of 2DM-based IR PDs. Transforming lab-scale prototypes into industrially applicable systems requires that the fabricated devices operate at standard temperatures, such as room temperature, remain stable for long lifetimes, and the fabrication process must be compatible with CMOS processes while ensuring wafer-level scalability.[496–502]

Device structure	Operating temperature [K]	Stability	Scalability	CMOS Compatibility
Nitride-doped MoS_2[344]	RT (≈300 K)	> 1 year	Device-level	Low (Exfoliation & Transfer)
$PdSe_2/MoTe_2$[307]	RT (≈300 K)	> 8000 cycles	Device-level	Low (Exfoliation & Transfer)
b-P/MoS_2/b-AsP[332]	RT (≈300 K) & 77 K	–	Device-level	Low (Exfoliation & Transfer)
graphene/b-P/MoS_2[345]	RT (≈300 K)	> 1 month	Device-level	Low (Exfoliation & Transfer)
b-P/SWCNT[503]	≈155 K	> 1 month	Array-level	Low (Exfoliation & Transfer)
graphene/PbS[504]	RT (≈300 K)	–	Array-level	Middle (CVD & Transfer)
HgTe/graphene[340]	RT (≈300 K)	> 1 month	Array-level	High (CVD & Printing)
graphene/Bi_2Te_3/GaAs[275]	RT (≈300 K)	> 1 month & 1000 cycles	Array-level	Challenging (MBE on GaAs)
graphene/h-BN[505]	RT (≈300 K)	–	Wafer-level	Middle (CVD & Transfer)
$PtTe_2$[259]	RT (≈300 K)	> 6 months	Wafer-level	High (CVD & CMOS process)

distributed Bragg reflectors (DBRs) gives rise to exciton-polariton modes whose resonance can be tuned by gate voltage, while coupling with metallic nanostructures induces plasmonic resonance. These collectively highlight the inherent electrical tunability of 2DMs, which transcends the limitations of photonic nanostructures.

4. Scalable Manufacturing of Spectrally Tunable 2DM-Based IR PDs

Although spectrally tunable 2DM-based PDs are emerging as key elements for intelligent optoelectronics, their transition from lab to fab remains hindered by scalability, complementary metal-oxide-semiconductor (CMOS) compatibility, and integration complexity, as summarized in **Table 3**. This section, along with **Figure 9**, outlines the general process challenges of integrating 2DMs and their heterostructures into PDs with nanophotonic architectures, then transitions to a focused discussion on application-specific requirements, particularly for spectral tunability. The discussion is organized into five core technical elements: platform, channel, contact, gate stack, and encapsulation. Furthermore, although not explored in depth in this section, ensuring device reliability is a critical requirement for the scalable manufacturing of 2DM-based IR PDs. For instance, suppressing defect states within the 2DMs, minimizing interface-trap states, and designing device geometries to prevent local high electric fields are crucial in mitigating degradation such as hysteresis, bias temperature instability (BTI) monitored by the threshold voltage shift, and hot carrier injection (HCI) evaluated by gate-induced drain leakage (GIDL). To ensure long-term stability, it is crucial to evaluate and monitor device reliability assessment throughout device integration systematically, such as time-dependent dielectric breakdown (TDDB) assessed via breakdown voltage or voltage ramping (Vramp), and high-temperature operating lifetime (HTOL) testing, while optimizing surrounding materials, interface properties, and device geometries. In particular, PDs must estimate endurance cycles, environmental stability, and the maximum optical power that can be detected without performance degradation.

4.1. General Integration Processes

Not initially developed for PDs, extensive process optimization efforts have been undertaken to transition 2DM-based devices from laboratory-scale demonstration to industry-scale manufacturing.[496–502] These lab-to-fab transition strategies, developed across various 2DM-based device platforms, provide a strong foundation that can be directly applied to the scalable integration of PDs as well. These established workflows, including wafer-scale growth, transfer, patterning, contact formation, and dielectric integration, offer valuable insights into the scalable realization of spectrally tunable PDs.

4.1.1. Growth and Transfer

High-performance IR PDs require crystalline and spatially uniform 2D semiconducting channels over a large area. Two main routes, mechanical exfoliation and direct synthesis via chemical vapor deposition (CVD), are employed.[389, 506–510] While exfoliation provides defect-free, high-quality layers, which are essential for proof-of-concept devices, it lacks scalability, reproducibility, and controllability. In contrast, CVD-based methods offer wafer-scale growth capability and better integration potential with existing semiconductor process workflows. However, they currently suffer from high defect density (≈ 10^{12} cm^{-2}), polycrystallinity, and limited control over uniformity.[511, 512]

The quality of the synthesized channel has a significant impact on the performance of a PD, particularly in minimizing i_d to achieve a low *NEP* and a high *D**. In conventional PDs based on Si photodiodes, atomic defect levels are typically < ≈1 per unit device, whereas 2DM-based PDs are still behind, with defect levels several orders of magnitude higher. Furthermore, the growth of 2DMs often requires high temperatures (> ≈600 °C) in reducing environments (e.g., H_2 atmosphere), which poses challenges for integration on temperature-sensitive dielectric substrates, such as SiO_2 or Si_3N_4.[513]

To mitigate thermal incompatibility, two main strategies have emerged. One approach is to develop low-temperature (< ≈500 °C) CVD processes that still yield high-quality monolayers. Another approach is to use advanced transfer techniques to transfer

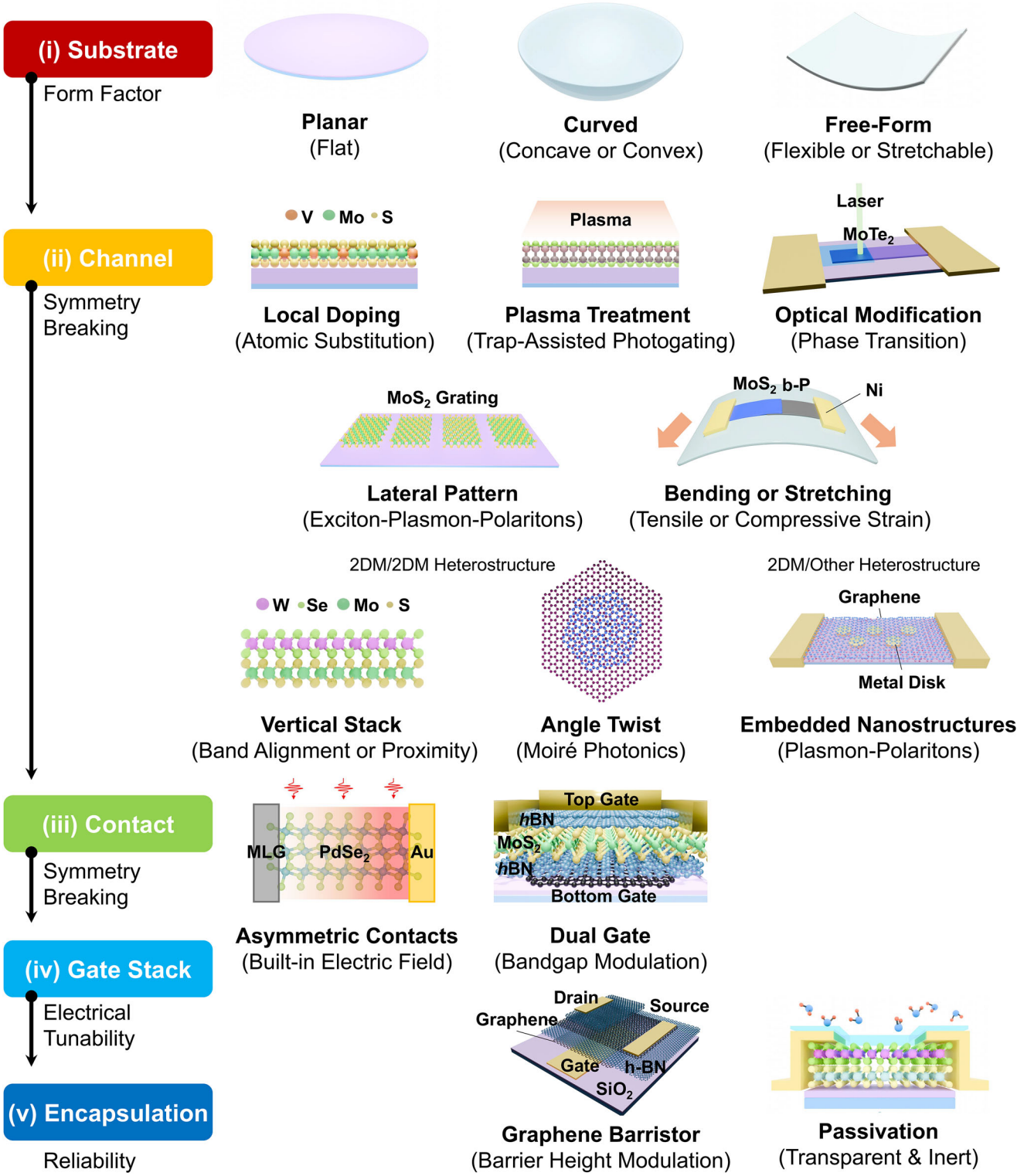

Figure 9. Schematic overview of key scalable integration strategies for spectrally tunable 2DM-based PDs. The integration flow is categorized into five core functional components. i) Substrate: Form factor classifications include planar, curved, and free-form geometries. ii) Channel: Symmetry breaking can be induced through local doping, plasma treatment, optical modification, lateral pattern, bending or stretching, vertical stack, angle twist, and embedded nanostructures. iii) Contact: Asymmetric contacts break inversion symmetry. iv) Gate Stack: Electrical tunability is enhanced with dual gate and graphene barristor architectures. v) Encapsulation: Transparent and chemically inert passivation layers ensure device reliability under ambient and thermal stress.

high-quality films grown on separate substrates to target wafers. Promising examples, such as polymer-assisted dry transfer, aim to suppress defect formation, reduce interfacial contamination, and improve alignment accuracy.[514–524] Continued research is needed to balance film integrity, throughput, and CMOS compatibility, enabling 2D semiconducting channels in large-area IR PD arrays.

4.1.2. Patterning

Photolithography defines the lateral geometry of 2D devices and enables pixel-level integration in PD arrays. However, conventional photolithography processes face significant limitations when applied to 2DMs due to their atomically thin nature and inherently weak adhesion to substrates. During key steps, such as photoresist development, 2D films are prone to wrinkling, delamination, or tearing due to capillary forces and solvent penetration, resulting in poor pattern fidelity and reduced device yield.

To overcome these limitations, adhesion lithography has emerged as a promising solution.[525] Mechanical stability during lithographic steps can be significantly improved by chemically modifying the substrate to modulate the adhesion energy between the 2DM layer and the underlying metal or oxide surface. Notably, this approach has demonstrated near-unity patterning yields across whole 6-inch wafers without requiring additional etching steps.

For removal of 2DMs after patterning, dry etching can be performed using reactive-ion etching (RIE), widely adopted in CMOS processes, with plasmas of O_2, CF_4, and Ar.[379, 415, 526, 527] The RIE enables anisotropic etching and precise patterning while maintaining compatibility with the CMOS infrastructure and preserving the structural integrity of the 2DM film. However, dry etching can introduce functional groups or leave edge regions in an undefined state, necessitating post-treatment steps to heal or passivate these regions.

Recently, a new approach defining open-space regions using PDMS molds has been proposed, addressing both the issues of pattern persistence and limited edge formation. 2DM can be selectively grown only within these open regions, generating well-defined patterns without etching. This bottom-up patterning method offers a promising approach to defining active regions without damage or lithography.[528, 529] To enable high-resolution patterning without compromising film integrity, lithography techniques must continue to evolve to address the unique surface chemistry and mechanical vulnerability of 2DMs.

4.1.3. Contact Formation

Forming reliable electrical contacts with 2D semiconductors for high on-state current and stable signals remains a significant challenge in device integration. In general, impurities or structural defects at the 2DM surface can create interface trap states (ITS) or metal-induced gap states (MIGS), which pin the Fermi level at the metal/2DM interface, thereby hindering work-function modulation or increasing contact resistance.[458, 460, 530, 531]

Extensive research over the past decade has led to significant advances in contact strategies, including interlayer contact, phase-engineered contact, and edge-plane contact.[532–534] The adsorbed contaminants, such as adsorbed water or hydrocarbon layers, induced by exposure of the 2DM surface to the atmosphere, can be minimized by depositing metal electrodes under ultra-high vacuum and transferring them onto the surface of 2D semiconductors. Therefore, to minimize interface damage and suppress ITS or MIGS, it is essential to deposit contact metals under mild conditions that preserve the vdW interface.[535–537] Recently, it has been reported that introducing semimetals with closely aligned Fermi levels in the conduction and valence bands of 2D semiconductors, such as Bi and Sb, can significantly reduce the Schottky barrier height and form an ohmic contact.[538, 539] Furthermore, the topological surface states, incorporated at the interface between 2D TSM and 2D semiconductor, effectively mitigate MIGS and improve broadband photodetection performance through the bulk photovoltaic effect in TMD by edge semimetal contacts.[188, 249–252]

Despite these advances, many of the proposed contact schemes remain difficult to implement in CMOS-compatible fabrication. For example, some 2D TSMs that provide very low contact resistance with 2D semiconductors are considered to have poor thermal stability or are incompatible with current fab processes, making them difficult to mass-produce.[389] Ultimately, achieving industrial-level reliability and low contact resistance will require co-optimization of material selection, interface chemistry, and scalable strategies.

4.1.4. Gate Dielectric Deposition

The deposition of gate dielectrics on 2DMs presents a significant challenge due to their chemically inert, dangling-bond-free surfaces. This often results in poor nucleation during atomic layer deposition (ALD), leading to discontinuous or defective dielectric films that degrade device performance.[540] In addition, uncontrolled interfaces can introduce ITS, increase leakage currents, and compromise electrostatic gating.

To address these issues, several strategies have been developed. One approach involves pre-depositing a metal seed layer or using surface functionalization techniques, such as ozone or plasma treatments, to enhance nucleation density and film uniformity.[541–543] These methods improve dielectric coverage, but the process must be controlled to minimize damage to the underlying 2DMs. A promising alternative is the use of in situ oxidation of transition-metal-rich 2D semiconductors. For example, Bi_2O_2Se can be thermally or chemically oxidized into $Bi_2Se_3O_5$, forming a conformal high-k dielectric layer that preserves the 2D interface.[544] This technology simplifies the process and ensures tight integration between the semiconductor and the gate dielectric, but has limitations in the material pool. This technique simplifies the processing and ensures the tight integration between the semiconductor and the gate insulator.

Despite these advances, challenges remain to achieve high breakdown fields, low interface-state densities, and mechanical stability under bending or thermal cycling, especially on flexible platforms. Continued efforts are needed to develop CMOS-compatible, scalable dielectric deposition methods that balance film quality, interface engineering, and device reliability.

4.2. Form Factor of the Substrate

The choice of substrate platform plays a crucial role in the design and performance of spectral tunable PDs, particularly when targeting flexible, stretchable, or curved integrated systems.[545] Rigid substrates such as Si or SiO_2 wafers remain the standard for prototyping and CMOS-compatible processing due to their mechanical robustness and compatibility with conventional semiconductor fabrication tools.

However, as IR PD applications expand to wearable electronics,[546] curved imagers,[547] and biomedical sensing platforms,[548] the demand for substrates that offer mechanical flexibility and optical transparency is rapidly increasing. To meet these requirements, recent studies have demonstrated the integration of 2DMs onto flexible polymer-based substrates, such as, polyethylene terephthalate (PET), polyethylene naphthalate (PEN), and polyimide (PI), or pre-shaped curved surfaces.[549–553] One notable example is a hemispherically curved image sensor array, demonstrated by transferring high-density MoS_2/graphene heterostructures onto a PDMS dome substrate.[547] The design emulated the geometry of the human eye and incorporated a truncated icosahedron architecture, including strain-isolation layers composed of Si_3N_4 and Al_2O_3. This structure mitigated buckling and local curvature effects, ensuring a uniform strain distribution and maintaining consistent electrical and optical responses across the curved surface.

Looking ahead, scalable integration into unconventional substrates should consider low-temperature processes, strain-adaptive electrode designs, strain-isolation layers, and mechanically robust encapsulation layers.[554, 555] Ensuring uniformity and long-term reliability under repeated bending and environmental exposures is also essential for commercial viability.

4.3. Symmetry Breaking in Channel

One of the most effective strategies to achieve spectral tunability in 2DM-based IR PDs is to manipulate the semiconducting channel's electronic band structure, including splitting or shifting energy levels. Symmetry breaking is a phenomenon in which a material's inherent symmetry is disrupted, introducing asymmetry and altering its electronic and optical properties. Such breaking can be intrinsic, due to the material's inherent structure or composition introduced during fabrication, or extrinsic, induced by external factors such as electric or magnetic fields. For example, introducing dopants into a semiconductor can break the symmetry of the host lattice, thereby altering the electronic band structure. Since symmetry breaking enables the tuning of semiconductor properties, it allows for the design of materials with specific functionalities, such as interband transitions at energies, dynamically shifting or broadening the spectral response by varying the joint density of states. In this subsection, we introduce several representative strategies in recent reports for symmetry breaking in the channel.

4.3.1. Local Doping

Spatially resolved doping in 2D semiconductors, including substitutional,[366, 556] molecular,[367, 557, 558] and electrostatic[559, 560] approaches, can modulate the local Fermi level and tune the potential landscape by breaking inversion symmetry, which is effective for controlling carrier polarity and density in the channel.

Although ion implantation remains a standard method for bulk semiconductors, it is not suitable for 2DMs due to severe lattice damage and interfacial degradation caused by high-energy ions and thermal processing.[365, 561, 562] To overcome limitations, various alternative doping techniques have been developed. Substitutional doping, for example, replacing neighboring tungsten (W) atoms in WSe_2 with vanadium (V) atoms, can create a stable atomic configuration that significantly modifies local symmetry.[366] Similarly, laser-assisted doping under controlled atmospheres enables spatially localized phosphorus doping in MoS_2, offering tunable thickness and carrier polarity.[556] These methods are desirable due to their compatibility with post-synthesis processing and potential for mask-free, site-selective doping.

Molecular charge transfer and electrostatic gating enable large-area, low-damage modulation of the Fermi level. While these alternative techniques show promise, significant challenges remain across doping methods in general, including maintaining mobility, controlling contact resistance, and achieving uniformity at scale.[563] Process-induced effects such as surface traps and interfacial roughness can seriously degrade electrical performance if not properly managed. The precise doping technologies are expected to play a critical role in enabling high-performance IR PDs and integrated logic-sensor platforms based on 2DMs.

4.3.2. Plasma Treatment

Plasma treatment offers a rapid and facile method for modifying the electrical and optical properties of 2DMs, eliminating the need for additional deposition or etching steps. Exposure of 2D semiconductors to mild plasma environments (e.g., CF_4, O_2/Ar) can break structural symmetry by introducing functional groups, atomic vacancies, or stoichiometric disorder. These defects locally distort the potential landscape and modify the band structure, often resulting in sub-bandgap states and enhanced NIR photoresponse.

Unlike conventional doping techniques, which typically involve high thermal budgets and multi-step integration, plasma-based approaches enable direct modification of the active layer at low temperatures, making them attractive for CMOS-compatible and monolithic integration of spectrally tunable PDs.

For example, O_2/Ar plasma treatment on monolayer MoS_2 forms surface MoO_x species that introduce PGE by modulating band alignment and suppressing recombination, enhancing i_{ph} and PL.[564] Similarly, CF_4 plasma treatment is leveraged to induce trap states in the InSe channel with Si_3N_4 passivation for configurable anti-ambipolar photoresponses to demonstrate multi-valued optoelectronic logic gates within a single device.[379] Such selective embedding of a charge-trap layer with plasma treatment highlights the potential of plasma-induced engineering.

Nevertheless, plasma treatment is highly sensitive to recipes and environmental factors, including dosage, exposure duration, and ambient gas chemistry. Thus, overprocessing can cause

irreversible lattice damage or etching, necessitating post-treatment steps such as thermal annealing, chemical passivation, or dielectric capping. While these processes are scalable and CMOS-compatible, ongoing improvements in uniformity, controllability of etching, doping, and trap-state formation, and environmental stability are crucial for reliable wafer-scale integration of 2DM-based IR PD arrays.

4.3.3. Optical Modification

Optical modification provides a rapid, low-temperature approach to tune the properties of 2DM-based PDs.[418, 420] While conventional processes, such as doping, annealing, and plasma treatment, have been widely used to tune band structures and defect states, they often lack selectivity in multilayer vdW heterostructures.[565] Optical modification, on the other hand, enables layer-specific control by adjusting laser parameters such as wavelength, power, and exposure time, without introducing chemicals or high thermal budgets.

For instance, in a heterostructure comprising $MoTe_2$, MoS_2, and h-BN stacked on SiO_2/Si, localized laser exposure induced layer thinning and defect healing in MoS_2, enhancing the PL intensity by more than 40 times.[380] Meanwhile, $MoTe_2$ showed decomposition and tellurium clustering, highlighting the layer-dependent reactivity. Such results demonstrate the potential of laser tuning for selective structural control. However, reproducibility and thermal confinement remain challenges. The use of capping layers, such as h-BN, can enhance thermal stability and protect against ambient degradation, while materials like graphene and Al_2O_3 may offer additional options.[52, 566, 567]

4.3.4. Lateral Pattern

Lateral patterning has become a promising fabrication technique for enabling spatial control of light–matter interaction, spectral and polarization selectivity, and enhanced light absorption in 2DM-based IR PDs. In contrast to vertical stacking approaches, it enables in-plane structural engineering, providing a practical solution for enhancing device performance and integration across the broadband IR range.

For example, a polarization-sensitive IR PD was realized using an InSe/MoS_2 heterostructure.[138] A MoS_2 grating, fabricated by e-beam lithography and dry etching, was overlaid on multilayer InSe. This patterning induces polarization sensitivity, a guided-mode resonance at 790 nm (TE polarization) and a plasmonic resonance at 960 nm (TM polarization), enhancing photocurrent without the need for metal structures. MoS_2, with its low optical loss and dielectric nature, proved advantageous for reducing thermal noise. However, such lateral-patterned structures are highly sensitive to fabrication conditions. Etch uniformity, sidewall roughness, and pattern fidelity directly affect optoelectronic performance.[568, 569] In particular, to mitigate plasma damage and thermal stress, optimized etching conditions such as high selectivity, low temperature, and damage-suppressing recipes are required. Post-patterning steps, including resist removal, interface cleaning, and transfer alignment, are critical for ensuring device reproducibility. Future efforts may explore scalable patterning techniques, such as self-aligned lithography and in situ growth patterning, as well as hybrid approaches that integrate doping gradients or embedded plasmonic structures to further expand spectral functionality.

4.3.5. Bending or Stretching

Strain engineering is a powerful strategy for inducing global inversion-symmetry breaking and for tuning the band structure of 2DMs. Localized mechanical deformation can induce bandgap shifts, modulate carrier effective masses, and enhance or suppress optical transitions depending on the magnitude and direction of the applied strain.

Typical approaches include uniaxial or biaxial stretching and compression of 2DMs stacked on flexible or elastomeric substrates.[546–548] Beyond global stretching, transferring monolayer 2DMs onto nanodomes, nanopillars, or wrinkled substrates creates spatially confined strain fields that locally modulate the band structure. This method enables pixel-level bandgap engineering and has been utilized to generate spatially varying photodetection across a single chip. Recent studies have demonstrated that few-layer WSe_2 and graphene were sequentially transferred onto ZnO nanorods with varying lengths from 300 to 600 nm using polypropylene carbonate (PPC) via a tilted-contact dry transfer method to prevent damage. After transfer, PPC was removed using heated acetone and critical point drying to achieve conformal contact without wrinkles or bubbles. This process naturally induced a position-dependent gradient strain field.[403] Nevertheless, this structure still relies on dry transfer, which poses challenges in alignment, interfacial cleanliness, and large-area reproducibility.

Therefore, future directions should explore strain-inducing processes that are compatible with CVD or epitaxial growth. Moreover, achieving precise directional control, gradient modulation, and uniformity over large areas remains an ongoing challenge for scalable device fabrication. Moreover, integrating strain-engineered 2DMs into scalable IR PD arrays will require innovations in substrate design, strain-isolation layers, and low-temperature transfer processes that minimize defect formation during conformal integration.

4.3.6. Vertical Stack and Angle Twist

2DM–based heterostructures offer a versatile platform for modulating the band structure and interlayer transition through interlayer coupling. Two major configurations, vertically stacked heterostructures and twisted bilayers, are particularly promising for enabling spectral tuning of PDs.

Carefully selected 2DMs in vertical stacks (e.g., MoS_2/WSe_2 or $MoTe_2$/MoS_2) enable type II band alignment and formation of interlayer excitons, leading to broader spectral absorption and novel symmetry-breaking transitions. Introducing a slight twist offset, i.e., the twisted bilayers, further creates a Moiré superlattice that reshapes the band structure. This Moiré potential gives rise to miniband formation and localized exciton states, resulting in narrow bands and spatially variable optical responses.

For example, to overcome the bandgap limitation of graphene, magic-angle twisted bilayer graphene has been demonstrated

to induce a tunable bandgap using electrostatic potential differences. In this configuration, interlayer screening can enhance photoconductivity by more than 4 times compared to conventional bilayer graphene; however, the precision of twist-angle control and scalability via dry transfer are limited.[346] As another example to improve angle control, the water vapor intercalation technique was introduced, where oxygen plasma-treated hydrophilic substrates facilitated smooth exfoliation and enabled twist angle alignment within a resolution of less than ≈1°, which provided a cleaner interface and tunable Moiré pattern formation.[570] Complementarily, a CVD-based heterosite nucleation approach has also been reported, where a second graphene layer is nucleated at the edge of a conventional layer by controlling the hydrogen flow and plasma energy, enabling the formation of a twist angle from 4° to 30° during the growth process, providing a clean interface and large-area integration potential.[571]

To enable practical device applications, future work must address reproducible large-area fabrication, thermal and mechanical robustness during processing, and seamless integration into CMOS-compatible workflows. Strategies such as automated transfer, low-temperature epitaxy, and interface passivation will be essential to unlock the full potential of vertically stacked heterostructures and to control their twist angles for spectrally tunable PDs.

4.3.7. Embedded Nanostructures

Plasmonic nanostructures have attracted considerable attention as a promising approach to improve the photoresponse sensitivity and wavelength- or polarization-selectivity (both wavelength- and polarization-dependent) of 2DM-based IR PDs. These structures enable the manipulation of incident light at sub-wavelength scales by coupling photons to collective electron oscillations at the metal/dielectric interfaces, resulting in localized surface plasmon resonance to enhance light–matter interaction within the active layer. One notable structure is a plasmonic cluster formed by embedding an array of metal nanodisks between upper and lower monolayer graphene sheets. This configuration creates a tightly confined optical field at the interface, enabling both efficient energy harvesting via substantial field enhancement and ultrafast carrier extraction due to graphene's high mobility. As a result, such hybrid systems show significant improvement in photocurrent generation and temporal response speed, even under low-intensity IR illumination.[333]

However, the performance of a 2DM-based IR PD with a plasmonic structure is highly dependent on its geometry. Its resonance wavelength, field distribution, and polarization selectivity are determined by parameters such as size, spacing, and periodicity. These nanoscale architectures require deep-UV or e-beam lithography for their delicate fabrication on the channel, imposing strict resolution constraints and throughput limitations.[572, 573] From an integration point of view, embedding nanostructures within PD stacks introduces an additional lithographic step that is not only cost-intensive but also challenges alignment accuracy, especially when scaled to large-area wafer-level fabrication. Additionally, variability in nanostructure dimensions or placement can introduce non-uniformities in device performance, complicating yield management in volume manufacturing.

To overcome these challenges while maintaining spectral tunability and scalability, various strategies, such as template-assisted nanofabrication, nanoimprint lithography, and bottom-up self-assembly, are being explored. These approaches offer the potential to pattern nanostructures over large areas with reduced complexity and lower cost, making them more compatible with industrial-scale integration pipelines.

4.4. Symmetry Breaking on Contact

Metal contacts to the semiconductor channel play a pivotal role in both charge injection and symmetry breaking in 2DM-based PDs. A common strategy is to use metals with different work functions at the metal/TMD interface. One recent practical approach is asymmetric metal contacts to induce bulk PVE or PTE.[239, 251, 378, 383–387] Notably, such asymmetry supports gate-tunability and device scalability without requiring complex gradient-doped junctions or split gates.

However, integrating asymmetric contacts poses several manufacturing challenges. Using dissimilar metal electrodes with different work functions and geometries requires multiple lithography and deposition steps, which increases process complexity and alignment requirements. Meanwhile, conventional deposition techniques, such as sputtering or e-beam evaporation, can damage or unintentionally dope the channel, requiring careful management of thermal and chemical compatibility between the contact metal and the underlying 2D semiconductor channel. Thus, asymmetric contacts offer an avenue for high-performance self-driven IR sensing, but scalable implementation requires careful co-optimization of materials, process flow, and interface engineering.

4.5. Electrical Tunability with Gate Stack

The gate stack in phototransistors not only allows modulation of the threshold voltage and on current but also plays a central role in controlling the spectral tunability due to a shift in the Fermi level and interlayer transition.[25–31]

4.5.1. Dual Gate

A dual-gate structure can modulate the Fermi level and carrier density by applying electric fields from each gate. The aligned graphene top and Si back gates induce a strong vertical electric field across the 2D semiconducting channel, leading to the Stark effect and enabling active tuning of the spectral response in the IR regime while minimizing optical loss.[352]

However, dual-gate integration often requires selective etching to open contact windows, necessitating high etch selectivity and interface integrity. Furthermore, the deposition of the top-gate metal can degrade the underlying channel. To address these issues, 2D conductors like graphene are favored for gate electrodes due to their vdW interface and minimal chemical reactivity.

4.5.2. Graphene Barristor

The graphene barristor is another promising architecture in which the graphene monolayer is in contact with a semiconducting channel or substrate, and the Schottky barrier height formed at the graphene/semiconductor interface is gate-tunable, enabling wavelength-specific photoresponse by IPE.[464, 478–481]

However, in the barristor structure that forms a graphene/semiconductor junction on a semiconducting substrate, a uniform dielectric film must be deposited on the substrate surface, the junction area must be etched to open the window, and the graphene monolayer experiences a step equal to the thickness of the dielectric film from the junction area to the dielectric film surface when the graphene is transferred. In other words, the large-area graphene is required to be transferred along this 3D surface morphology, and transferring a clean, abrupt, and low-defect graphene monolayer to form a homogeneous Schottky junction over wafer-scale processes remains challenging due to the inevitable interface traps induced by defects, wrinkles, local stress, and polymer residues during the large-area transfer of graphene onto the target substrate. These issues lead to Schottky barrier inhomogeneity in graphene/semiconductor junctions, which can compromise the stability and repeatability of gate modulation. Thus, integrating graphene barristor into scalable, manufacturable optoelectronic platforms requires further process optimization.

4.6. Reliability with Encapsulation

Encapsulation plays a crucial role in ensuring the long-term reliability and performance stability of 2D PDs, particularly for spectrally tunable devices that operate under diverse environmental and electrical conditions.[52, 567] Although 2D semiconductors are fundamentally stable, they can gradually degrade over time due to exposure to moisture, oxygen, or chemical contaminants (e.g., b-P, Te, etc.). Such exposure can lead to increased trap densities, shifts in doping levels, and long-term instability in the spectral response.

To mitigate these effects while preserving optical functionality, transparent inorganic materials such as SiO_2 and Al_2O_3 are commonly used as an encapsulation layer.[574] These materials are typically deposited via ALD, which provides conformal coverage and good scalability. Despite their excellent chemical stability and optical transparency, their intrinsic brittleness limits their application in flexible or stretchable PDs, where repeated mechanical deformation is expected. In contrast, organic encapsulants offer mechanical compliance and form factor adaptability, making them suitable for deformable platforms. However, they often exhibit poor barrier properties, particularly against moisture and oxygen permeation, limiting their effectiveness in harsh or long-term operating environments.

As alternatives, 2D dielectrics, such as h-BN, have emerged as promising encapsulation layers,[575, 576] offering atomically flat, chemically inert surfaces that serve as effective diffusion barriers while remaining compatible with the underlying 2D optoelectronic layer. Their vdW interface formation allows for defect-free coverage and can also serve multifunctional roles in dielectric or charge modulation.[505, 577]

Similarly, encapsulation must be compatible with low-temperature, high-throughput processes. Future research should focus on developing hybrid encapsulation stacks that combine the barrier properties of inorganics with the flexibility of polymers, while maintaining electrical neutrality and optical transparency.

5. Intelligent Optoelectronic Applications

Intelligent optoelectronic IR PDs are a part of smart multimodal sensors, equipped with functions such as data processing, self-diagnosis, decision-making, and communication. These devices enable the detection of visual or invisible information, collect, analyze, and process the relevant data, or transmit or receive it to an edge board or cloud server. For integration with AI, they require high performance, ultra-small size, lightweight design, and low power consumption to incorporate multiple built-in capabilities, operating as sensors while also functioning as processors and memories.[578, 579] These sensors not only detect physical parameters like light or heat, but also analyze that information so they can perform predefined actions or communicate data to other systems. This makes them more versatile, as they outperform or overtask conventional sensors. The tunable spectral response of 2DM-based IR PDs provides an excellent platform for computation-enabled or multifunctional hardware in intelligent sensors, particularly in optoelectronics enabled by multidimensional sensing, processing, and transceiving.

5.1. Computational Spectroscopy

IR spectroscopy has a wide range of applications in various fields, including material identification, chemical composition analysis, equipment testing, artwork authenticity assessment, biomedical diagnostics, food safety evaluation, healthcare, hygiene and quarantine, cell examination, drug screening, environmental monitoring, mineral exploration, astronomical observation, and space exploration.[580–583] Portable and on-site spectroscopic analysis technologies that overcome the difficulties of collecting and transporting samples without damaging or degrading their performance and enable rapid and flexible responses through real-time analysis have been attracting attention.[584, 585] Consequently, the demand for miniaturized spectrometers has been rapidly increasing.[1, 2] However, as spectrometers become smaller, physical limitations lead to degrade spectrometer performance and increased production costs. Despite their limitations, commercially available miniaturized spectrometers and portable hyperspectral cameras are priced too high, primarily because they use expensive, bulky optical elements for light dispersion.

Since 2020, computational spectrometers, combined with sensors capable of tunable wavelength-specific responsivity or with spectral-tunable optical filters, have attracted attention. Computational spectrometers are spectrometers that can obtain spectra without the need for separate light-dispersing elements, such as prisms, diffraction gratings, or filter arrays. Their operation scheme includes learning (calibrating R_λ, which is geometrically or electrically tunable, of multiple known monochromatic lights at different wavelengths), testing (measuring i_{ph}, which is geometrically or electrically tunable, of an unknown monochromatic

or broadband light), and computing (reconstructing spectra of an unknown monochromatic or broadband light) processes. This computational approach can meet both usability and spectrometer performance requirements, which are typically evaluated based on wavelength accuracy, spectral resolution, spectral range, and physical footprint.

Encoding a set of diverse spectral responsivity datasets represents a spectral responsivity matrix with low inter-state correlation. It is crucial for accurate spectral reconstruction in the presence of noise sources and calibration errors. Specifically, high variability in the spectral responsivity datasets trained at different variables, such as geometric and electrical modulations, enables efficient spectral reconstruction.[586] Recent progress in both hardware and software enables the miniaturization of spectrometers while maintaining their performance. Along with this, a variety of algorithms have been developed for spectral reconstruction, initially utilizing Tikhonov regularization and increasingly incorporating deep learning.[587–589] In general, spectral reconstruction algorithms can be categorized into machine learning algorithms and deep learning algorithms.[2]

Machine learning algorithms are expressed as mathematical models of objective functions that include decision variables. The objective function in a computational spectrometer consists of a residual term that controls the loss tolerance for the spectral responsivity matrix and a regularization term that imposes constraints on the spectral reconstruction. For residual terms, it depends on the noise contained in the spectral responsivity matrix. In particular, an objective function can adopt either mean absolute error (MAE) or mean squared error (MSE). MAE is used in environments with severe noise sources, leading to outlier datasets in the spectral responsivity matrix. In contrast, MSE is used in environments with Gaussian noise, typically in spectral reconstruction. The regularization term provides prior information about the desired solution or spectral composition. As a representative regularization term, the l_1 norm induces sparsity, similar to Lasso regression, while the l_2 norm prevents overfitting, as in Tikhonov regularization. Optimizing an objective function in a machine learning algorithm is crucial for spectral reconstruction and for finding a feasible solution in regression.

On the other hand, deep learning algorithms are typically implemented as neural networks with multiple layers. Each layer passes weight and bias information to the subsequent layers and extracts prediction values at the end of the network. The deep learning algorithm calculates the loss by comparing predicted and actual spectral values and updates the network via backpropagation. This neural network process is optimized for encoding spectral responsivity matrices for spectral reconstruction, with the advantage of learning complex statistical and structural priors that counteract noise sources and calibration errors, thereby enabling end-to-end mapping from raw measurements to reconstructed spectra, which is beyond the regularization used in machine learning algorithms.

Deep learning algorithms combined with 2DM-based IR PD can provide solutions for reconstructing spectra from complex mathematical models or high-dimensional input data that are physically challenging to interpret. Specifically, neural network algorithms are used to encode the tunable spectral response of 2DM-based IR PDs, ensuring uncorrelated datasets and thereby improving learning accuracy, which enables more efficient spectral reconstruction. For example, a recent study demonstrated that the strain-induced spectral response of WS_2 and WSe_2 can be encoded for spectral reconstruction using a multi-layer perceptron (MLP) neural network.[395] Another work highlighted dual-signal spectral reconstruction by encoding the gate tunability of both amplitude and relaxation time of the spectral photoresponse datasets of the semifloating MoS_2 homojunction through a deep neural network (DNN) to achieve high-fidelity spectral reconstruction.[354]

Computational spectrometers eliminate or reduce the physical requirements of light dispersion elements, addressing the trade-off between performance degradation and footprint miniaturization that is typically considered inevitable in conventional spectrometers. The programmable spectral responsivity of IR PDs enables IR computational spectrometers to be embedded in a single pixel on a chip. Numerous efforts have been made to optimize computational IR spectrometers, but they still face several technological barriers to commercialization.[350–353, 394, 590–593] Thus, the commercialization of high-performance IR computational spectrometers embedded in a single-pixel-on-a-chip could dramatically increase the potential for widespread spectroscopy applications in consumer products, such as smartphones and drones. With its significant impact on academia, industry, the economy, security, and the environment, spectroscopic technology can be applied in various areas of daily life for the public.

5.1.1. Portable Hyperspectral Imaging

Conventional image sensors typically employ either a charge-coupled device (CCD) or a CMOS architecture. CCDs use a global shutter and employ a single-shot acquisition strategy. In contrast, CMOS sensors enable pixel-level control, making them well-suited for high dynamic range (HDR) imaging. HDR imaging is often realized through a multi-shot approach, in which multiple images are captured at varying exposure times to cover a wide brightness range. This multi-shot approach enhances visual perception and is increasingly adopted in emerging technologies such as drones and autonomous driving systems.

Hyperspectral imaging (HSI) shares conceptual similarities with HDR imaging in its implementation. Like HDR, HSI often uses a multi-shot acquisition method, capturing individual frames at different spectral sensitivities. HSI collects multi-shot data in both the spatial and spectral domains, providing higher-resolution data in both domains. This allows HSI to offer superior capability for quantifying physical sensory quantities compared to conventional spectral imaging or conventional color imagers. In particular, 3D HSI, which incorporates spectral information in 2D, provides a spatial representation of the intensity of light spectra emitted or reflected by the measurement target.[594]

Building conventional HSI systems is considered to require lab-scale, or at least bench-top space, and optimizing performance and production costs presents significant technical challenges. Accordingly, there are two types of commercially available hyperspectral cameras. One is a portable hyperspectral camera equipped with a delicate light dispersion system, which is too expensive for the public to purchase. The other is a heavy, bulky hyperspectral camera that relies on a traditional diffraction grating, making it difficult to carry. Therefore, acquiring HSI typically

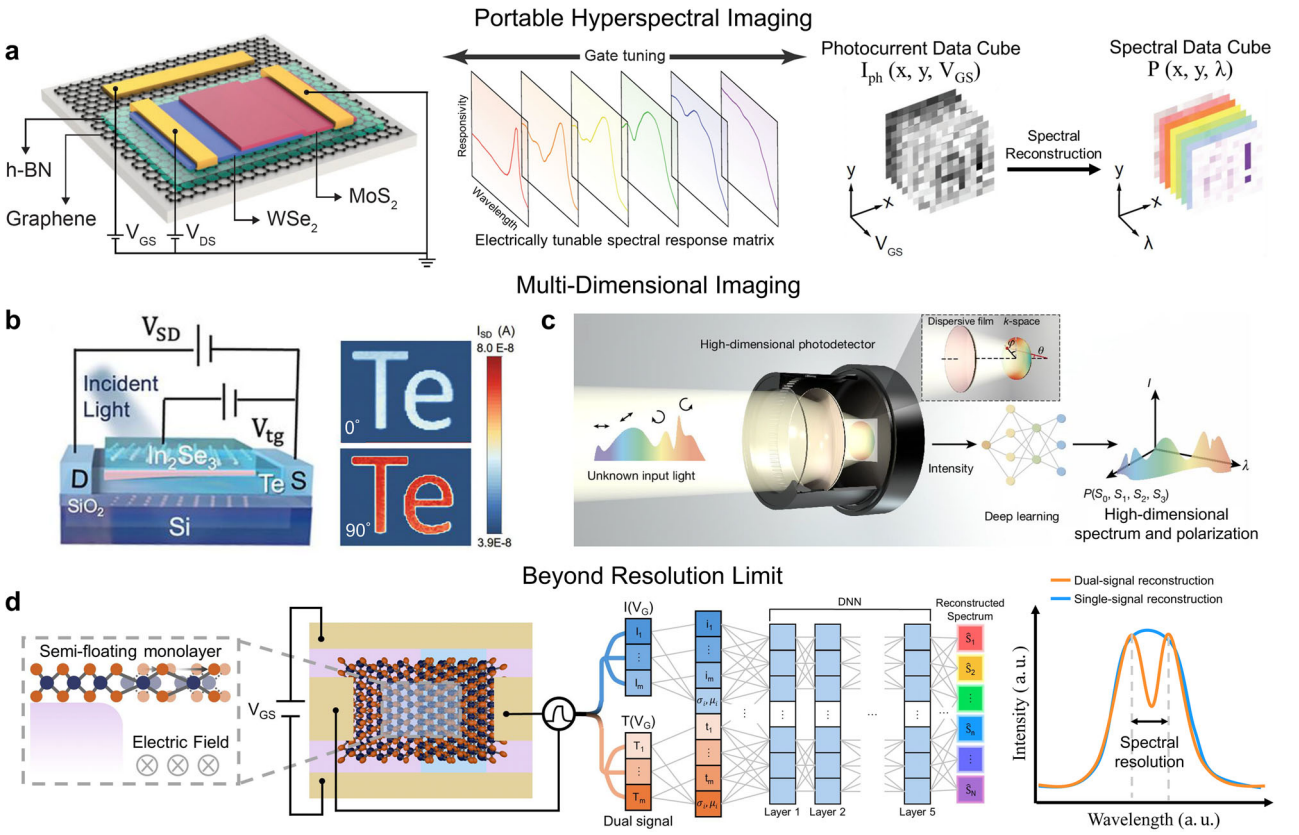

Figure 10. Computational spectroscopy. a) Operation scheme of computational spectrometers and hyperspectral images by leveraging electrically-tunable wavelength-specific photoresponse of 2DM-based PDs, allowing for spectrum reconstruction and spectral imaging based on the trained dataset of tunable spectral responsivity. b) Polarization imaging with a 2DM-based IR PD. c) Multi-dimensional imaging captures various optical information, including light intensity, wavelength, and polarization. d) Spectral resolution enhanced with dual-signal reconstruction using a semi-floating 2DM PD beyond the resolution limit. (a) Reproduced with permission.[350] Copyright 2022, AAAS. (b) Reproduced with permission.[232] Copyright 2024, Wiley-VCH. (c) Reproduced with permission.[610] Copyright 2024, Springer Nature. (d) Inspired by ref. [354].

involves collecting samples, transporting them to the laboratory, performing spectroscopic analysis, and taking HSI. Instead, the computational spectral reconstruction approach can be extended to reconstruct hyperspectral images by recovering hyperspectral information from RGB images. Various relevant approaches have been explored to enhance reconstruction accuracy and robustness of HSI.[595]

Although AI-integrated PDs with tunable spectral responsivity serve as powerful tools for computational spectroscopy, they do not always provide HSI unless a spectrometer is implemented within a single PD pixel, rather than in a PD or filter array. For example, in a CMOS image sensor (CIS)- based smartphone drug classification system using a convolutional neural network, a periodic array of band-pass filters is integrated to capture a 2D Raman spectral intensity map.[596] In their scheme, each CIS pixel with a periodic filter array collects individual spectral responsivity information, not spatial imaging information, providing spectroscopic analysis, rather than imaging. On the other hand, HSI in a CIS has been employed using a machine learning algorithm to quantify meat freshness as a measurable physical quantity.[588] In this case, they could provide HSI by acquiring data using a line-scan to construct 3D hyperspectral datasets. In other words, CIS must require a filter array (spatially) or a line scan (temporally) to obtain spectral responsivity in spatial dimensions, limiting the further miniaturization of HSI on a chip.[587, 589] In contrast, an array of 2DM-based PDs with electrically tunable spectral responsivity can perform HSI without a filter array or a line scan.

In particular, HSI in the IR region holds significant promise for the identification of chemical agents, assessment of gas flow, evaluation of soil quality, check of meat freshness, and detection of fever, owing to its ability to exploit molecular absorption and thermographic.[583, 597–605] Spectrally tunable 2DM-based IR PDs can offer single-pixel IR spectrometers, whose operating scheme is summarized in **Figure 10a**, allowing their array to feature spectrally resolved imaging at different wavelengths. This enables HSI-driven gas sensing powered by computational spectroscopy. This computational spectroscopy approach is highly versatile, providing both quantitative and qualitative analysis simultaneously in a single-shot imaging process, surpassing the capabilities of non-dispersive infrared (NDIR) gas sensors,[606–608] which are often used to analyze the concentration of a specific gas but cannot offer spectroscopic analysis or imaging. Recent work on a multiplexed NDIR gas-sensing system aims to replace bulky, costly bandpass filters with plasmonic metamaterial absorbers, enabling spectroscopic analysis on a chip.[609] However, it still does not offer imaging, as a spectrometer is implemented using

a multiplexed filter array. On the contrary, 2DM-based IR PDs with electrically tunable spectral responsivity can implement a spectrometer in a single pixel, allowing an array of 2DM-based IR PDs to perform single-shot HSI.[53]

5.1.2. Multi-Dimensional Imaging

Digital holography is an imaging technique that does not require photonic hardware components, such as an imaging lens, for the simultaneous capture of multi-dimensional imaging information.[611] Acquiring multiple optical information, including light intensity, wavelength, and polarization, with a single-pixel PD enables the acquisition of a holographic image of nonlinear light and a multi-dimensional image of incoherent light with a single-shot exposure, without the need for a filter array or a line scan, as shown in Figure 10b,c.[332, 485] However, given the fundamental limitation of conventional image sensors, which are inherently unable to capture multi-dimensional optical information, a comprehensive strategy is required to realize future multi-dimensional imaging systems.[612–615] A recent study demonstrated dispersion-assisted high-dimensional PDs with dielectric thin-film filter arrays and deep residual neural networks.[610] Thus, polarization-sensitive 2DMs with an electrically tunable spectral response[25–31] are ideal building blocks for in-pixel multi-dimensional imaging, such as 2D vdW heterostructures,[159, 224, 232–234, 305, 336, 341, 414, 616–618] or photonic nanostructures,[134–138, 140, 235, 276, 317, 318, 334, 430–447] unipolar barriers,[254, 321, 332, 482–490, 492] and 2DM-coupled CCDs or CISs.[504, 619]

2DMs and their heterostructures with intrinsic anisotropy are beneficial for encoding light polarization with polarization sensitivity and broadband response, opening a pathway for multi-dimensional imaging systems, particularly spectro-polarimeters.[231, 234] Polarized IR imaging has been demonstrated using an anisotropic Te PD with absorption spectra at different polarizations of light.[231] Similarly, a Te/Bi_2Se_3 PD has been reported to leverage both crystal anisotropy and topological surface states to enable polarization-resolved IR detection across an ultra-broadband range spanning from the UV to the MIR.[234] Importantly, these studies suggest that polarization is not merely additional information for light detection. Still, it can be merged into the fundamental axis of multi-dimensional images, such as wavelength in HSI.

The development of dual-band IR PDs operating at room temperature further miniaturizes multi-dimensional broadband imagers, enabling simultaneous detection in the NIR and MIR ranges.[620] A tandem structure formed in a b-P/MoS_2/Si vertical p-n-p heterojunction enables spectral blackbody detection due to wavelength-dependent coexisting spatio-temporal photocurrents. The ultralow crosstalk of 1.2% for MIR-to-NIR and 0.05% for NIR-to-MWIR is ensured by the filtering effect of thin-film Si and the barrier effect of MoS_2, allowing for independent readout of the dual-band information. Furthermore, ultrafast response times of several µs enable real-time analysis of transient phenomena in multi-dimensional datasets.

5.1.3. Beyond Resolution Limit

Spectral resolution is the most critical metric in spectrometers, reflecting the ability to distinguish fine features within the measured or reconstructed spectra. In traditional spectroscopy, spectral resolution and spectral range are typically constrained by the system's light dispersion elements. In computational spectroscopy, achieving improved spectral resolution and a wide spectral range within a limited footprint requires enhanced tunability of PD spectral responsivity and advanced spectral reconstruction algorithms.

Considerable progress has been made with 2DM-based single-pixel PD toward achieving a high spectral resolution or a wide spectral range approaching those of benchtop laboratory systems. Key advancements in t and their spectrometer performance metrics are summarized in **Table 4**. In general, gating to 2DMs enables substantial modulation of the Fermi level or bandgap, allowing tuning of PD spectral responsivity via excitonic absorption.[352] Furthermore, 2D vdW heterostructures facilitate tunable interlayer transport or interlayer transition for improving spectral resolution or spectral range.[350, 351, 590, 592, 621]

Several recent studies have further improved performance beyond the physical resolution limits. For example, a semi-floating MoS_2 homojunction is employed to achieve a spectral resolution of ≈1.2 nm through the utilization of dual signals, including photocurrent and relaxation time, which are processed by deep neural network algorithms, as illustrated in Figure 10d.[354] Their semi-floating structure induces locally varying strain in a single-pixel PD, which in turn alters the optical bandgap. Thus, intralayer exciton transport through the homojunction interface can increase the variability in spectral tunability at different gate voltages, due to the in-plane electric field influenced by local strain, leading to a dependence of both responsivity and transient behavior on the incident light wavelength and applied gate voltage. Another study exploited photonic quasi-bound states in the continuum (qBIC) for a bandstop strategy that can surpass the conventional bandpass strategy when qBIC-inspired spectrometers require a filter-array-based design. They demonstrated the spectral resolution of on the order of ≈1.7 nm.[622]

5.2. Artificial Vision

Artificial vision refers to the ability of machines to perceive, analyze, and interpret visual information, which is widely utilized in edge-level AI applications, including autonomous driving, medical diagnostics, industrial automation, and environmental monitoring.[623, 624] To address the growing demands for on-device intelligence, there has been an increasing focus on the development of emerging material platforms that facilitate enhanced functionality and seamless integration. In this regard, 2DMs emerge as a compelling solution for compact, multifunctional vision systems,[3–8] offering a platform for integrated sensing, memory, and processing due to their broadband absorption and electrical tunability.[227, 625, 626] Recent developments have demonstrated 2DM-based image sensors featuring tunable spectral response, in-sensor computing, and low power consumption, enabling adaptive and energy-efficient intelligent vision technologies.[6, 88]

Table 4. Performance comparison of computational spectrometers utilizing 2DM-based IR PDs. The spectral resolution indicates the ability to distinguish two narrow spectral peaks of a broadband spectrum separated by fine wavelength intervals, the wavelength accuracy represents the ability to resolve peak monochromatic wavelengths, and the spectral range defines the operational wavelength range of reconstructed spectra from computational spectrometers. Hence, the higher the spectral range multiplied by the footprint divided by the spectral resolution (or wavelength accuracy), the better the performance.

Year	Device structure (Tunable spectral engineering strategy)	Spectral range	Spectral resolution	Wavelength accuracy	Footprint
2021	b-P channel[352] (Gate-tunable bandgap due to Stark effect)	≈ 2000–9000 nm	≈ 80 nm (estimated)	–	9×16 μm^2
2022	Au intercalated ReS_2/Au/WSe_2 heterostructure[590] (Gate-tunable interlayer optical excitation)	≈ 1150–1470 nm	–	≈ 4.67 nm (estimated)	6×6 μm^2
2022	MoS_2/WSe_2 heterojunction[350] (Gate-tunable interlayer transport)	≈ 405–845 nm	≈ 3 nm	≈ 0.36 nm	22×8 μm^2
2024	MoS_2/b-P tunnel diode[351] (Bias-tunable thermionic emission and tunneling)	≈ 500–1600 nm	–	≈ 2 nm	30×20 μm^2
2025	p-i-n WSe_2 homojunction[353] (Bias-tunable nonlinear memristive photoresponse)	≈ 630–640 nm	≈ 2 nm	≈ 0.18 nm	4×9 μm^2
2025	$NbTe_2$/InSe waveguide-integrated on-chip[592] Gate- and bias-tunable photovoltaic mode)	≈ 500–720 nm	–	≈ 2.45 nm	5×5 μm^2
2024	SnS_2/$ReSe_2$ heterojunction[621] (Gate-tunable photocurrent via trap states)	≈ 400–800 nm	≈ 60 nm (estimated)	≈ 5 nm (estimated)	19×12 μm^2
2024	Semi-floating MoS_2 homojunction[354] (Gate-tunable photocurrent and relaxation time)	≈ 450–800 nm	≈ 1.2 nm	–	20×25 μm^2
2025	Controllable biaxial strain to MoS_2[395] (Strain-tunable bandgap and optical absorption)	≈ 400–800 nm	–	≈ 2.78 nm (estimated)	40×20 μm^2

5.2.1. Machine Vision

Machine vision has become pivotal in industrial automation and intelligent systems, facilitating high-precision visual inspection and real-time control. Conventionally, these systems have been integrated with cameras and sensors, along with rule-based image-processing algorithms, to perform tasks such as object detection and robotic guidance. Nonetheless, such systems generally depend on conventional von Neumann architectures, in which sense, memory and processing units are physically separated.[627] This structural division leads to a sequential workflow in which a camera captures visual information, digitizes it, and then transmits it to a processing unit that runs a machine learning algorithm.[628] As image resolution and frame rates increase, the need to transfer large volumes of redundant data results in high latency and power consumption, limiting real-time processing in delay-sensitive applications such as autonomous vehicles and industrial manufacturing.[629]

To overcome the limitations of physically separated sensing and processing units, recent research has explored the use of emerging material platforms, such as 2DMs, which offer unique opportunities for monolithic integration. Building on these material capabilities, a reconfigurable WSe_2 PD array with ambipolar conduction behavior has been demonstrated as a neural network image sensor for ultrafast machine vision, as shown in **Figure 11a**.[3] The device consists of a 3×3 array of monolayer WSe_2 pixels, where split-gate electrodes can individually modulate the photoresponsivity of each pixel.[630–632] This gate-tunable photoresponse effectively serves as a programmable synaptic weight, enabling the array to carry out in-sensor tasks such as classification and encoding of stylized letter patterns ("n," "v," and "z") via neural network inference.[3]

The gate tunability of the optoelectronic properties of 2DM allows for precise control of the spectral responsivity,[25–31] especially for reconfigurable neural network vision.[612–615, 635, 636] The Fermi-level shift through gating allows individual pixels within a PD array to function as weighted elements, analogous to the synaptic weights in a neural network.[629] As a result, the sensor itself can perform basic computational tasks such as weighted summation and feature extraction, enabling in-sensor computing for machine vision. As illustrated in Figure 11b, these systems can dramatically reduce data transfer overhead and latency for vision processing by embedding tunable spectral responsivity at the pixel level.[288, 578, 637]

Beyond electrically reconfigurable architecture, neuromorphic vision capabilities have been expanded to extreme operating conditions. For example, an ultrasensitive phototransistor array is demonstrated based on a momentum-conserved heterojunction comprising halide perovskite and Bi_2O_2Se for reliable in-sensor computing under dim illumination as low as 0.1 μW/cm^2, comparable to natural moonlight.[638] Furthermore, an all-optical neuromorphic retina operating in the MIR range based on a b-AsP/$MoTe_2$ heterostructure has been reported, which perceives MIR stimuli at 4.6 μm and encodes light intensity into spike trains using rate-based encoding, triggered by a stochastic NIR sampling terminal at 730 nm.[639] These developments highlight the versatility and scalability of 2DM-based vision systems across spectral ranges and illumination regimes.

5.2.2. Intelligent Imaging

Intelligent imaging systems, based on conventional machine vision, will further integrate AI to enable high-level

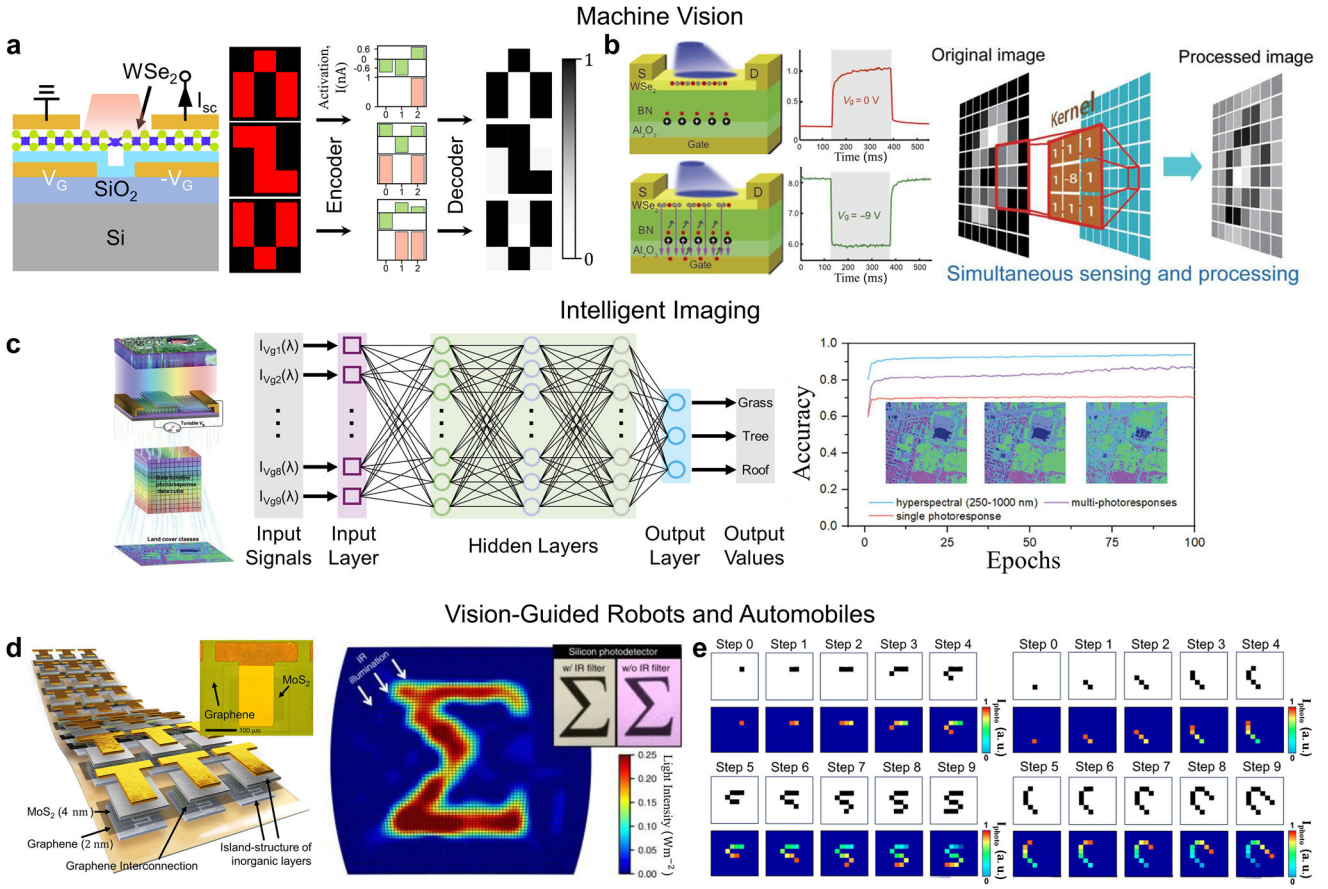

Figure 11. Artificial vision. a) A few-layer WSe_2-based lateral p-n junction photodiode with split-gate electrodes. Using this device, a 3 × 3 photodiode array was implemented to classify and encode 3 × 3 pixel letter images. b) The gate-tunable photoresponse of the WSe_2/h-BN/Al_2O_3 device mimics the hyperpolarization and depolarization of a bipolar cell. This temporal photoresponse enables the implementation of a retinomorphic vision sensor that simultaneously senses and processes. c) The $GaTe_{0.5}Se_{0.5}$/WSe_2-based PD with wide-spectral photoresponses (250 to 1000 nm). An artificial neural network trained on the multi-dimensional spectral responsivity matrix exhibits a classification accuracy of 0.87. d) The flexible phototransistor based on the MoS_2-graphene heterostructure and its extension to a curved image sensor array. This image sensor array can capture a clean sigma-shape image even under IR illumination due to the wide bandgap of MoS_2, which makes it immune to IR noise typically observed in conventional SI photodiodes (inset). e) In-sensor trajectory tracing of moving targets on the NbS_2/MoS_2 phototransistor-based image sensor array. (a) Inspired by ref. [3]. (b) Reproduced from [612]. Copyright 2020, AAAS under the CC BY-NC 4.0. (c) Inspired by ref. [633](Center), Reproduced from [627](Left, Right). Copyright 2024, Wiley-VCH under the CC BY 4.0. (d) Reproduced from [547]. Copyright 2017, Springer Nature under the CC BY 4.0. (e) Reproduced from [628]. Copyright 2023, Springer Nature under the CC BY 4.0.

decision-making in tasks such as medical diagnosis and autonomous driving.[640] Still, system-level bottlenecks remain major challenges for real-time deployment.[641, 642] To overcome these limitations, 2DM-based PDs have emerged as promising platforms for intelligent imaging. Recent studies have explored various approaches, including programmable image sensors,[643, 644] perceptual imagers,[633, 645] convolutional processors,[93, 646] and long-term image memory architectures.[621] These systems leverage the gate-tunable optoelectronic properties of 2DMs to enable adaptive, task-specific visual processing. In particular, the ability to dynamically modulate spectral responsivity enables 2DM-based platforms to address critical challenges in latency, power efficiency, and computational overhead that conventional hardware faces.

A representative example is a broadband (from 1.5 to 3 μm) b-P phototransistor array that enables both electrical and optical programming via charge storage in the HfO_2 layer.[643] By applying gate voltage pulses and optical stimuli, its mixed-mode responsivity programming was achieved, enabling local and remote control. This 3×4 array demonstrated convolutional image recognition with 92% classification accuracy. Due to its parallel imaging and programming schemes, the multifunctional b-P phototransistor array can realize a more complex artificial neural network. To address structural complexity, a SnS_2/$ReSe_2$ vdW heterostructure is proposed to exhibit long-term image memory with a retention time exceeding 10^4 s.[621] Unlike dielectric charge storage, the memory effect in this device arises from PGE enabled by trap states introduced by sulfur (2% in SnS_2) and rhenium (2.4% in $ReSe_2$) vacancies. While the device offers multifunctional operation at the single-pixel level, its spectral response is limited to 400–800 nm, thereby restricting its broader applicability.

Meanwhile, a $PdSe_2$/$MoTe_2$ heterostructure is demonstrated for broadband convolutional processing, capable of detecting

NIR signals up to 980 nm.[646] This device exploits gate-tunable band alignment and intensity-dependent photoresponse for wavelength-selective detection. Convolutional image encoding and remote sensing functionalities were demonstrated by applying different spatial kernels across the array. Extending this concept, an artificial neural network is trained to classify and recognize remote sensing targets using $GaTe_{0.5}Se_{0.5}/WSe_2$ vdW heterostructures, achieving classification across the NIR range up to 1000 nm.[633] As shown in Figure 11c, they achieved a classification accuracy of 87% with the trained multispectral photoresponse data cube.

5.2.3. Vision-Guided Robots and Automobiles

Vision-guided robotics and autonomous vehicles increasingly depend on intelligent imaging systems that integrate real-time perception, decision-making, and control to operate reliably in dynamic, unstructured environments.[647] To meet these demands, visual sensors must offer high spatial resolution, rapid response, and low power consumption, while maintaining robust performance under diverse lighting conditions and enabling the extraction of critical visual cues such as object localization, motion trajectories, and semantic identity.[623, 624]

Image sensors utilizing 2DM-based IR PDs optimized for robotics and vehicles offer multifunctionality, including broadband photoresponse, electrical tunability, and mechanical flexibility, for next-generation artificial vision.[547, 648–650] As shown in Figure 11d, a NbS_2/MoS_2 phototransistor is designed to simultaneously perform visual sensing, synaptic memory, and contrast enhancement, enabling static image processing within a neuromorphic sensor array.[634] Notably, the in-sensor registration of light trajectories has been experimentally demonstrated, allowing accurate dynamic trace extraction without external computation, as illustrated in Figure 11e.[634] Another study demonstrated that centimeter-level precision distance sensing is possible with only nW-level MIR detection.[651] The fusion of 2DM-based IR PDs with machine learning-assisted data interpretation will further elevate the responsiveness, autonomy, and intelligence of embedded vision platforms.

Recently, a differential perovskite hemispherical PD has pushed the boundaries of intelligent imaging by incorporating location tracking and color classification.[652] Similarly, a large-area phototransistor array based on 2D vdW heterojunctions can also be integrated on such a hemispherical substrate, demonstrating a promising direction for bio-inspired artificial vision in robotics and autonomous vehicles.

5.3. Computing

The traditional von Neumann architecture, in which memory and processors are physically separated, has struggled to handle the explosive increase in data volumes driven by AI-based real-time data collection. While numerous efforts have been made to develop parallel computing architectures that overcome the limitations of the von Neumann architecture, these have faced significant scalability issues due to the material limitations of silicon. In contrast, 2DMs provide a powerful means of overcoming these limitations.

In this subsection, we introduce four new computing paradigms that leverage the advantages of 2DMs. First, we discuss the status of the von Neumann architecture and highlight recent progress in optoelectronic computing enabled by 2DMs at the device level. Next, we review emerging non-von Neumann approaches, such as brain-inspired neuromorphic computing and optical quantum computing, with an emphasis on the role of 2DM-based devices in each.

5.3.1. Optoelectronic Computing

Optoelectronic computing refers to computing that employs devices capable of performing logic operations using optical signals or a combination of optical and electrical signals. Optical signals exhibit minimal resistive loss, facilitating bandwidths that exceed those of purely electrical interconnections and mitigating the data transmission bottleneck.[14, 653] 2DMs have emerged as a significant component of optoelectronic computing due to their remarkable light–matter interaction properties and their compatibility with the fabrication processes employed in chip manufacturing. For instance, graphene's high carrier mobility and broadband absorption enable electro-optic modulators with GHz–THz bandwidth.[141] Furthermore, its atomic thickness allows modulators to be placed directly atop waveguides for on-chip communication links. Similarly, TMDs, such as MoS_2 and WSe_2, can function as efficient PDs in the VIS to NIR range. These materials can convert optical signals into electrical currents in devices with a thickness of a few nanometers.[356]

The strong excitonic absorption and high optical nonlinearity of 2DMs further unlock optoelectronic and all-optical logic computing architectures.[269, 654] For instance, anti-ambipolar and bi-anti-ambipolar photoresponses have been reported in InSe transistors with a Si_3N_4 passivation layer, engineered by CF_4 plasma-induced trap states, which can realize optically configurable multi-valued logic gates. As shown in **Figure 12a**, the device utilizes wavelength-dependent carrier trapping and detrapping mechanisms to switch the negative differential transconductance from a single-peak to a dual-peak configuration, significantly increasing logic density and reducing energy consumption per operation.[379] Furthermore, optical chirality logic gates in monolayer MoS_2 have been demonstrated, harnessing nonlinear processes (four-wave mixing under chiral selection rules) to encode logic states, as shown in Figure 12b. By exploiting the spin angular momentum of photons, these devices execute Boolean operations entirely in the optical domain, eliminating the need for electrical interconnects. This all-optical approach offers fast switching, high bandwidth, and complete reconfigurability, while remaining compatible with hybrid integration with conventional electronic circuits.[655]

5.3.2. In-Sensor Computing

In-sensor computing integrates computational capabilities directly into sensors.[660–665] By preprocessing raw data at the point of capture, only highly refined information is transmitted to the central processor, significantly reducing bandwidth requirements and latency for tasks such as real-time image

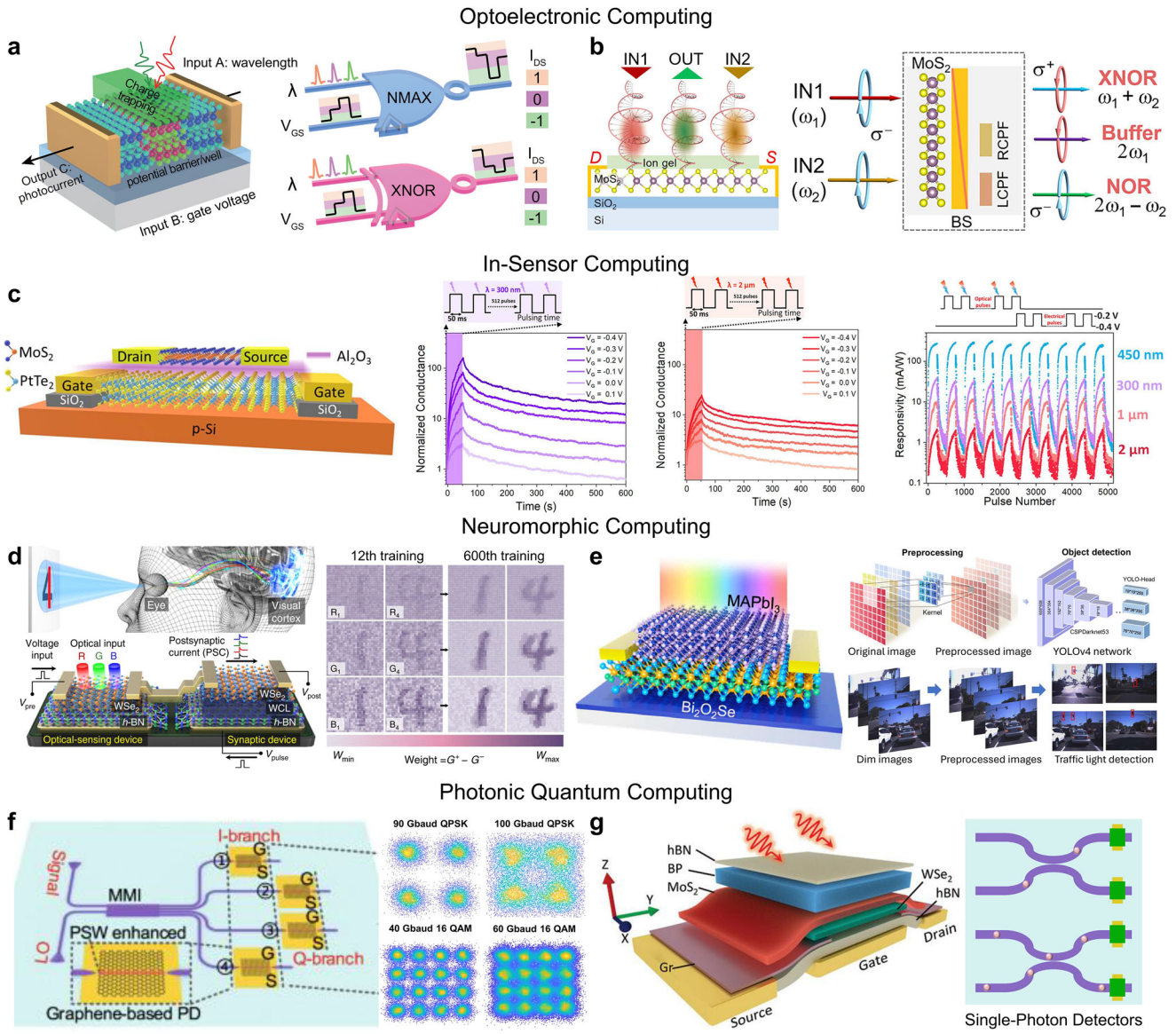

Figure 12. Computing. a) Anti-ambipolar phototransistors based on InSe enable multi-valued logic operations by exploiting wavelength- and gate-dependent photoresponses, allowing logic-level computation such as NMAX and XNOR. b) Chirality logic gate based on a MoS_2 FET with two incident circularly polarized beams and one output circularly polarized beam. (Left) Chirality logic gate based on a MoS_2 FET with two incident circularly polarized beams and one output circularly polarized beam. Multiple chirality XNOR, NOR, and Buffer (NOT) logic gates are implemented by inserting a beam splitter to detect simultaneously second-harmonic generation, four-wave mixing, and sum-frequency generation signals. c) In-sensor computing can perform processing using a multi-wavelength optoelectronic synapse that exhibits optical-stimulation-controlled short- and long-term potentiation, electrically driven long-term depression, and synaptic weight update across multiple wavelengths ranging from 300 nm to 2 μm for mixed-wavelength pattern recognition tasks. d) Optic-neural synaptic devices built from h-BN/WSe_2 heterostructures enable color-mixed pattern recognition by integrating wavelength-sensitive photodetection and programmable synaptic behavior, characterized by high conductance linearity and ultra-low energy consumption. e) Neuromorphic vision sensing based on $MAPbI_3/Bi_2O_2Se$ FET array effectively detects traffic lights by sequentially processing both dim and preprocessed images for real-time vision sensors. f) Graphene-on-plasmonic slot waveguide PDs and 90° optical hybrids operate as coherent receivers, enabling high-speed demodulation of advanced optical modulation formats. g) WSe_2/MoS_2/b-P FET can be used as a single-photon detector at the optical communication wavelength of 1550 nm for photonic quantum sensing. (a) Reproduced with permission. (Right)[379] Copyright 2024, AIP Publishing. (b) Reproduced from [653]. Copyright 2022, AAAS under the CC BY 4.0. (c) Reproduced with permission.[656] Copyright 2022, American Chemical Society (d) Reproduced from [655]. Copyright 2018, Springer Nature under the CC BY 4.0. (e) Reproduced from [638]. Copyright 2024, Springer Nature under the CC BY-NC-ND 4.0. (f) Reproduced from [656]. Copyright 2021, Springer Nature under the CC BY 4.0. (g) Reproduced with permission.[659] Copyright 2024, Wiley-VCH (Left).

recognition and environmental monitoring.[9–13] In typical artificial visual systems, the sensing unit is physically separated from the processing unit. In contrast, 2DM-based PDs inherently couple sensing and memory, allowing them to sense, store, and process optical data across a wide range of the electromagnetic spectrum.

For example, a phototransistor array with locally tunable photoresponse has been demonstrated to emulate the adaptive mechanisms of the human retina by leveraging engineered charge trap states. Under negative gate voltages, the device mimics rod cell behavior, exhibiting high sensitivity in low-light (scotopic) environments. In contrast, a positive gate voltage enables photopic adaptation, resembling the behavior of cone cells. It enables scotopic and photopic adaptation at the pixel level, resulting in contrast-enhanced imaging under dynamic lighting conditions and achieving an extended perception range of up to 199 dB within a single device.[649]

Figure 12c illustrates that excitatory postsynaptic currents (EPSCs) are uniquely distinguishable at different incident light wavelengths, which is promising for simultaneous sensing of multiband spectra. An intelligent artificial visual system has been demonstrated by featuring this multi-wavelength optoelectronic synapse enabled by VIS-sensitive MoS_2 channel with IR-sensitive $PtTe_2$/Si gate electrode, which is tested for recognizing single-color and multi-color patterns using UV, VIS, NIR, and IR wavelengths of light simultaneously. They reported that an in-sensor computing system can process visual information at the sensory terminal to eliminate redundant raw data, thereby enabling real-time pattern recognition.[656]

Furthermore, PDs with programmable spectral responsivity can be utilized to implement regression and classification directly upon light detection. An array of optical cavities with tunable resonant wavelengths has been demonstrated to implement the weighted inner product operation between the input spectrum and the trained spectral responsivity vector.[666] In this case, the PD obtains a correlation that enables it to detect light of a specific spectrum, eliminating the need for external signal reconstruction. For example, a heterostructure composed of partially overlapping p-type and n-type semiconductors exhibits gate-tunable bi-directional photoresponse in the NIR range, enabling real-time analog MAC operations directly at the sensor level, which is critical for low-latency image classification in edge AI systems.[667] In parallel, bi-directional PDs driven by wavelength or power-dependent polarity switching have been investigated as an alternative strategy for embedding computational functionality within the sensing layer, enabling optical information processing at the physical level.[13, 87–96] This method exemplifies a highly integrated physical-computational hybrid approach to miniaturized, energy-efficient spectroscopy.[10] As sensor and compute co-design improves, we expect to see 2DM in-sensor processors enabling ultra-low-power edge AI in everything from cameras to wearable biomedical devices.

Wavelength-dependent photoresponse is becoming increasingly crucial in in-sensor computing.[9–13] In particular, a sensor array based on 2DMs offers significant advantages for efficient, low-power execution in MIR target detection and recognition tasks.[668] A promising approach involves integrating in-memory computing and IR PD on a chip. For example, a b-P/MoS_2/h-BN/graphene heterostructure features dual functionality, combining ultrafast 20 ns operation in flash memory with exceptionally low energy consumption per operation of 1.8 fJ. The device leverages these capabilities to successfully enable object detection and recognition in the MIR region, providing enhanced accuracy in determining object location, classification, and type. Another study demonstrated integrated in-memory and in-sensor computing with artificial vision based on an optoelectronic ferroelectric transistor constructed from a SnS_2/h-BN/$CuInP_2S_6$ heterostructure.[669] The optoelectronic ferroelectric transistor exhibited electrically and optically switchable upward and downward polarization states by regulating the carrier concentration in the channel via positive and negative gate voltages. Their integrated computing system achieves 7-bit memory-state resolution with 128 levels, thereby demonstrating synaptic functions such as paired-pulse facilitation, short-term and long-term plasticity, and Pavlovian conditioning, with MNIST classification accuracy of 93.62%.

It is worthwhile to note that while the system-level advantages of 2DM-based IR PDs and their tunable spectral engineering for in-sensor computing have been discussed here, their transition from laboratory prototypes to practical implementations necessitates addressing critical bottlenecks to meet benchmarks set by mature CIS technologies. In particular, achieving high SNR with sub-electron noise in low-light environments and high energy efficiency of less than 10 pJ per pixel for edge computing is critical, which requires device-to-circuit optimization to increase conversion gain, reduce Flicker noise, and implement non-destructive readout.[670, 671]

5.3.3. Neuromorphic Computing

Neuromorphic computing is a non-von Neumann paradigm inspired by the structure and function of the brain. In a neuromorphic system, networks of artificial neurons and synapses process information in parallel, communicating via analog signals or spiking events rather than step-by-step binary logic.[672] A salient feature of the model is the co-localization of computation and memory. Each synapse in the network serves both a storage function for weights and a computational role, akin to the dual functions of neurons in biological neural networks. This tight integration eliminates the conventional separation of logic and memory, circumventing the von Neumann bottleneck. Neuromorphic architectures demonstrate proficiency in tasks such as pattern recognition, sensory data processing, and machine learning, domains in which the brain's model of massive parallelism and adaptive learning confers a distinct advantage. However, constructing neuromorphic hardware requires electronic devices capable of emulating the behavior of neurons and synapses. Such devices may include those that integrate signals and "fire" when a threshold is attained (neuron-like) or those that undergo a gradual change in conductance in response to stimuli, thereby demonstrating long-term plasticity (synapse-like).[673, 674]

2DMs have demonstrated considerable potential by facilitating high-performance artificial synapses and neurons. The most common approach is 2DM-based memristors to emulate synapses, which inherently offer switchable resistance states that can serve as synaptic weights in a neural network. 2DM-based memristors often support multiple intermediate resistance

states and undergo continuous updates. These properties are imperative for simulating synaptic plasticity (i.e., learning) with analog fidelity. These synaptic functions, including short-term plasticity (STP), long-term plasticity (LTP), and spike-timing-dependent plasticity (STDP), have been extensively reviewed across optoelectronic synaptic platforms based on 2DMs, where optical or electrical stimuli are employed to modulate synaptic weights and emulate biologically inspired plasticity behaviors.[291, 353, 673–677] These photonic memristors, so-called optomemristive feedback neurons, have been investigated as promising approaches for high-bandwidth and low-power parallelism, enabling wavelength-dependent neural operations and scalable photonic architectures that utilize both 2DMs and non-2DMs.[678–681]

A notable implementation is a multi-wavelength optoelectronic synapse constructed from monolayer MoS_2 and IR-sensitive $PtTe_2$, which enables color-resolved synaptic responses across the UV-IR spectrum and facilitates mixed-color pattern recognition by leveraging synaptic weight modulation.[656] Another study reported an optoelectronic synapse regulated by a phase transition of VO_2 based on a VO_2/graphene heterostructure for high-fidelity recognition tasks.[682] A two-terminal broadband optoelectronic synapse has also been reported to enable multiple synaptic behaviors, including excitatory postsynaptic currents, spike-number-dependent plasticity, and transitions between short-term and long-term memory. These optoelectronic synaptic devices support polarization-sensitive multispectral sensing and the generation of optical kernels for convolutional preprocessing.[657, 683, 684] With a 6×6 array configuration, classification accuracy exceeding 90 % has been achieved even under dim light conditions, demonstrating suitability for compact neuromorphic vision architectures, as depicted in Figure 12d.[661]

An alternative approach for optoelectronic synapses without gating has been demonstrated using defect-engineered heterostructures. For example, a curved MoS_2 dome-shaped PD over a defect-rich Fe_3S_4 core exhibited memory times up to 800 s under pulsed illumination, with enhanced charge trapping enabled by synergistic interactions between intrinsic defects and the heterointerface. The device enables high-efficiency recognition under simplified device configurations, underscoring the intrinsic-defect-based architectures for compact neuromorphic vision systems.[685] Another study demonstrated the construction of a high-precision multibit optoelectronic synapse using a ReS_2/h-BN/graphene heterostructure, which enables 1024 discrete optical conductance levels with 10-bit resolution. The device demonstrated STDP with an ultralow energy consumption of ≈500 fJ per spike.[686] A neuromorphic photoelectric memory based on a ReS_2/WSe_2 heterostructure with sulfur vacancies in ReS_2 further demonstrated dual-mode operation for sensing and memory, enabling digit recognition tasks with ≈94.9 % accuracy on the MNIST dataset after only 20 training epochs. Sulfur vacancies induced by light exposure and electric field can synergistically modulate carrier transport within the channel.[687] Furthermore, a reconfigurable phototransistor integrating halide perovskites and Bi_2O_2Se is used to perform analog MAC operations under dim light illumination,[638] as shown in Figure 12e. IR-triggered retinomorphic artificial synapse based on a WSe_2/InAs heterojunction also exhibits a synaptic behavior like STDP analogous to the human retina at 1060 nm in the short-wavelength IR (SWIR) range.[688] Optoelectronic synapses based on 2D TMD gradient alloys exhibit ≈161 % paired-pulse facilitation, stimulus-dependent transitions from short-term to long-term plasticity, emulation of brain-like learning processes, and simulation of neuromorphic vision in an artificial neural network for handwritten digit recognition with over ≈95.6 % accuracy.[689] Finally, a free-space optoelectronic synapse based on a bare 2D MoS_2 channel has demonstrated programmable modulation of nonlinear optical signals. Synergistic excitation pathways, including transitions from two-photon absorption to synergistic excited-state absorption, enable tunable operations in an artificial neural network. Weight encoding was achieved through pulse delay and intensity, resulting in operating durations as fast as ≈5.47 ps and energy consumption ranging from ≈5.12 to ≈9.12 pJ per operation.[690] Neuromorphic computing with 2DMs thus represents a convergence of advanced device physics and architecture: memristors and transistors built from atomic layers provide the analog memory and nonlinear response needed to realize neural networks in hardware physically.[9]

5.3.4. Photonic Quantum Computing

Photonic quantum computing represents a radical departure from conventional computing paradigms, leveraging quantum states of light (photons) to perform computational tasks. In quantum computing, information is encoded in qubits, which can exist in superposition states.[691] The entanglement between qubits facilitates computations that would be impracticable for classical computers. Photons have been identified as particularly effective carriers of qubits for specific quantum computing applications, such as quantum communication and linear optical quantum computing. This is due to their high transmission speed, minimal interaction with their environment, which reduces decoherence, and their ability to be manipulated using optical components. The challenge, however, lies in implementing photon sources and interactions that enable universal quantum logic. Key requirements include single-photon sources to generate qubits, high-efficiency linear optical elements such as beamsplitters and phase shifters, nonlinear processes to enact two-qubit gates (typically via measurement-induced effects or optical nonlinearities), and single-photon detectors, as depicted in Figure 12g.

Since 2DMs have been extensively explored for generating, manipulating, and detecting light with coherent control of individual photons, such as single-photon emission and broadband optical nonlinearity, the advances in 2DMs have had a considerable impact on integrated quantum photonics, offering scalable platforms for quantum applications. These capabilities underscore their potential in realizing on-chip quantum information processing beyond conventional bulk materials.[126] Recent advances in nonlinear optics with 2DMs have established their role as promising candidates for integrated photonic platforms, owing to their broadband optical responses, high third-order nonlinear susceptibilities, and compatibility with Si photonics.[692] In one approach, high-harmonic generation has been experimentally demonstrated in monolayer MoS_2, where delay-modulated femtosecond pump-probe control enables a tunable third- to

fifth-harmonic response with a modulation depth of up to 95%. This result reveals a pathway for ultrafast state encoding based on optical coherence and nonlinear dynamics in atomic-scale materials.[693] Further studies have realized nonlinear second-order and third-order photonic TIs, where light is confined in corner states or along domain walls. By tuning the phase delay and lattice symmetry, mode switching and logic operations can be achieved. These topological photonic devices offer controllable light confinement for quantum routing and information control, as illustrated in Figure 12f.[694, 695]

Building on these developments, comprehensive theoretical frameworks and experimental realizations of nonlinear topological photonic systems have been established, in which optical nonlinearities dynamically modulate nontrivial band structures and edge-localized modes. These systems enable soliton-like edge states, nonlinear topological transitions, and robust light transport under intense excitation conditions, enriching the material and device paradigm for integrated photonic quantum platforms.[696] Moreover, a multilayer $PtSe_2$ PD grown directly on Si photonic waveguides has demonstrated R_λ up to 11 m A · W^{-1} in the 1550 nm range, with FIR measurements extending to 28 µm. This integration enables potential on-chip interfacing between IR sensing and quantum photonic circuits, satisfying thermal budget and CMOS compatibility constraints.[697] In another system, optical Tamm states were engineered within Sb_2Te_3 thin films, enhancing the third harmonic generation via boundary-localized field confinement. The demonstrated field enhancement opens new directions for quantum signal amplification in photonic non-von Neumann architectures.[278] Recent advances in on-chip nonlinear photonic integration using 2DMs have further enriched the toolkit for photonic quantum computing, particularly by enabling compact, reconfigurable photonic platforms. Through hybrid integration with Si and other photonic substrates, 2DMs such as TMDs and b-P offer enhanced nonlinear responses, broadband tunability, and compatibility with CMOS fabrication, thereby expanding the applicability of nonlinear quantum photonics beyond conventional bulk systems.[15]

5.4. Communication

As global demand for fast, reliable data transmission continues to grow, communication technologies are evolving rapidly to keep pace. The surge in internet traffic, big data, data center, cloud computing, and AI is placing increasing pressure on modern computing systems to deliver higher speed, greater energy efficiency, and broader bandwidth. Conventional electrical interconnects are increasingly limited by signal loss, heat generation, and bandwidth constraints. Above all, they cannot support long-distance data transmission. In contrast, optical communication offers significant advantages, including high speed, low power consumption, large data throughput, and long-range data transmission. Especially in data centers and edge AI systems, where efficient transceivers are needed to link memory and processor, thus emerging as a core technology to meet future performance demands. In line with this trend, 2DM-based IR PDs and their spectral tunability provide a range of solutions in communication technologies.

5.4.1. Telecommunication

The rapid increase in demand for the Internet of Things, big data, and AI has driven the development of high-speed, low-power, and broadband optical communication technologies that process information in photonic integrated circuits and transmit it over optical fibers. 2DM is favorable for vdW integration and exhibits excellent compatibility with existing materials used in photonic integrated circuits, such as Si,[337, 445, 698–700] Si_3N_4,[701] $LiNbO_3$,[702] and InP.[703]

As illustrated in **Figure 13a**, integrating 2DM-based IR PDs on photonic integrated circuits benefits from both evanescent wave enhancement and efficient photocurrent collection, without issues related to lattice mismatch. A recent study demonstrated a waveguide-integrated IR PD operating at 2 µm based on a $Te/MoTe_2$ heterojunction, achieving a bandwidth of 36 MHz and supporting low-noise detection beyond standard communication bands.[337] In another example, a waveguide-integrated Te PD has been developed on a lithium niobate-on-insulator (LNOI) platform, delivering a 3 dB bandwidth of ≈2 GHz at 1550 nm wavelength.[702] Expanding the functionality of waveguide-integrated IR PDs, optoelectronic logic gates have been demonstrated by employing a triple waveguide design where an individual PD based on b-P is integrated into each waveguide. Three channels perform reconfigurable linear (AND, OR, NOT, NAND, NOR) and nonlinear (XOR and XNOR) logic operations with a 3 dB bandwidth of 230 MHz in the communication band at 1.55 µm, promising for encrypted communications.[704]

Beyond Si and LNOI, 2DMs offer the possibility of new photonic integration platforms for on-chip light propagation, emission, and detection. For example, as shown in Figure 13b, low-loss passive waveguides with MoS_2 and on-chip light sources and PDs with InSe have been demonstrated to exhibit a low propagation loss of 0.02 dB $µm^{-1}$.[705] 2DMs, such as graphene and b-P, have been explored for tunable NIR, SWIR, and MIR emitters that can modulate emission wavelengths in response to external stimuli, including electric fields and strain, and enhance light intensity through photonic architectures, like cavities and waveguides.[83, 208, 232, 239, 269, 706, 707] Furthermore, a recent study reported an inverse-designed wavelength demultiplexer capable of separating three distinct emission wavelengths (620, 750, and 870 nm) through excitonic PL sorting across the WS_2/WSe_2 heterostructure.[708] They leverage gradient-based optimization algorithms to achieve non-intuitive waveguide geometries, enabling efficient routing of WS_2 monolayer excitons (620 nm), WSe_2 monolayer excitons (750 nm), and interlayer excitons (870 nm) into dedicated output channels.

Likewise, 2DMs integrated into photonic integrated circuits or photonic architectures are opening new routes for the future of optical telecommunications. 2DMs not only enhance the performance of IR PDs for photonic integrated circuits but also offer versatile functionalities such as optoelectronic logic and signal processing. Their compatibility with existing photonic integrated circuit platforms and the ability to transmit light at high

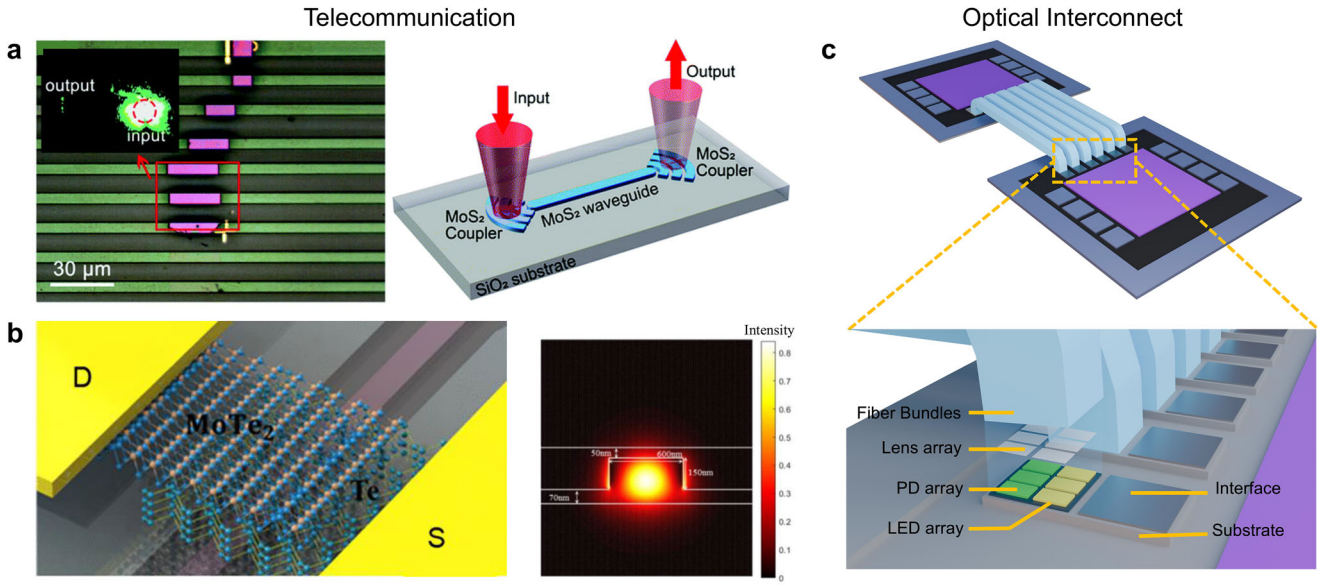

Figure 13. Communication. a) Left: Schematic of a waveguide-integrated Te/$MoTe_2$ PD. Right: Simulated transverse electric mode intensity in the designed waveguide. b) Left: Optical microscope image of MoS_2 embedded in the middle of each Si_3N_4 waveguide. The bright green region corresponds to the Si_3N_4 waveguide, and the bright purple region represents the MoS_2 buried waveguide covered by the Si_3N_4 layer on top. Right: Schematic of a MoS_2 waveguide integrated with grating couplers. c) Schematic of optoelectronic transceivers consisting of PD and LED arrays. (a) Reproduced from ref. [705]. Copyright 2022, Royal Society of Chemistry under the CC BY 3.0. (b) Reproduced with permission.[337] Copyright 2024, American Chemical Society.

speed and low loss enable the development of on-chip telecommunication systems with improved performance, including GHz-level operational bandwidth and sub-nanosecond response time.[14–16]

5.4.2. Optical Interconnect

AI data centers and their cloud services require intensive handling of large datasets for AI model training and inference, resulting in rapid annual increases in power consumption. As a result, ≈40% of AI data centers are expected to experience power shortages. Electrical interconnects suffer from intrinsic issues related to resistive losses, capacitive loading, impedance mismatches, and excessive heat generation. These physical constraints degrade data bandwidth, signal integrity, and energy efficiency, particularly at the chip-to-chip and memory-to-processor interfaces in AI accelerator architectures. As AI workloads grow in data intensity and real-time responsiveness, the transition from electrical to optical signaling is not only advantageous, but inevitable.[709]

Recent approaches utilize photonic optical links to connect processors and high-bandwidth memory modules, thereby mitigating the data bottlenecks characteristic of modern AI workloads. Unlike electron-based signaling, photonic communication utilizes light transmission through dielectric waveguides or optical fibers, which dramatically reduces signal loss over distance and enables high bandwidth with minimal power dissipation. Moreover, optical links are almost immune to electromagnetic interference and resistive heating issues, making them ideal for dense computing environments with stringent thermal budgets. Advances in photonic integrated circuits (PICs) have enabled the fabrication of optical transceivers comprising a library of passive and active photonic components such as waveguides, optical modulators, grating couplers, and PDs, combined with off-chip lasers via optical fibers.[710–712] In particular, wavelength division multiplexing (WDM) enables the parallel transmission of multiple data channels over a single optical fiber by encoding data onto different wavelengths, thereby vastly increasing the aggregate bandwidth without expanding the physical footprint.[713] These optical links demonstrate the ability to scale to terabit-per-second (Tbps) bandwidths per link, with significantly lower energy per bit than Cu-based interconnect.[714–716]

Despite these advantages, several technical challenges remain for PIC-based optical transceivers. Since PICs require lasers as light sources, they are often off-chip due to their CMOS incompatibility, resulting in alignment losses and input/output (I/O) limitations. Si-based PICs are CMOS-compatible but vulnerable to voltage and temperature fluctuations, and static electricity generated by friction can cause unwanted oscillations and noise. In particular, microring resonators and optical modulators face signal distortion when integrated with electronic circuits.

An emerging alternative approach involves optoelectronic transceivers based on micro light-emitting diodes (μLEDs) and PDs, as illustrated in Figure 13c. The conventional architecture utilizes GaN μLEDs and Si PDs. Here, GaN μLED arrays eliminate the need for external lasers and reduce optical loss by minimizing coupling interfaces, and Si PD arrays simplify photonic routing. This architecture enables compact, low-cost, and scalable optical interconnect without the need for complex photonic components in PICs,[717–719] making it ideal for edge AI applications.[720] However, these optoelectronic transceivers

still require optoelectronic conversion that introduces latency. Hence, the current implementation method has limited overall data throughput due to the lack of WDM functionality, but has garnered attention as a next-generation optical interconnect because it is advantageous for high-density I/O channels and ultralow-power data transceiving.

2DMs feature strong potential for integration into PIC components, such as waveguides and optical modulators.[14, 337, 699, 700, 702, 721–723] These are beneficial to manage polarization or nonlinear optical effects in PICs for optical transceivers.[15, 704, 705, 724–726] Moreover, they exhibit exceptional performance in both IR LEDs and IR PDs with their spectral tunability and environmental stability.[83, 208, 232, 239, 269, 706, 707] For monolithic integration of optoelectronic transceivers, 2DM-based IR LEDs and IR PDs can be integrated on a chip by employing an electrostatic split-gate architecture with two operational modes, emission and detection.[82, 83, 269, 445, 706, 727–729] Furthermore, tunable spectral engineering in 2DM-based IR PDs will allow WDM in optoelectronic transceivers.

6. Conclusion and Outlook

Intelligent optoelectronic applications either benefit from AI or provide significant advantages to AI. Still, their core functionality relies on the broadband spectral-tuning capabilities of IR PDs to collect diverse optical data across a range of wavelengths. This review highlights the tunable spectral engineering of 2DM-based IR PDs for this core functionality. We highlight why and how spectrally tunable 2DM-based IR PDs have emerged as transformative intelligent optoelectronic platforms for or alongside AI. Unlike conventional IR PDs, 2DM-based IR PDs enable a paradigm shift through their excellent tunable spectral responsivity and multi-dimensional detection versatility, which is achieved by engineering both geometric and electrical schemes while simultaneously addressing trade-offs among high sensitivity, noise tolerance, broad wavelength range, fast response speed, and low-power operation. We reviewed recent advances in the key operating mechanisms, integration strategies, and application-specific challenges of 2DM-based IR PDs to overcome the limitations and trade-offs of photodetection performance metrics and redefine the architectural foundations for intelligent optoelectronics. While these developments offer significant promise, industrial translation remains limited by interfacial instability, process non-uniformity, and low fabrication yield. In particular, achieving CMOS-compatible processes while preserving spectral tunability and high performance remains a critical challenge. We anticipate that the development of scalable, robust integration techniques (e.g., wafer-scale crack-free transfer processes such as van der Waals pick-and-place methods[520–524] and deposition processes such as low-temperature ALD for industrial implementations[730]) for uniformity and reliability will be key to realizing the full potential of 2DM-based IR PDs. Overall, spectrally tunable 2DM-based IR PDs represent a paradigm shift that extends beyond improving IR detection performance and versatility. Continued research in the tunable spectral engineering of 2DM-based IR PDs will lead to intelligent, multifunctional, adaptive, and scalable optoelectronic systems.

Acknowledgements

J.H., Y.M., Y.N.A., and S.-U.A., contributed equally to this work. This work was supported by the National Research Foundation of Korea (NRF) Grant, funded by the Korean Government's Ministry of Science and ICT (MSIT) with Grant Nos. RS-2024-00355248 (to D.-H.K.), RS-2024-00352458 (to H.-J.S.), RS-2025-23323230 (to H.-J.S.), and RS-2025-00561110 (to H.H.Y.); the Industrial Strategic Technology Development Program, funded by the Korean Government's Ministry of Trade, Industry, and Energy (MOTIE) with Grant No. RS-2024-00431676 (to H.H.Y.); the Regional Innovation Mega Project program, funded by the MSIT with Grant No. 2023-DD-UP-0015 (to D.-H.K.); the State Key Laboratory of Chips and Systems for Advanced Light Field Display, Center for Interdisciplinary Science of Optical Quantum and NEMS Integration, Beijing Institute of Technology (to Y.D.); the National Natural Science Foundation of China with Grant No. 62375020 (to Y.D.); the National Key Research and Development Program of China with Grant Nos. 2022YFA1403302 (to Y.D.) and 2024YFA1410500 (to Y.D.); the Electronics and Telecommunications Research Institute (ETRI) Internal Project, funded by the MSIT with Grant No. 24YR1310 (to H.H.Y. and H.K.); the Korea Basic Science Institute (National Research Facilities and Equipment Center) Grant, funded by the MSIT with Grant No. RS-2025-00516669 (to H.-J.S.); the Future-Leading Specialized Research Project, funded by the Gwangju Institute of Science and Technology (GIST) (to D.-H.K., H.-J.S., and H.H.Y.); the AI-Based GIST Research Scientist Project, funded by the GIST (to H.H.Y.); the InnoCORE Program, funded by the MSIT with Grant No. GIST InnoCORE KH0830 (to Y.M.S. and H.-J.S.); and the Scientific Research Innovation Capability Support Project for Young Faculty, funded by the Ministry of Education of the People's Republic of China with Grant No. ZYGXQNJSKYCXNLZCXM-E8 (W.C.).

Conflict of Interest

The authors declare no conflict of interest.

Keywords

2D materials, infrared photodetectors, intelligent optoelectronics, tunable spectral engineering

Received: July 28, 2025
Revised: October 21, 2025
Published online:

[1] Z. Yang, T. Albrow-Owen, W. Cai, T. Hasan, *Science* **2021**, *371*, eabe0722.
[2] Q. Xue, Y. Yang, W. Ma, H. Zhang, D. Zhang, X. Lan, L. Gao, J. Zhang, J. Tang, *Adv. Sci.* **2024**, *11*, 2404448.
[3] L. Mennel, J. Symonowicz, S. Wachter, D. K. Polyushkin, A. J. Molina-Mendoza, T. Mueller, *Nature* **2020**, *579*, 62.
[4] B. Lu, Y. Xia, Y. Ren, M. Xie, L. Zhou, G. Vinai, S. A. Morton, A. T. Wee, W. G. van der Wiel, W. Zhang, P. K. J. Wong, *Adv. Sci.* **2024**, *11*, 2305277.
[5] M. I. Saleem, A. K. K. Kyaw, J. Hur, *Adv. Opt. Mater.* **2024**, *12*, 2401625.
[6] P. Zhang, Y. Sun, J. Sun, S. Wang, R. Wang, J. Zhang, *Adv. Funct. Mater.* **2025**, *35*, 2502072.
[7] F. Wang, S. Fang, Y. Zhang, Q. J. Wang, *Nat. Commun.* **2025**, *16*, 1.
[8] P. Xie, D. Li, W. Wang, J. C. Ho, *Small* **2025**, e2503717.
[9] G. Cao, P. Meng, J. Chen, H. Liu, R. Bian, C. Zhu, F. Liu, Z. Liu, *Adv. Funct. Mater.* **2021**, *31*, 2005443.
[10] D. Kwak, D. K. Polyushkin, T. Mueller, *Nat. Commun.* **2023**, *14*, 4264.

[11] H. Huang, S. Shi, J. Zha, Y. Xia, H. Wang, P. Yang, L. Zheng, S. Xu, W. Wang, Y. Ren, Y. Wang, Y. Chen, H. P. Chan, J. C. Ho, Y. Chai, Z. Wang, C. Tan, *Nat. Commun.* **2025**, *16*, 3836.
[12] J. I. Kwon, J. S. Kim, H. Seung, J. Kim, H. Cho, T.-M. Choi, J. Park, J. Park, J. A. Lim, M. K. Choi, D.-H. Kim, C. Choi, *Sci. Adv.* **2025**, *11*, eadt6527.
[13] Z. Wang, L. Lu, J. Meng, T. Wang, *Adv. Mater.* **2025**, *37*, 2504710.
[14] J. You, Y. Luo, J. Yang, J. Zhang, K. Yin, K. Wei, X. Zheng, T. Jiang, *Laser Photonics Rev.* **2020**, *14*, 2000239.
[15] V. Pelgrin, H. H. Yoon, E. Cassan, Z. Sun, *Light: Adv. Manuf.* **2023**, *4*, 311.
[16] F. J. García de Abajo, D. N. Basov, F. H. L. Koppens, L. Orsini, M. Ceccanti, S. Castilla, L. Cavicchi, M. Polini, P. A. D. Gonçalves, A. T. Costa, N. M. R. Peres, N. A. Mortensen, S. Bharadwaj, Z. Jacob, P. J. Schuck, A. N. Pasupathy, M. Delor, M. K. Liu, A. Mugarza, P. Merino, M. G. Cuxart, E. Chávez-Angel, M. Svec, L. H. G. Tizei, F. Dirnberger, H. Deng, C. Schneider, V. Menon, T. Deilmann, A. Chernikov, et al., *arXiv* **2025**, https://doi.org/10.1021/acsphotonics.5c00353.
[17] S. Gunapala, B. Levine, D. Ritter, R. Hamm, M. Panish, *Appl. Phys. Lett.* **1991**, *58*, 2024.
[18] J. Faist, F. Capasso, D. L. Sivco, C. Sirtori, A. L. Hutchinson, A. Y. Cho, *Science* **1994**, *264*, 553.
[19] H. Kim, O. Cellek, Z.-Y. Lin, Z.-Y. He, X.-H. Zhao, S. Liu, H. Li, Y.-H. Zhang, *Appl. Phys. Lett.* **2012**, *101*, 16.
[20] W. Lei, J. Antoszewski, L. Faraone, *Appl. Phys. Rev.* **2015**, *2*, 4.
[21] M. Kopytko, A. Rogalski, *Prog. Quantum Electron.* **2016**, *47*, 1.
[22] A. Graf, M. Arndt, M. Sauer, G. Gerlach, *Meas. Sci. Technol.* **2007**, *18*, R59.
[23] A. Rogalski, *OptoElectron. Rev.* **2012**, *20*, 279.
[24] A. Rogalski, in *Electro-Optical and Infrared Systems: Technology and Applications XIV*, vol. *10433*, SPIE, Bellingham, Washington, USA **2017**, pp. 128–152.
[25] M. M. Furchi, A. Pospischil, F. Libisch, J. Burgdorfer, T. Mueller, *Nano Lett.* **2014**, *14*, 4785.
[26] C.-H. Lee, G.-H. Lee, A. M. Van Der Zande, W. Chen, Y. Li, M. Han, X. Cui, G. Arefe, C. Nuckolls, T. F. Heinz, J. Guo, J. Hone, P. Kim, *Nat. Nanotechnol.* **2014**, *9*, 676.
[27] T. Roy, M. Tosun, X. Cao, H. Fang, D.-H. Lien, P. Zhao, Y.-Z. Chen, Y.-L. Chueh, J. Guo, A. Javey, *ACS Nano* **2015**, *9*, 2071.
[28] M. Buscema, J. O. Island, D. J. Groenendijk, S. I. Blanter, G. A. Steele, H. S. van der Zant, A. Castellanos-Gomez, *Chem. Soc. Rev.* **2015**, *44*, 3691.
[29] J. Kistner-Morris, A. Shi, E. Liu, T. Arp, F. Farahmand, T. Taniguchi, K. Watanabe, V. Aji, C. H. Lui, N. Gabor, *Nat. Commun.* **2024**, *15*, 4075.
[30] D. Mastrippolito, M. Cao, E. Bossavit, C. Gureghian, A. Colle, T. Gemo, G. Strobbia, D. De Pesseroey, M. Paye, A. Khalili, H. Zhang, J. Biscaras, J. K. Utterback, P. Dudin, J. Avila, E. Lhuillier, D. Pierucci, *Nano Lett.* **2025**, *25*, 11340.
[31] J. Han, Z. Fu, J. Wei, S. Han, W. Deng, F. Hu, Z. Wang, H. Zhou, H. Yu, J. Gou, J. Wang, *Light: Sci. Appl.* **2025**, *14*, 362.
[32] Z. Sun, H. Chang, *ACS Nano* **2014**, *8*, 4133.
[33] R. Xing, X. Zhang, X. Fan, R. Xie, L. Wu, X. Fang, *Adv. Mater.* **2025**, *37*, 2501833.
[34] R. Dutta, A. Bala, A. Sen, M. R. Spinazze, H. Park, W. Choi, Y. Yoon, S. Kim, *Adv. Mater.* **2023**, *35*, 2303272.
[35] H. Fang, W. Hu, *Adv. Sci.* **2017**, *4*, 1700323.
[36] O. Lopez-Sanchez, D. Lembke, M. Kayci, A. Radenovic, A. Kis, *Nat. Nanotechnol.* **2013**, *8*, 497.
[37] A. Kumar, D. Mandal, *Adv. Energy Mater.* **2024**, *14*, 2403319.
[38] Y. Peng, Q. Yang, J. Fu, J. Yang, Y. Wu, Y. Zhang, G. Li, Z. Li, H. Shi, X. Wei, *Laser Photonics Rev.* **2025**, *19*, 2500218.
[39] F. Wang, T. Zhang, R. Xie, Z. Wang, W. Hu, *Nat. Commun.* **2023**, *14*, 2224.
[40] V. Pecunia, T. D. Anthopoulos, A. Armin, B. Bouthinon, M. Caironi, A. Castellanos-Gomez, Y. Chen, K. Cho, C. Clegg, X. Fang, P. Fendel, B. Fowler, G. Gelinck, H. Gottlob, P. Guyot-Sionnest, R. Hannebauer, G. Hernandez-Sosa, M. C. Hersam, L. Hirsch, L. Hirsch, J. C. Ho, F. H. Isikgor, J. Joimel, H. J. Kim, G. Konstantatos, J. Labram, M. C. Lemme, K. Leo, E. Lhuillier, E. Lidorikis, et al., *Nat. Photonics* **2025**, *19*, 1178.
[41] J. Barnes, D. Allan, *Proc. IEEE* **2005**, *54*, 176.
[42] A. P. Van Der Wel, E. A. Klumperink, J. S. Kolhatkar, E. Hoekstra, M. F. Snoeij, C. Salm, H. Wallinga, B. Nauta, *IEEE J. Solid-State Circuits* **2007**, *42*, 540.
[43] B. E. Saleh, M. C. Teich, *Fundamentals of Photonics, 2 volume set*, John Wiley & sons, New Jersey **2019**.
[44] S. O. Kasap, *Optoelectronics and Photonics*, vol. *218*, Pearson Education UK **2013**.
[45] X. Li, J. Chen, F. Yu, X. Chen, W. Lu, G. Li, *Nano Lett.* **2024**, *24*, 13255.
[46] L. Huang, W. C. Tan, L. Wang, B. Dong, C. Lee, K.-W. Ang, *ACS Appl. Mater. Interfaces* **2017**, *9*, 36130.
[47] S. Kalimuddin, B. Das, S. Chatterjee, A. Bera, S. Bera, K. Chattopadhyay, M. Mondal, *ACS Appl. Mater. Interfaces* **2025**, *17*, 35781.
[48] S. Ryoo, J. Sim, S. Jeong, J. Jang, J. Woo, J. Park, S. Ko, Y. Kim, Y. Song, J. Yoo, H. Ahn, K. Kang, D. Cho, K. Cho, T. Lee, *Adv. Mater. Technol.* **2025**, *10*, 2500064.
[49] Y. Fang, Y. Ge, C. Wang, H. Zhang, *Laser Photonics Rev.* **2020**, *14*, 1900098.
[50] N. Ubrig, E. Ponomarev, J. Zultak, D. Domaretskiy, V. Zólyomi, D. Terry, J. Howarth, I. Gutiérrez-Lezama, A. Zhukov, Z. R. Kudrynskyi, Z. D. Kovalyuk, A. Patanè, T. Taniguchi, K. Watanabe, R. V. Gorbachev, V. I. Fal'ko, A. F. Morpurgo, *Nat. Mater.* **2020**, *19*, 299.
[51] J. Yao, G. Yang, *Nanoscale* **2020**, *12*, 454.
[52] H. Wang, Z. Li, D. Li, P. Chen, L. Pi, X. Zhou, T. Zhai, *Adv. Funct. Mater.* **2021**, *31*, 2103106.
[53] Z. Cheng, T. Zhao, H. Zeng, *Small Sci.* **2022**, *2*, 2100051.
[54] Q. Qiu, Z. Huang, *Adv. Mater.* **2021**, *33*, 2008126.
[55] J. Zha, M. Luo, M. Ye, T. Ahmed, X. Yu, D.-H. Lien, Q. He, D. Lei, J. C. Ho, J. Bullock, K. B. Crozier, C. Tan, *Adv. Funct. Mater.* **2022**, *32*, 2111970.
[56] W. Ahmad, L. Pan, K. Khan, L. Jia, Q. Zhuang, Z. Wang, *Adv. Funct. Mater.* **2023**, *33*, 2300686.
[57] M. Abdullah, M. Younis, M. T. Sohail, S. Wu, X. Zhang, K. Khan, M. Asif, P. Yan, *Small* **2024**, *20*, 2402668.
[58] M. Jiang, D. Kong, M. Zhang, H. Lan, Q. Hu, Y. Zhou, J. Zhou, *Adv. Phys. Res.* **2025**, *4*, 2400199.
[59] N. Argirusis, A. Achilleos, N. Alizadeh, C. Argirusis, G. Sourkouni, *Sensors* **2025**, *25*, 673.
[60] J. Qi, W. Qiao, Z. Y. Wang, *Chem. Rec.* **2016**, *16*, 1531.
[61] S. Keuleyan, E. Lhuillier, V. Brajuskovic, P. Guyot-Sionnest, *Nat. Photonics* **2011**, *5*, 489.
[62] J. Yang, H. Hu, Y. Lv, M. Yuan, B. Wang, Z. He, S. Chen, Y. Wang, Z. Hu, M. Yu, X. Zhang, J. He, J. Zhang, H. Liu, H.-Y. Hsu, J. Tang, H. Song, X. Lan, *Nano Lett.* **2022**, *22*, 3465.
[63] Q. Lin, Z. Wang, M. Young, J. B. Patel, R. L. Milot, L. Martinez Maestro, R. R. Lunt, H. J. Snaith, M. B. Johnston, L. M. Herz, *Adv. Funct. Mater.* **2017**, *27*, 1702485.
[64] L. Mei, R. Huang, C. Shen, J. Hu, P. Wang, Z. Xu, Z. Huang, L. Zhu, *Adv. Opt. Mater.* **2022**, *10*, 2102656.
[65] K. Liao, Y. Lian, M. Yu, Z. Du, T. Dai, Y. Wang, H. Yan, S. Wang, C. Lu, C. Chan, R. Zhu, D. Di, X. Hu, Q. Gong, *Nat. Photonics* **2025**, *19*, 358.
[66] X. Zhang, O. Ericksen, S. Lee, M. Akl, M.-K. Song, H. Lan, P. Pal, J. M. Suh, S. Lindemann, J.-E. Ryu, Y. Shao, X. Zheng, N. M. Han, B. Bhatia, H. Kim, H. S. Kum, C. S. Chang, Y. Shi, C.-B. Eom, J. Kim, *Nature* **2025**, *641*, 98.

[67] A. Rogalski, *Rep. Prog. Phys.* **2005**, *68*, 2267.
[68] E. H. Steenbergen, in *Mid-infrared Optoelectronics*, Elsevier, Amsterdam **2020**, pp. 415–453.
[69] V. Coropceanu, J. Cornil, D. A. da Silva Filho, Y. Olivier, R. Silbey, J.-L. Brédas, *Chem. Rev.* **2007**, *107*, 926.
[70] D. Wang, M. Wright, N. K. Elumalai, A. Uddin, *Sol. Energy Mater. Sol. Cells* **2016**, *147*, 255.
[71] F. Koppens, T. Mueller, P. Avouris, A. Ferrari, M. S. Vitiello, M. Polini, *Nat. Nanotechnol.* **2014**, *9*, 780.
[72] J. Wang, H. Fang, X. Wang, X. Chen, W. Lu, W. Hu, *Small* **2017**, *13*, 1700894.
[73] F. Yan, Z. Wei, X. Wei, Q. Lv, W. Zhu, K. Wang, *Small Methods* **2018**, *2*, 1700349.
[74] G. Konstantatos, *Nat. Commun.* **2018**, *9*, 5266.
[75] N. Huo, G. Konstantatos, *Adv. Mater.* **2018**, *30*, 1801164.
[76] M. Long, P. Wang, H. Fang, W. Hu, *Adv. Funct. Mater.* **2019**, *29*, 1803807.
[77] J. Cheng, C. Wang, X. Zou, L. Liao, *Adv. Opt. Mater.* **2019**, *7*, 1800441.
[78] G. Rao, X. Wang, Y. Wang, P. Wangyang, C. Yan, J. Chu, L. Xue, C. Gong, J. Huang, J. Xiong, Y. Li, *InfoMat* **2019**, *1*, 272.
[79] A. Rogalski, M. Kopytko, P. Martyniuk, *Appl. Phys. Rev.* **2019**, *6*, 2.
[80] E. Wu, D. Wu, C. Jia, Y. Wang, H. Yuan, L. Zeng, T. Xu, Z. Shi, Y. Tian, X. Li, *ACS photonics* **2019**, *6*, 565.
[81] J. Jiang, Y. Wen, H. Wang, L. Yin, R. Cheng, C. Liu, L. Feng, J. He, *Adv. Electron. Mater.* **2021**, *7*, 2001125.
[82] Z. Cheng, R. Cao, K. Wei, Y. Yao, X. Liu, J. Kang, J. Dong, Z. Shi, H. Zhang, X. Zhang, *Adv. Sci.* **2021**, *8*, 2003834.
[83] J. An, X. Zhao, Y. Zhang, M. Liu, J. Yuan, X. Sun, Z. Zhang, B. Wang, S. Li, D. Li, *Adv. Funct. Mater.* **2022**, *32*, 2110119.
[84] F. Wang, T. Zhang, R. Xie, A. Liu, F. Dai, Y. Chen, T. Xu, H. Wang, Z. Wang, L. Liao, J. Wang, P. Zhou, W. Hu, *Adv. Mater.* **2024**, *36*, 2301197.
[85] K. Wang, Q. Wang, E. Tian, C. Liu, Z. Li, K. Liu, *Adv. Funct. Mater.* **2024**, *34*, 2408312.
[86] J. Ahn, E. Yeon, D. K. Hwang, *Adv. Opt. Mater.* **2017**, 2403412.
[87] Y. Wang, E. Liu, A. Gao, T. Cao, M. Long, C. Pan, L. Zhang, J. Zeng, C. Wang, W. Hu, S.-J. Liang, F. Miao, *ACS Nano* **2018**, *12*, 9513.
[88] L. Wang, H. Wang, J. Liu, Y. Wang, H. Shao, W. Li, M. Yi, H. Ling, L. Xie, W. Huang, *Adv. Mater.* **2024**, *36*, 2403538.
[89] J. Han, W. Deng, F. Hu, S. Han, Z. Wang, Z. Fu, H. Zhou, H. Yu, J. Gou, J. Wang, *Adv. Funct. Mater.* **2025**, *35*, 2423360.
[90] Y. Tao, C. Hong, J.-H. Kim, *Sci. Adv.* **2025**, *11*, eady1321.
[91] S. Zhu, H. Liu, J. Wu, J. Mei, R. Zhang, Y. Liu, Y. Chen, X. Cai, *ACS Appl. Mater. Interfaces* **2025**, *17*, 22060.
[92] J. Xu, Z. Wang, K. Yu, G. Zhou, N. Xiao, K. Wang, A. Barinov, M. Marsi, H. Xiang, Z. Zhang, H. Zhang, Z. Chen, *Adv. Funct. Mater.* **2025**, 15145.
[93] V. K. Dat, M. C. Nguyen, B. J. Jeong, N. T. Duong, V. D. Do, C. Hong, D. H. Phuong, V. T. Vu, J. Kang, X. Zhang, R. A. Taylor, K. Kyhm, W. J. Yu, J.-Y. Choi, J.-H. Kim, *Adv. Mater.* **2025**, *37*, 00011.
[94] Y. He, X. Mao, Y. Berencén, J. Gao, Y. Long, Q. Sun, Y. Pan, Q. Deng, S. Ran, D. Luo, X. Liu, T. Zheng, D. Liu, W. Gao, *Adv. Funct. Mater.* **2025**, 17969.
[95] Y. Wang, J. Huang, Z. Pan, C. Luo, Y. Song, Y. Long, T. Zhao, M. Yang, Z. Zheng, N. Huo, Y. Yan, D. Luo, W. Gao, *Adv. Opt. Mater.* **2025**, 02265.
[96] H. Peng, P. Hou, *ACS Appl. Mater. Interfaces* **2025**, *17*, 57708.
[97] C.-h. Liu, J. Zheng, Y. Chen, T. Fryett, A. Majumdar, *Opt. Mater. Express* **2019**, *9*, 384.
[98] H. Lin, Z. Zhang, H. Zhang, K.-T. Lin, X. Wen, Y. Liang, Y. Fu, A. K. T. Lau, T. Ma, C.-W. Qiu, B. Jia, *Chem. Rev.* **2022**, *122*, 15204.
[99] P. G. Zotev, Y. Wang, D. Andres-Penares, T. Severs-Millard, S. Randerson, X. Hu, L. Sortino, C. Louca, M. Brotons-Gisbert, T. Huq, S. Vezzoli, R. Sapienza, T. F. Krauss, B. D. Gerardot, A. I. Tartakovskii, *Laser Photonics Rev.* **2023**, *17*, 2200957.
[100] Y. Meng, H. Zhong, Z. Xu, T. He, J. S. Kim, S. Han, S. Kim, S. Park, Y. Shen, M. Gong, Q. Xiao, S.-H. Bae, *Nanoscale Horiz.* **2023**, *8*, 1345.
[101] Y. Meng, J. Feng, S. Han, Z. Xu, W. Mao, T. Zhang, J. S. Kim, I. Roh, Y. Zhao, D.-H. Kim, Y. Yang, J.-W. Lee, L. Yang, C.-W. Qiu, S.-H. Bae, *Nat. Rev. Mater.* **2023**, *8*, 498.
[102] B. Radisavljevic, A. Radenovic, J. Brivio, V. Giacometti, A. Kis, *Nat. Nanotechnol.* **2011**, *6*, 147.
[103] K. S. Novoselov, A. K. Geim, S. V. Morozov, D.-e. Jiang, Y. Zhang, S. V. Dubonos, I. V. Grigorieva, A. A. Firsov, *Science* **2004**, *306*, 666.
[104] H. Liu, A. T. Neal, Z. Zhu, Z. Luo, X. Xu, D. Tománek, P. D. Ye, *ACS Nano* **2014**, *8*, 4033.
[105] D. A. Bandurin, A. V. Tyurnina, G. L. Yu, A. Mishchenko, V. Zólyomi, S. V. Morozov, R. K. Kumar, R. V. Gorbachev, Z. R. Kudrynskyi, S. Pezzini, Z. D. Kovalyuk, U. Zeitler, K. S. Novoselov, A. Patanè, L. Eaves, I. V. Grigorieva, V. I. Fal'ko, A. K. Geim, Y. Cao, *Nat. Nanotechnol.* **2017**, *12*, 223.
[106] K. S. Novoselov, A. K. Geim, S. V. Morozov, D. Jiang, M. I. Katsnelson, I. V. Grigorieva, S. V. Dubonos, A. A. Firsov, *nature* **2005**, *438*, 197.
[107] R. Roldán, L. Chirolli, E. Prada, J. A. Silva-Guillén, P. San-Jose, F. Guinea, *Chem. Soc. Rev.* **2017**, *46*, 4387.
[108] R. Roldán, J. A. Silva-Guillén, M. P. López-Sancho, F. Guinea, E. Cappelluti, P. Ordejón, *Ann. Phys.* **2014**, *526*, 347.
[109] A. Chaves, J. G. Azadani, H. Alsalman, D. Da Costa, R. Frisenda, A. Chaves, S. H. Song, Y. D. Kim, D. He, J. Zhou, A. Castellanos-Gomez, F. M. Peeters, Z. Liu, C. L. Hinkle, S.-H. Oh, P. D. Ye, S. J. Koester, Y. H. Lee, P. Avouris, X. Wang, T. Low, *npj 2D Mater. Appl.* **2020**, *4*, 29.
[110] T. Low, A. Chaves, J. D. Caldwell, A. Kumar, N. X. Fang, P. Avouris, T. F. Heinz, F. Guinea, L. Martin-Moreno, F. Koppens, *Nat. Mater.* **2017**, *16*, 182.
[111] L. Du, *Nat. Rev. Phys.* **2024**, *6*, 157.
[112] E. C. Regan, D. Wang, E. Y. Paik, Y. Zeng, L. Zhang, J. Zhu, A. H. MacDonald, H. Deng, F. Wang, *Nat. Rev. Mater.* **2022**, *7*, 778.
[113] Y. Jiang, S. Chen, W. Zheng, B. Zheng, A. Pan, *Light: Sci. Appl.* **2021**, *10*, 72.
[114] T. Mueller, E. Malic, *npj 2D Mater. Appl.* **2018**, *2*, 29.
[115] C. Zhang, H. Wang, W. Chan, C. Manolatou, F. Rana, *Phys. Rev. B* **2014**, *89*, 205436.
[116] A. Steinhoff, J.-H. Kim, F. Jahnke, M. Rosner, D.-S. Kim, C. Lee, G. H. Han, M. S. Jeong, T. Wehling, C. Gies, *Nano Lett.* **2015**, *15*, 6841.
[117] C. Attaccalite, M. Grüning, H. Amara, S. Latil, F. Ducastelle, *Phys. Rev. B* **2018**, *98*, 165126.
[118] F. Zhou, J. H. Kua, S. Lu, W. Ji, *Opt. Express* **2018**, *26*, 16093.
[119] X. Liu, T. Galfsky, Z. Sun, F. Xia, E.-c. Lin, Y.-H. Lee, S. Kéna-Cohen, V. M. Menon, *Nat. Photonics* **2015**, *9*, 30.
[120] S. Ghosh, R. Su, J. Zhao, A. Fieramosca, J. Wu, T. Li, Q. Zhang, F. Li, Z. Chen, T. Liew, D. Sanvitto, Q. Xiong, *Photonics Insights* **2022**, *1*, R04.
[121] K. F. Mak, K. He, J. Shan, T. F. Heinz, *Nat. Nanotechnol.* **2012**, *7*, 494.
[122] H. Zeng, J. Dai, W. Yao, D. Xiao, X. Cui, *Nat. Nanotechnol.* **2012**, *7*, 490.
[123] J. Gu, B. Chakraborty, M. Khatoniar, V. M. Menon, *Nat. Nanotechnol.* **2019**, *14*, 1024.
[124] Y. Hu, X. Wen, J. Lin, W. Yao, Y. Chen, J. Li, S. Chen, L. Wang, W. Xu, D. Li, *Nano Lett.* **2023**, *23*, 6581.
[125] Y. Wang, S. Das, F. Iyikanat, Y. Dai, S. Li, X. Guo, X. Yang, J. Cheng, X. Hu, M. Ghotbi, F. Ye, H. Lipsanen, S. Wu, T. Hasan, X. Gan, X. Gan, K. Liu, D. Sun, Q. Dai, F. J. G. d. Abajo, Z. Sun, *ACS Photonics* **2021**, *8*, 2320.
[126] M. Turunen, M. Brotons-Gisbert, Y. Dai, Y. Wang, E. Scerri, C. Bonato, K. D. Jöns, Z. Sun, B. D. Gerardot, *Nat. Rev. Phys.* **2022**, *4*, 219.

[127] H. Hu, N. Chen, H. Teng, R. Yu, M. Xue, K. Chen, Y. Xiao, Y. Qu, D. Hu, J. Chen, Z. Sun, P. Li, F. J. G. d. Abajo, Q. Dai, *Science* **2023**, *379*, 558.
[128] Y. Xiong, Y. Wang, R. Zhu, H. Xu, C. Wu, J. Chen, Y. Ma, Y. Liu, Y. Chen, K. Watanabe, T. Taniguchi, M. Shi, X. Chen, Y. Lu, P. Zhan, Y. Hao, F. Xu, *Sci. Adv.* **2022**, *8*, eabo0375.
[129] F. H. Koppens, D. E. Chang, F. J. García de Abajo, *Nano Lett.* **2011**, *11*, 3370.
[130] A. N. Grigorenko, M. Polini, K. S. Novoselov, *Nat. Photonics* **2012**, *6*, 749.
[131] G. Ni, A. McLeod, Z. Sun, L. Wang, L. Xiong, K. Post, S. Sunku, B.-Y. Jiang, J. Hone, C. R. Dean, M. M. Fogler, D. N. Basov, *Nature* **2018**, *557*, 530.
[132] T. Huang, X. Tu, C. Shen, B. Zheng, J. Wang, H. Wang, K. Khaliji, S. H. Park, Z. Liu, T. Yang, Z. Zhang, L. Shao, X. Li, T. Low, Y. Shi, X. Wang, *Nature* **2022**, *605*, 63.
[133] T. Stauber, H. Kohler, *Nano Lett.* **2016**, *16*, 6844.
[134] G. Wang, L. Li, W. Fan, R. Wang, S. Zhou, J.-T. Lü, L. Gan, T. Zhai, *Adv. Funct. Mater.* **2018**, *28*, 1800339.
[135] H. Zhang, B. Abhiraman, Q. Zhang, J. Miao, K. Jo, S. Roccasecca, M. W. Knight, A. R. Davoyan, D. Jariwala, *Nat. Commun.* **2020**, *11*, 3552.
[136] Y. Wu, J. Duan, W. Ma, Q. Ou, P. Li, P. Alonso-González, J. D. Caldwell, Q. Bao, *Nat. Rev. Phys.* **2022**, *4*, 578.
[137] T. Weber, L. Kühner, L. Sortino, A. Ben Mhenni, N. P. Wilson, J. Kühne, J. J. Finley, S. A. Maier, A. Tittl, *Nat. Mater.* **2023**, *22*, 970.
[138] Y.-T. Chu, P.-L. Chen, S.-H. Huang, S. N. S. Yadav, W.-R. Syong, C.-H. Mao, Y.-J. Lu, C.-H. Liu, P. C. Wu, T.-J. Yen, *ACS Nano* **2025**, *19*, 18545.
[139] D. Rodrigo, O. Limaj, D. Janner, D. Etezadi, F. J. García de Abajo, V. Pruneri, H. Altug, *Science* **2015**, *349*, 165.
[140] D. Wang, A. E. L. Allcca, T.-F. Chung, A. V. Kildishev, Y. P. Chen, A. Boltasseva, V. M. Shalaev, *Light: Sci. Appl.* **2020**, *9*, 126.
[141] K. Yoshioka, G. Bernard, T. Wakamura, M. Hashisaka, K.-i. Sasaki, S. Sasaki, K. Watanabe, T. Taniguchi, N. Kumada, *Nat. Electron.* **2024**, *7*, 537.
[142] Y. Jia, H. Zhao, Q. Guo, X. Wang, H. Wang, F. Xia, *ACS Photonics* **2015**, *2*, 907.
[143] P. Li, M. Lewin, A. V. Kretinin, J. D. Caldwell, K. S. Novoselov, T. Taniguchi, K. Watanabe, F. Gaussmann, T. Taubner, *Nat. Commun.* **2015**, *6*, 7507.
[144] P. Pons-Valencia, F. J. Alfaro-Mozaz, M. M. Wiecha, V. Biolek, I. Dolado, S. Vélez, P. Li, P. Alonso-González, F. Casanova, L. E. Hueso, L. Martín-Moreno, R. Hillenbrand, A. Y. Nikitin, *Nat. Commun.* **2019**, *10*, 3242.
[145] N. Li, X. Guo, X. Yang, R. Qi, T. Qiao, Y. Li, R. Shi, Y. Li, K. Liu, Z. Xu, et al., *Nat. Mater.* **2021**, *20*, 43.
[146] S. G. Menabde, S. Boroviks, J. Ahn, J. T. Heiden, K. Watanabe, T. Taniguchi, T. Low, D. K. Hwang, N. A. Mortensen, M. S. Jang, *Sci. Adv.* **2022**, *8*, eabn0627.
[147] M. Chen, X. Lin, T. H. Dinh, Z. Zheng, J. Shen, Q. Ma, H. Chen, P. Jarillo-Herrero, S. Dai, *Nat. Mater.* **2020**, *19*, 1307.
[148] W. Ma, P. Alonso-González, S. Li, A. Y. Nikitin, J. Yuan, J. Martín-Sánchez, J. Taboada-Gutiérrez, I. Amenabar, P. Li, S. Vélez, C. Tollan, Z. Dai, Y. Zhang, S. Sriram, K. Kalantar-Zadeh, S.-T. Lee, R. Hillenbrand, Q. Bao, *Nature* **2018**, *562*, 557.
[149] G. Ni, A. S. McLeod, Z. Sun, J. R. Matson, C. F. B. Lo, D. A. Rhodes, F. L. Ruta, S. L. Moore, R. A. Vitalone, R. Cusco, L. Artus, L. Xiong, C. R. Dean, J. C. Hone, A. J. Millis, M. M. Fogler, J. H. Edgar, J. D. Caldwell, D. N. Basov, *Nano Lett.* **2021**, *21*, 5767.
[150] H. Wang, M.-L. Chen, M. Zhu, Y. Wang, B. Dong, X. Sun, X. Zhang, S. Cao, X. Li, J. Huang, L. Zhang, W. Liu, D. Sun, Y. Ye, K. Song, J. Wang, Y. Han, H. Guo, C. Qin, L. Xiao, J. Zhang, J. Chen, Z. Han, Z. Zhang, *Nat. Commun.* **2019**, *10*, 2302.
[151] S. Yang, Y. Yang, M. Wu, C. Hu, W. Shen, Y. Gong, L. Huang, C. Jiang, Y. Zhang, P. M. Ajayan, *Adv. Funct. Mater.* **2018**, *28*, 1707379.
[152] W. Chen, A. Chen, R. Zhang, J. Zeng, L. Zhang, M. Gu, C. Wang, M. Huang, Y. Guo, H. Duan, C. Hu, W. Shen, B. Niu, K. Watanabe, T. Taniguchi, J. Zhang, J. Li, X. Cai, G. Liu, *Nano Lett.* **2023**, *23*, 10821.
[153] K. Xin, Z. Zhou, S. Qiu, T. Liu, Y. Yu, J. Yang, W. Hu, Z. Wei, *Nat. Rev. Electrical Eng.* **2025**, *2*, 1.
[154] F. Xia, H. Wang, Y. Jia, *Nat. Commun.* **2014**, *5*, 4458.
[155] H. Yuan, X. Liu, F. Afshinmanesh, W. Li, G. Xu, J. Sun, B. Lian, A. G. Curto, G. Ye, Y. Hikita, Z. Shen, S.-C. Zhang, X. Chen, M. Brongersma, H. Y. Hwang, Y. Cui, *Nat. Nanotechnol.* **2015**, *10*, 707.
[156] C. Wang, G. Zhang, S. Huang, Y. Xie, H. Yan, *Adv. Opt. Mater.* **2020**, *8*, 1900996.
[157] A. Elbanna, H. Jiang, Q. Fu, J.-F. Zhu, Y. Liu, M. Zhao, D. Liu, S. Lai, X. W. Chua, J. Pan, Z. X. Shen, L. Wu, Z. Liu, C.-W. Qiu, J. Teng, *ACS Nano* **2023**, *17*, 4134.
[158] L. Yu, H. Dong, W. Zhang, Z. Zheng, Y. Liang, J. Yao, *Nanoscale Horiz.* **2025**, *10*, 847.
[159] J. Ahn, K. Ko, J.-h. Kyhm, H.-S. Ra, H. Bae, S. Hong, D.-Y. Kim, J. Jang, T. W. Kim, S. Choi, J.-H. Kang, N. Kwon, S. Park, B.-K. Ju, T.-C. Poon, M.-C. Park, S. Im, D. K. Hwang, *ACS Nano* **2021**, *15*, 17917.
[160] L. Li, P. Gong, D. Sheng, S. Wang, W. Wang, X. Zhu, X. Shi, F. Wang, W. Han, S. Yang, K. Liu, H. Li, T. Zhai, *Adv. Mater.* **2018**, *30*, 1804541.
[161] Y. Yang, S.-C. Liu, Y. Wang, M. Long, C.-M. Dai, S. Chen, B. Zhang, Z. Sun, Z. Sun, C. Hu, S. Zhang, L. Tong, G. Zhang, D.-J. Xue, J.-S. Hu, *Adv. Opt. Mater.* **2019**, *7*, 1801311.
[162] Y. Zhang, J. Wu, L. Jia, D. Jin, B. Jia, X. Hu, D. Moss, Q. Gong, *npj Nanophotonics* **2024**, *1*, 28.
[163] P. K. Venuthurumilli, P. D. Ye, X. Xu, *ACS Nano* **2018**, *12*, 4861.
[164] R. Duan, Y. He, C. Zhu, X. Wang, C. Zhu, X. Zhao, Z. Zhang, Q. Zeng, Y. Deng, M. Xu, Z. Liu, *Adv. Funct. Mater.* **2022**, *32*, 2113255.
[165] L. Pi, C. Hu, W. Shen, L. Li, P. Luo, X. Hu, P. Chen, D. Li, Z. Li, X. Zhou, T. Zhai, *Adv. Funct. Mater.* **2021**, *31*, 2006774.
[166] P. Li, J. Zhang, C. Zhu, W. Shen, C. Hu, W. Fu, L. Yan, L. Zhou, L. Zheng, H. Lei, Z. Liu, W. Zhao, P. Gao, P. Yu, G. Yang, *Adv. Mater.* **2021**, *33*, 2102541.
[167] D. Wu, F. Wu, W. Shen, L. Zhou, C. Hu, P. Yu, G. Yang, *Adv. Mater.* **2025**, *37*, 2416041.
[168] W. Luo, Y. Cao, P. Hu, K. Cai, Q. Feng, F. Yan, T. Yan, X. Zhang, K. Wang, *Adv. Opt. Mater.* **2015**, *3*, 1418.
[169] X.-Y. Chen, D. Su, K.-H. Li, Y.-J. Song, P. Xia, X.-Y. Zhang, *Adv. Devices Instrumentation* **2024**, *5*, 0042.
[170] J. Chen, Q. Wang, Y. Sheng, G. Cao, P. Yang, Y. Shan, F. Liao, Z. Muhammad, W. Bao, L. Hu, R. Liu, C. Cong, Z.-J. Qiu, *ACS Appl. Mater. Interfaces* **2019**, *11*, 43330.
[171] H. Huang, J. Wang, W. Hu, L. Liao, P. Wang, X. Wang, F. Gong, Y. Chen, G. Wu, W. Luo, H. Shen, T. Lin, J. Sun, X. Meng, X. Chen, J. Chu, *Nanotechnology* **2016**, *27*, 445201.
[172] J. Wu, G. K. W. Koon, D. Xiang, C. Han, C. T. Toh, E. S. Kulkarni, I. Verzhbitskiy, A. Carvalho, A. S. Rodin, S. P. Koenig, G. Eda, W. Chen, A. H. C. Neto, B. Ozyilmaz, *ACS Nano* **2015**, *9*, 8070.
[173] X. Chen, X. Lu, B. Deng, O. Sinai, Y. Shao, C. Li, S. Yuan, V. Tran, K. Watanabe, T. Taniguchi, D. Naveh, L. Yang, F. Xia, *Nat. Commun.* **2017**, *8*, 1672.
[174] X. Lv, L. Zhang, M. Jiang, S. Zhang, L. Han, K. Zhang, C. Liu, H. Xing, X. Chen, L. Wang, *Adv. Devices Instrumentation* **2023**, *4*, 0012.
[175] M. Long, A. Gao, P. Wang, H. Xia, C. Ott, C. Pan, Y. Fu, E. Liu, X. Chen, W. Lu, T. Nilges, J. Xu, X. Wang, W. Hu, *Sci. Adv.* **2017**, *3*, 1700589.
[176] J. Li, L. Jiang, W. Ma, T. Wu, Q. Qiu, Y. Shi, W. Zhou, N. Yao, Z. Huang, *ACS Appl. Nano Mater.* **2022**, *5*, 5158.
[177] B. Y. Zhang, T. Liu, B. Meng, X. Li, G. Liang, X. Hu, Q. J. Wang, *Nat. Commun.* **2013**, *4*, 1811.

[178] T. Mueller, F. Xia, P. Avouris, *Nat. Photonics* **2010**, *4*, 297.
[179] H. Zhang, L. Du, X. Zhong, W. Wu, Z. Fu, W. Sun, J. Liu, X. Song, J. Zhang, Z. Dai, Y. Ren, Y. Ye, X. Ren, J. Yao, *Sens. Actuators, A* **2024**, *371*, 115324.
[180] H. Xu, C. Guo, J. Zhang, W. Guo, C.-N. Kuo, C. S. Lue, W. Hu, L. Wang, G. Chen, A. Politano, X. Chen, W. Lu, *Small* **2019**, *15*, 1903362.
[181] J. Lai, X. Liu, J. Ma, Q. Wang, K. Zhang, X. Ren, Y. Liu, Q. Gu, X. Zhuo, W. Lu, Y. Wu, Y. Li, J. Feng, S. Zhou, J.-H. Chen, D. Sun, *Adv. Mater.* **2018**, *30*, 1707152.
[182] J. Lai, Y. Liu, J. Ma, X. Zhuo, Y. Peng, W. Lu, Z. Liu, J. Chen, D. Sun, *ACS Nano* **2018**, *12*, 4055.
[183] A. Sharma, A. Srivastava, T. Senguttuvan, S. Husale, *Sci. Rep.* **2017**, *7*, 17911.
[184] W. Ma, T. Wu, N. Yao, W. Zhou, L. Jiang, Q. Qiu, J. Li, Z. Huang, *Commun. Mater.* **2022**, *3*, 68.
[185] M. Jiang, H. Xing, L. Zhang, L. Han, K. Zhang, C. Yao, D. Wang, X. Wang, S. Lan, X. Lv, L. Wang, *Adv. Opt. Mater.* **2023**, *11*, 2300074.
[186] P. Metuh, A. Paralikis, P. Wyborski, S. Jamo, A. Palermo, L. Zugliani, M. Barbone, K. Müller, N. Gregersen, S. Vaitiekėnas, J. Finley, B. Munkhbat, *arXiv preprint* **2025**, arXiv:2503.22670.
[187] S. Bharucha, M. Dave, R. Vaidya, *Mater. Today:. Proc.* **2022**, *55*, 118.
[188] H. Yu, H. Zeng, Y. Zhang, Y. Liu, W. ShangGuan, X. Zhang, Z. Zhang, Y. Zhang, *Adv. Funct. Mater.* **2025**, *35*, 2412913.
[189] Y. Dong, Z. Sun, I. Phinney, D. Sun, T. Andersen, L. Xiong, Y. Shao, S. Zhang, A. Rikhter, S. Liu, P. Jarillo-Herrero, P. Kim, C. R. Dean, A. J. Millis, M. M. Fogler, D. A. Bandurin, D. N. Basov, *Nat. Commun.* **2025**, *16*, 3861.
[190] F. Xia, T. Mueller, Y.-m. Lin, A. Valdes-Garcia, P. Avouris, *Nat. Nanotechnol.* **2009**, *4*, 839.
[191] M. Freitag, T. Low, W. Zhu, H. Yan, F. Xia, P. Avouris, *Nat. Commun.* **2013**, *4*, 1951.
[192] M. Freitag, T. Low, F. Xia, P. Avouris, *Nat. Photonics* **2013**, *7*, 53.
[193] C.-H. Liu, Y.-C. Chang, T. B. Norris, Z. Zhong, *Nat. Nanotechnol.* **2014**, *9*, 273.
[194] F. Wang, Y. Zhang, C. Tian, C. Girit, A. Zettl, M. Crommie, Y. R. Shen, *science* **2008**, *320*, 206.
[195] Z. Li, E. A. Henriksen, Z. Jiang, Z. Hao, M. C. Martin, P. Kim, H. L. Stormer, D. N. Basov, *Nat. Phys.* **2008**, *4*, 532.
[196] J. Horng, C.-F. Chen, B. Geng, C. Girit, Y. Zhang, Z. Hao, H. A. Bechtel, M. Martin, A. Zettl, M. F. Crommie, Y. R. Shen, F. Wang, *Phys. Rev. B* **2011**, *83*, 165113.
[197] L. Ren, Q. Zhang, J. Yao, Z. Sun, R. Kaneko, Z. Yan, S. Nanot, Z. Jin, I. Kawayama, M. Tonouchi, J. M. Tour, J. Kono, *Nano Lett.* **2012**, *12*, 3711.
[198] A. Schmitt, P. Vallet, D. Mele, M. Rosticher, T. Taniguchi, K. Watanabe, E. Bocquillon, G. Feve, J.-M. Berroir, C. Voisin, J. Cayssol, M. O. Goerbig, J. Troost, E. Baudin, B. Placais, *Nat. Phys.* **2023**, *19*, 830.
[199] D. Allor, T. D. Cohen, D. A. McGady, *Phys. Rev. D: Part., Fields, Gravitation, Cosmol.* **2008**, *78*, 096009.
[200] S. Kubakaddi, K. Bhargavi, *Phys. Rev. B* **2010**, *82*, 155410.
[201] S. Koniakhin, E. Eidelman, *Europhys. Lett.* **2013**, *103*, 37006.
[202] T. I. Andersen, B. L. Dwyer, J. D. Sanchez-Yamagishi, J. F. Rodriguez-Nieva, K. Agarwal, K. Watanabe, T. Taniguchi, E. A. Demler, P. Kim, H. Park, M. D. Lukin, *Science* **2019**, *364*, 154.
[203] A. H. Barajas-Aguilar, J. Zion, I. Sequeira, A. Z. Barabas, T. Taniguchi, K. Watanabe, E. B. Barrett, T. Scaffidi, J. D. Sanchez-Yamagishi, *Nat. Commun.* **2024**, *15*, 2550.
[204] W. Zhao, S. Zhao, H. Li, S. Wang, S. Wang, M. I. B. Utama, S. Kahn, Y. Jiang, X. Xiao, S. Yoo, K. Watanabe, T. Taniguchi, A. Zettl, F. Wang, *Nature* **2021**, *594*, 517.
[205] Y. Dong, L. Xiong, I. Phinney, Z. Sun, R. Jing, A. McLeod, S. Zhang, S. Liu, F. Ruta, H. Gao, Z. Deong, R. Pan, J. H. Edgar, P. Jarillo-Herrero, L. S. Levitov, A. J. Millis, M. M. Fogler, D. A. Bandurin, D. N. Basov, *Nature* **2021**, *594*, 513.
[206] I. Kaminer, Y. T. Katan, H. Buljan, Y. Shen, O. Ilic, J. J. López, L. J. Wong, J. D. Joannopoulos, M. Soljačić, *Nat. Commun.* **2016**, *7*, ncomms11880.
[207] R. Beams, P. Bharadwaj, L. Novotny, *Nanotechnology* **2014**, *25*, 055206.
[208] Y. D. Kim, H. Kim, Y. Cho, J. H. Ryoo, C.-H. Park, P. Kim, Y. S. Kim, S. Lee, Y. Li, S.-N. Park, Y. S. Yoo, D. Yoon, V. E. Dorgan, E. Pop, T. F. Heinz, J. Hone, S.-H. Chun, H. Cheong, S. W. Lee, M.-H. Bae, Y. D. Park, *Nat. Nanotechnol.* **2015**, *10*, 676.
[209] L. J. Wong, I. Kaminer, O. Ilic, J. D. Joannopoulos, M. Soljačić, *Nat. Photonics* **2016**, *10*, 46.
[210] X. Zhou, X. Hu, J. Yu, S. Liu, Z. Shu, Q. Zhang, H. Li, Y. Ma, H. Xu, T. Zhai, *Adv. Funct. Mater.* **2018**, *28*, 1706587.
[211] X. Zhou, X. Hu, S. Zhou, H. Song, Q. Zhang, L. Pi, L. Li, H. Li, J. Lü, T. Zhai, *Adv. Mater.* **2018**, *30*, 1703286.
[212] Y. Liu, Y. Huang, X. Duan, *Nature* **2019**, *567*, 323.
[213] S. Lukman, L. Ding, L. Xu, Y. Tao, A. C. Riis-Jensen, G. Zhang, Q. Y. S. Wu, M. Yang, S. Luo, C. Hsu, L. Yao, G. Liang, H. Lin, Y.-W. Zhang, K. S. Thygesen, Q. J. Wang, Y. Feng, J. Teng, *Nat. Nanotechnol.* **2020**, *15*, 675.
[214] H. Kang, J. Ma, J. Li, X. Zhang, X. Liu, *ACS Nano* **2023**, *17*, 24449.
[215] J. Liu, H. Gan, Q. Hao, Y. Zeng, Y. Gong, J. Zhu, J. Huang, F. Liu, W. Zhang, *InfoMat* **2025**, *7*, e12625.
[216] A. Urich, K. Unterrainer, T. Mueller, *Nano Lett.* **2011**, *11*, 2804.
[217] F. De Juan, A. G. Grushin, T. Morimoto, J. E. Moore, *Nat. Commun.* **2017**, *8*, 15995.
[218] X. Sun, G. Adamo, M. Eginligil, H. N. Krishnamoorthy, N. I. Zheludev, C. Soci, *Sci. Adv.* **2021**, *7*, eabe5748.
[219] I. E. Zadeh, J. Chang, J. W. Los, S. Gyger, A. W. Elshaari, S. Steinhauer, S. N. Dorenbos, V. Zwiller, *Appl. Phys. Lett.* **2021**, *118*, 19.
[220] G. Di Battista, K. C. Fong, A. Díez-Carlón, K. Watanabe, T. Taniguchi, D. K. Efetov, *Sci. Adv.* **2024**, *10*, eadp3725.
[221] Q. Yang, W. Shi, Z. Zhong, X. Li, Y. Li, X. Meng, J. Wang, J. Chu, H. Huang, *Nano Lett.* **2024**, *24*, 16417.
[222] T.-R. T. Han, F. Zhou, C. D. Malliakas, P. M. Duxbury, S. D. Mahanti, M. G. Kanatzidis, C.-Y. Ruan, *Sci. Adv.* **2015**, *1*, e1400173.
[223] J. Kim, K. Heo, D.-H. Kang, C. Shin, S. Lee, H.-Y. Yu, J.-H. Park, *Adv. Sci.* **2019**, *6*, 1901255.
[224] D. Wu, J. Guo, J. Du, C. Xia, L. Zeng, Y. Tian, Z. Shi, Y. Tian, X. J. Li, Y. H. Tsang, J. Jie, *ACS Nano* **2019**, *13*, 9907.
[225] G. Zhang, M. Amani, A. Chaturvedi, C. Tan, J. Bullock, X. Song, H. Kim, D.-H. Lien, M. C. Scott, H. Zhang, A. Javey, *Appl. Phys. Lett.* **2019**, *114*, 25.
[226] L. Wang, L. Han, W. Guo, L. Zhang, C. Yao, Z. Chen, Y. Chen, C. Guo, K. Zhang, C.-N. Kuo, C. S. Lue, A. Politano, H. Xing, M. Jiang, X. Yu, X. Chen, W. Lu, *Light: Sci. Appl.* **2022**, *11*, 53.
[227] W. Fan, H. Yan, X. Wang, L. Tong, W. Yan, C. Su, Q. Wang, S. Yin, *Adv. Funct. Mater.* **2025**, 2416703.
[228] M. R. Miah, M. I. R. Ebon, A. T. Abir, J. Hossain, *Adv. Theory Simul.* **2024**, *7*, 2400389.
[229] H. Jang, Y. Seok, Y. Choi, S.-H. Cho, K. Watanabe, T. Taniguchi, K. Lee, *Adv. Funct. Mater.* **2021**, *31*, 2006788.
[230] L. Li, Q. Wu, C. Wang, Z. Cai, L. Lin, X. Gu, K. K. Ostrikov, H. Nan, S. Xiao, *ACS Photonics* **2024**, *11*, 2615.
[231] L. Tong, X. Huang, P. Wang, L. Ye, M. Peng, L. An, Q. Sun, Y. Zhang, G. Yang, Z. Li, F. Zhong, F. Wang, Y. Wang, M. Motlag, W. Wu, G. J. Cheng, W. Hu, *Nat. Commun.* **2020**, *11*, 2308.
[232] J. Xiong, Q. Yu, X. Hou, B. Liu, S. Li, H. Deng, Z. Yang, J. Leng, S. Zhu, Y. Sun, Z. Jiang, N. Huo, J. Wu, P. Zhou, *Adv. Funct. Mater.* **2024**, *34*, 2314972.

[233] P. Wang, Z. Li, X. Xia, J. Zhang, Y. Lan, L. Zhu, Q. Ke, H. Mu, S. Lin, *Small* **2024**, *20*, 2401216.
[234] Y. Yu, T. Zhao, M. Peng, T. Xu, S. Duan, Y. She, P. Jian, M. Chen, Y. Chen, Z. Wang, F. Wu, P. Martyniuk, Y. H. Tsang, B. Yao, L. Zeng, J. Dai, C. Chen, W. Hu, *Small* **2025**, *21*, 2407830.
[235] J. Liao, H. Shao, Y. Zhang, Y. Yan, J. Zeng, C. Lan, B. Gao, D. Chen, Q. Quan, P. Xie, Y. Meng, J. C. Ho, *Adv. Mater.* **2025**, *37*, 2419653.
[236] T. U. Tran, N. T. Duong, D. Y. Park, H. P. Duong, J. Bahng, V. D. Do, M. S. Jeong, S. C. Lim, *Nanoscale Horiz.* **2025**, *10*, 1215.
[237] M. Buscema, D. J. Groenendijk, S. I. Blanter, G. A. Steele, H. S. Van Der Zant, A. Castellanos-Gomez, *Nano Lett.* **2014**, *14*, 3347.
[238] X. Zhu, Z. Cai, Q. Wu, J. Wu, S. Liu, X. Chen, Q. Zhao, *Laser Photonics Rev.* **2025**, *19*, 2400703.
[239] L. Ai, J. Zhang, C. Chen, Q. Zhang, X. Wang, X. Wang, L. Huang, M. Xia, A. Pan, L. Wang, K. Zhang, J. Wang, *ACS Appl. Electron. Mater.* **2024**, *6*, 3820.
[240] N. Higashitarumizu, S. Wang, S. Wang, H. Kim, J. Bullock, A. Javey, *Nano Lett.* **2024**, *24*, 13107.
[241] J. I. Kim, N. Higashitarumizu, S. Wang, R. Yalisove, M. C. Scott, S. Y. Song, A. Javey, *Adv. Mater.* **2024**, *36*, 2402922.
[242] M. Amani, E. Regan, J. Bullock, G. H. Ahn, A. Javey, *ACS Nano* **2017**, *11*, 11724.
[243] S. Zhang, X. Huang, Y. Chen, R. Yin, H. Wang, T. Xu, J. Guo, X. Wang, T. Lin, H. Shen, J. Ge, X. Meng, W. Hu, N. Dai, X. Wang, J. Chu, J. Wang, *Adv. Mater.* **2024**, *36*, 2313134.
[244] Q. Bai, X. Huang, S. Du, Y. Guo, C. Li, W. Li, J. Li, C. Gu, *Nanoscale* **2024**, *16*, 8907.
[245] A. A. Soluyanov, D. Gresch, Z. Wang, Q. Wu, M. Troyer, X. Dai, B. A. Bernevig, *Nature* **2015**, *527*, 495.
[246] A. Burkov, *Nat. Mater.* **2016**, *15*, 1145.
[247] W. Li, X. Gong, Z. Yu, L. Ma, W. Sun, S. Gao, Ç. Köroğlu, W. Wang, L. Liu, T. Li, H. Ning, D. Fan, Y. Xu, X. Tu, T. Xu, L. Sun, W. Wang, J. Lu, Z. Ni, J. Li, X. Duan, P. Wang, Y. Nie, H. Qiu, Y. Shi, E. Pop, J. Wang, X. Wang, *Nature* **2023**, *613*, 274.
[248] E. Zhai, T. Liang, R. Liu, M. Cai, R. Li, Q. Shao, C. Su, Y. C. Lin, *Nat. Rev. Electrical Eng.* **2024**, *1*, 497.
[249] S. Ghods, H. Lee, J.-H. Choi, J.-Y. Moon, S. Kim, S.-I. Kim, H. J. Kwun, M. J. Josline, C. Y. Kim, S. H. Hyun, et al., *ACS Nano* **2024**, *18*, 26192.
[250] X. Li, K. Liu, D. Wu, P. Lin, Z. Shi, X. Li, L. Zeng, Y. Chai, S. P. Lau, Y. H. Tsang, *Adv. Mater.* **2025**, 2415717.
[251] S. Qiao, J. Liu, C. Yao, N. Yang, F. Zheng, W. Meng, Y. Wan, P. C. Chow, D.-K. Ki, L. Zhang, Y. Shi, L.-J. Li, *Light: Sci. Appl.* **2025**, *14*, 22.
[252] P. Niu, H. Liu, P. Zhang, J. Lai, *Adv. Opt. Mater.* **2025**, *13*, 02083.
[253] J. Wei, Y. Li, L. Wang, W. Liao, B. Dong, C. Xu, C. Zhu, K.-W. Ang, C.-W. Qiu, C. Lee, *Nat. Commun.* **2020**, *11*, 6404.
[254] H. H. Yoon, F. Ahmed, Y. Dai, H. A. Fernandez, X. Cui, X. Bai, D. Li, M. Du, H. Lipsanen, Z. Sun, *ACS Appl. Mater. Interfaces* **2021**, *13*, 58927.
[255] E. I. Titova, M. A. Kashchenko, A. V. Miakonkikh, A. D. Morozov, A. V. Shabanov, I. K. Domaratskiy, S. S. Zhukov, D. A. Mylnikov, V. V. Rumyantsev, S. V. Morozov, K. S. Novoselov, D. A. Bandurin, D. A. Svintsov, *Adv. Opt. Mater.* **2025**, 2500167.
[256] S. L. Patil, O. Y. Pawar, T. D. Dongale, S. Chang, S. Lim, Y. M. Song, *Carbon* **2024**, *228*, 119320.
[257] W. Yao, E. Wang, H. Huang, K. Deng, M. Yan, K. Zhang, K. Miyamoto, T. Okuda, L. Li, Y. Wang, H. Gao, C. Liu, W. Duan, S. Zhou, *Nat. Commun.* **2017**, *8*, 14216.
[258] T. Wei, X. Wang, Q. Yang, Z. He, P. Yu, Z. Xie, H. Chen, S. Li, S. Wu, *ACS Appl. Mater. Interfaces* **2021**, *13*, 22757.
[259] Z. Dong, W. Yu, L. Zhang, L. Yang, L. Huang, Y. Zhang, Z. Ren, H. Mu, C. Chen, J. Zhang, J. Li, L. Wang, K. Zhang, *InfoMat* **2023**, *5*, e12403.
[260] M. Choi, S. Oh, S. Hahn, Y. Ji, M.-k. Jo, J. Kim, T.-S. Ju, G. Kim, M. Gyeon, Y. Lee, J. Do, S. Choi, A. Kim, S. Yang, C. Hwang, K.-J. Kim, D. Cho, C. Kim, K. Kang, H. Y. Jeong, S. Song, *ACS Nano* **2024**, *18*, 15154.
[261] H.-J. Noh, J. Jeong, E.-J. Cho, K. Kim, B. Min, B.-G. Park, *Phys. Rev. Lett.* **2017**, *119*, 016401.
[262] C. Zhang, S. Peng, J. Han, C. Li, H. Zhou, H. Yu, J. Gou, C. Chen, Y. Jiang, J. Wang, *Adv. Funct. Mater.* **2023**, *33*, 2302466.
[263] L. Zeng, W. Han, X. Ren, X. Li, D. Wu, S. Liu, H. Wang, S. P. Lau, Y. H. Tsang, C.-X. Shan, J. Jie, *Nano Lett.* **2023**, *23*, 8241.
[264] Z. Wang, H. Weng, Q. Wu, X. Dai, Z. Fang, *Phys. Rev. B* **2013**, *88*, 125427.
[265] S. Borisenko, Q. Gibson, D. Evtushinsky, V. Zabolotnyy, B. Büchner, R. J. Cava, *Phys. Rev. Lett.* **2014**, *113*, 027603.
[266] M. Neupane, S.-Y. Xu, R. Sankar, N. Alidoust, G. Bian, C. Liu, I. Belopolski, T.-R. Chang, H.-T. Jeng, H. Lin, A. Bansil, F. Chou, M. Z. Hasan, *Nat. Commun.* **2014**, *5*, 3786.
[267] J. Ma, B. Cheng, L. Li, Z. Fan, H. Mu, J. Lai, X. Song, D. Yang, J. Cheng, Z. Wang, C. Zeng, D. Sun, *Nat. Commun.* **2022**, *13*, 5425.
[268] Z. Zhao, F. Dong, Y. Wang, J. Sun, H. Ye, R. Wang, J. Zhang, *Nanoscale* **2023**, *15*, 11955.
[269] Y.-Q. Bie, G. Grosso, M. Heuck, M. M. Furchi, Y. Cao, J. Zheng, D. Bunandar, E. Navarro-Moratalla, L. Zhou, D. K. Efetov, T. Taniguchi, K. Watanabe, J. Kong, D. Englund, P. Jarillo-Herrero, *Nat. Nanotechnol.* **2017**, *12*, 1124.
[270] H. Wang, Y. Li, P. Gao, J. Wang, X. Meng, Y. Hu, J. Yang, Z. Huang, W. Gao, Z. Zheng, Z. Wei, J. Li, N. Huo, *Adv. Mater.* **2024**, *36*, 2309371.
[271] J. Ma, Q. Gu, Y. Liu, J. Lai, P. Yu, X. Zhuo, Z. Liu, J.-H. Chen, J. Feng, D. Sun, *Nat. Mater.* **2019**, *18*, 476.
[272] B. Feng, B. Fu, S. Kasamatsu, S. Ito, P. Cheng, C.-C. Liu, Y. Feng, S. Wu, S. K. Mahatha, P. Sheverdyaeva, P. Moras, M. Arita, O. Sugino, T.-C. Chiang, K. Shimada, K. Miyamoto, T. Okuda, K. Wu, L. Chen, Y. Yao, I. Matsuda, *Nat. Commun.* **2017**, *8*, 1007.
[273] B. Das, N. S. Das, S. Sarkar, B. K. Chatterjee, K. K. Chattopadhyay, *ACS Appl. Mater. Interfaces* **2017**, *9*, 22788.
[274] F. Wang, L. Li, W. Huang, L. Li, B. Jin, H. Li, T. Zhai, *Adv. Funct. Mater.* **2018**, *28*, 1802707.
[275] X. Zhang, X. Liu, C. Zhang, S. Peng, H. Zhou, L. He, J. Gou, X. Wang, J. Wang, *ACS Nano* **2022**, *16*, 4851.
[276] H. Lu, S. Shi, D. Li, S. Bo, J. Zheng, D. Mao, Y. Zhang, X. Gan, J. Zhao, *Laser Photonics Rev.* **2025**, *19*, 2500033.
[277] K. Zheng, L.-B. Luo, T.-F. Zhang, Y.-H. Liu, Y.-Q. Yu, R. Lu, H.-L. Qiu, Z.-J. Li, J. A. Huang, *J. Mater. Chem. C* **2015**, *3*, 9154.
[278] H. Lu, S. Shi, D. Li, L. Hou, S. Bo, J. Zhao, F. Xiao, D. Mao, J. Zhao, *Laser Photonics Rev.* **2023**, *17*, 2300269.
[279] S. Zhang, H. Luo, H. Wang, J. Liu, A. Suvorova, Y. Ren, C. Yuan, W. Lei, *Opt. Mater.* **2024**, *150*, 115220.
[280] Y. Zhang, H. Lu, Z. Yue, M. Zhang, X. Gan, J. Zhao, *Adv. Photonics Res.* **2025**, *6*, 2400232.
[281] M. Suleman, M. Kim, A. Rehmat, E. Elahi, M. Asim, M. Riaz, S. Kumar, J. Jung, Y. Seo, *Adv. Opt. Mater.* **2025**, *13*, 01177.
[282] S. Lan, L. Han, C. Yao, S. Tian, L. Zhang, M. Jiang, X. Pan, Y. Wei, Y. Zhang, K. Zhang, H. Xing, X. Chen, L. Wang, *Laser Photonics Rev.* **2025**, *19*, 2402091.
[283] M. Yang, H. Zhou, J. Wang, *Mater. Today Commun.* **2022**, *33*, 104190.
[284] D. Qiu, C. Gong, S. Wang, M. Zhang, C. Yang, X. Wang, J. Xiong, *Adv. Mater.* **2021**, *33*, 2006124.
[285] B. Chen, H. Xue, H. Pan, L. Zhu, X. Yan, J. Wang, Y. Song, Z. An, *Light: Sci. Appl.* **2024**, *13*, 97.
[286] Q.-Y. Wang, Z. Li, W.-H. Zhang, Z.-C. Zhang, J.-S. Zhang, W. Li, H. Ding, Y.-B. Ou, P. Deng, K. Chang, J. Wen, C.-L. Song, K. He, J.-F. Jia,

S.-H. Ji, Y.-Y. Wang, L.-L. Wang, X. Chen, X.-C. Ma, Q.-K. Xue, *Chin. Phys. Lett.* **2012**, *29*, 037402.
[287] J.-F. Ge, Z.-L. Liu, C. Liu, C.-L. Gao, D. Qian, Q.-K. Xue, Y. Liu, J.-F. Jia, *Nat. Mater.* **2015**, *14*, 285.
[288] M. Kumar, S. Lim, J. Kim, H. Seo, *Adv. Mater.* **2023**, *35*, 2210907.
[289] A. Milloch, M. Fabrizio, C. Giannetti, *npj Spintronics* **2024**, *2*, 49.
[290] X. Sun, K. Xiao, Y. Wei, W. Mo, L. Zhang, S. Tian, X. Pan, Y. Yang, S. Lan, Y. Zhang, Z. Hu, K. Zhang, L. Han, F. Wang, X. Chen, L. Wang, W. Hu, *Nat. Commun.* **2025**, *16*, 1.
[291] M. Islam, S. M. Bohaichuk, T. D. Brown, S. Oh, C. Perez, C. Zhang, T. J. Park, M. Park, A. A. Talin, S. Ramanathan, S. Kumar, E. Pop, *Nat. Electron.* **2025**, *8*, 672.
[292] H. Itoh, A. Takahashi, M. Aihara, *Phys. Rev. B* **2006**, *73*, 075110.
[293] D. Wu, Y. Ma, Y. Niu, Q. Liu, T. Dong, S. Zhang, J. Niu, H. Zhou, J. Wei, Y. Wang, Z. Zhao, N. Wang, *Sci. Adv.* **2018**, *4*, eaao3057.
[294] Y. Wang, W. Yao, Z. Xin, T. Han, Z. Wang, L. Chen, C. Cai, Y. Li, Y. Zhang, *Nat. Commun.* **2020**, *11*, 4215.
[295] W. Wu, Y. Wang, Y. Niu, P. Wang, M. Chen, J. Sun, N. Wang, D. Wu, Z. Zhao, *ACS Appl. Mater. Interfaces* **2020**, *12*, 14165.
[296] K. Xiao, S. Zhang, K. Zhang, L. Zhang, Y. Wen, S. Tian, Y. Xiao, C. Shi, S. Hou, C. Liu, L. Han, J. He, W. Tang, G. Li, L. Wang, X. Chen, *Adv. Sci.* **2024**, *11*, 2401716.
[297] D. Jariwala, T. J. Marks, M. C. Hersam, *Nat. Mater.* **2017**, *16*, 170.
[298] J. Jang, Y. Lee, J.-Y. Yoon, H. H. Yoon, J. Koo, J. Choe, S. Jeon, J. Sung, J. Park, W. C. Lee, H. Lee, H. Y. Jeong, K. Park, K. Kim, *Nano Lett.* **2018**, *18*, 6214.
[299] Z. Zhang, P. Lin, Q. Liao, Z. Kang, H. Si, Y. Zhang, *Adv. Mater.* **2019**, *31*, 1806411.
[300] A. M. Shafi, F. Ahmed, H. A. Fernandez, M. G. Uddin, X. Cui, S. Das, Y. Dai, V. Khayrudinov, H. H. Yoon, L. Du, Z. Sun, H. Lipsanen, *ACS Appl. Mater. Interfaces* **2022**, *14*, 31140.
[301] X. Bai, Z. Xu, Q. Zhang, S. Li, Y. Dai, X. Cui, H. H. Yoon, L. Yao, H. Jiang, M. Du, Y. Zhang, E. I. Kauppinen, Z. Sun, *Adv. Mater. Interfaces* **2022**, *9*, 2200193.
[302] E.-X. Ding, P. Liu, H. H. Yoon, F. Ahmed, M. Du, A. M. Shafi, N. Mehmood, E. I. Kauppinen, Z. Sun, H. Lipsanen, *ACS Appl. Mater. Interfaces* **2023**, *15*, 4216.
[303] Z. Xu, Q. Qin, X. Ma, J. Chen, X. Liu, W. Chen, Z. Qiu, L. Wu, W. Gao, L. Li, *Adv. Opt. Mater.* **2024**, *12*, 2401379.
[304] J. Zhou, W. Chen, L. Lu, B. Zhu, G. Ren, Y. Pan, J. Ou, L. Zhu, *Adv. Opt. Mater.* **2025**, *13*, 2403253.
[305] J. Xie, J. Han, J. Jiang, L. Liu, Z. Fu, J. Wang, *Adv. Opt. Mater.* **2025**, *13*, 2403463.
[306] X. Guan, Y. Chen, Y. Ma, H. Liang, Z. Zheng, C. Ma, C. Du, J. Yao, G. Yang, *Nanoscale* **2024**, *16*, 20811.
[307] W. Liu, Y. Wu, X. Bao, L. Sun, Y. Xie, Y. Chen, *Adv. Funct. Mater.* **2025**, *35*, 2421525.
[308] J. Jang, J. P. Hong, S.-J. Kim, J. Ahn, B.-S. Yu, J. Han, K. Lee, A. Ha, E. Yoon, W. Kim, S. Jo, H. W. Ko, S. K. Yoon, T. Taniguchi, K. Watanabe, H. Baek, D.-Y. Kim, K. Lee, S. Mun, K. H. Lee, S. Park, K. Kim, Y. J. Song, S. A. Lee, H. J. Kim, J. W. Shim, G. Wang, J.-H. Kang, M.-C. Park, D. K. Hwang, *Nat. Electron.* **2025**, 1.
[309] Y. Luo, H. Yu, X. Wei, J. Wen, H. Zeng, Y. Zheng, Z. Zhang, X. Zhang, Y. Zhang, *Adv. Funct. Mater.* **2025**, 10929.
[310] C. Liu, T. Liang, X. Sui, L. Du, Q. Guo, G. Xue, C. Huang, Y. You, G. Yao, M. Zhao, J. Yin, Z. Sun, H. Hong, E. Wang, K. Liu, *Nat. Commun.* **2025**, *16*, 544.
[311] F. Zhou, S. Yu, M. Wu, X. Zhong, X. Song, H. Zhang, *Sens. Actuators Rep.* **2025**, *10*, 100350.
[312] L. Howe, K. H. Ellepola, N. Jahan, B. Talbert, J. Li, M. P. Cooney, N. Q. Vinh, *ACS Appl. Electron. Mater.* **2025**, *7*, 1305.
[313] B. Sheng, J. Yang, C. Zhang, M. Jiang, W. Ma, X. Liu, K. Kalantar-Zadeh, Z. Chen, X. Li, *Adv. Electron. Mater.* **2024**, *10*, 2400190.
[314] M. Liu, J. Wei, L. Qi, J. An, X. Liu, Y. Li, Z. Shi, D. Li, K. S. Novoselov, C.-W. Qiu, S. Li, *Nat. Commun.* **2024**, *15*, 141.
[315] N. M. Gabor, J. C. Song, Q. Ma, N. L. Nair, T. Taychatanapat, K. Watanabe, T. Taniguchi, L. S. Levitov, P. Jarillo-Herrero, *Science* **2011**, *334*, 648.
[316] T. J. Echtermeyer, P. Nene, M. Trushin, R. V. Gorbachev, A. L. Eiden, S. Milana, Z. Sun, J. Schliemann, E. Lidorikis, K. S. Novoselov, A. C. Ferrari, *Nano Lett.* **2014**, *14*, 3733.
[317] M. Dai, C. Wang, B. Qiang, F. Wang, M. Ye, S. Han, Y. Luo, Q. J. Wang, *Nat. Commun.* **2022**, *13*, 4560.
[318] M. Dai, C. Wang, B. Qiang, Y. Jin, M. Ye, F. Wang, F. Sun, X. Zhang, Y. Luo, Q. J. Wang, *Nat. Commun.* **2023**, *14*, 3421.
[319] M. Buscema, M. Barkelid, V. Zwiller, H. S. van der Zant, G. A. Steele, A. Castellanos-Gomez, *Nano Lett.* **2013**, *13*, 358.
[320] Y. Yan, Z.-M. Liao, X. Ke, G. Van Tendeloo, Q. Wang, D. Sun, W. Yao, S. Zhou, L. Zhang, H.-C. Wu, D.-P. Yu, *Nano Lett.* **2014**, *14*, 4389.
[321] D. A. Mylnikov, M. A. Kashchenko, K. N. Kapralov, D. A. Ghazaryan, E. E. Vdovin, S. V. Morozov, K. S. Novoselov, D. A. Bandurin, A. I. Chernov, D. A. Svintsov, *npj 2D Mater. Appl.* **2024**, *8*, 34.
[322] J. Yan, M. H. Kim, J. A. Elle, A. B. Sushkov, G. S. Jenkins, H. M. Milchberg, M. S. Fuhrer, H. Drew, *Nat. Nanotechnol.* **2012**, *7*, 472.
[323] H. Vora, P. Kumaravadivel, B. Nielsen, X. Du, *Appl. Phys. Lett.* **2012**, *100*, 15.
[324] X. Wang, H. Shen, Y. Chen, G. Wu, P. Wang, H. Xia, T. Lin, P. Zhou, W. Hu, X. Meng, J. Chu, J. Wang, *Adv. Sci.* **2019**, *6*, 1901050.
[325] M. Du, X. Cui, H. H. Yoon, S. Das, M. G. Uddin, L. Du, D. Li, Z. Sun, *ACS Nano* **2022**, *16*, 568.
[326] D. Xu, Q. Liu, B. Liang, N. Yu, X. Ma, Y. Xu, T. Taniguchi, C. Ding, R. K. Lake, R. Yan, M. Liu, *Sci. Adv.* **2025**, *11*, eadv7614.
[327] M. Kumar, A. Saravanan, S.-C. Chen, B.-R. Huang, H. Sun, *Appl. Surf. Sci.* **2024**, *669*, 160504.
[328] W. Liu, X. Yang, Z. Wang, Y. Li, J. Li, Q. Feng, X. Xie, W. Xin, H. Xu, Y. Liu, *Light: Sci. Appl.* **2023**, *12*, 180.
[329] G. Konstantatos, M. Badioli, L. Gaudreau, J. Osmond, M. Bernechea, F. P. G. De Arquer, F. Gatti, F. H. Koppens, *Nat. Nanotechnol.* **2012**, *7*, 363.
[330] S. B. Mitta, F. Ali, Z. Yang, I. Moon, F. Ahmed, T. J. Yoo, B. H. Lee, W. J. Yoo, *ACS Appl. Mater. Interfaces* **2020**, *12*, 23261.
[331] M. Tian, Y. Wang, T. Zhang, C. Zhang, J. Miao, Z. Bian, X. Su, Z. Li, J. Chai, A. Wang, F. Wang, B. Yu, Y. Xu, Y. Chai, X. Wang, Y. Zhao, *Nat. Commun.* **2025**, *16*, 5824.
[332] S. Zhang, H. Jiao, Y. Chen, R. Yin, X. Huang, Q. Zhao, C. Tan, S. Huang, H. Yan, T. Lin, H. Shen, J. Ge, X. Meng, W. Hu, N. Dai, X. Wang, J. Chu, J. Wang, *Nat. Commun.* **2024**, *15*, 7071.
[333] Z. Fang, Z. Liu, Y. Wang, P. M. Ajayan, P. Nordlander, N. J. Halas, *Nano Lett.* **2012**, *12*, 3808.
[334] H. Jiang, Y. Chen, W. Guo, Y. Zhang, R. Zhou, M. Gu, F. Zhong, Z. Ni, J. Lu, C.-W. Qiu, W. Gao, *Nat. Commun.* **2024**, *15*, 8347.
[335] M. Long, E. Liu, P. Wang, A. Gao, H. Xia, W. Luo, B. Wang, J. Zeng, Y. Fu, K. Xu, W. Zhou, Y. Lv, S. Yao, M. Lu, Y. Chen, Z. Ni, Y. You, X. Zhang, S. Qin, Y. Shi, W. Hu, D. Xing, F. Miao, *Nano Lett.* **2016**, *16*, 2254.
[336] H. Jiao, X. Wang, Y. Chen, S. Guo, S. Wu, C. Song, S. Huang, X. Huang, X. Tai, T. Lin, H. Shen, H. Yan, W. Hu, X. Meng, J. Chu, Y. Zhang, J. Wang, *Sci. Adv.* **2022**, *8*, eabn1811.
[337] H. Ma, S. Lin, T. He, B. Tang, J. Wu, Y. Wang, Y. Ye, J. Jian, J. Wang, Z. Zhang, M. Wei, Y. Si, Y. Wu, J. Li, X. Qiao, D. Gao, L. Li, W. Hu, H. Lin, *ACS Photonics* **2024**, *11*, 3982.
[338] C. Liu, L. Tang, Y. Lv, L. Chen, Y. Qin, S. Zhang, S. Zhao, S. Ding, X. Zhang, P. Xu, C. Ma, X. Liu, F. Wang, P. Wang, X. Wang, Y. Liu, E.-G. Wang, L. Liao, X. Zou, *Nat. Commun.* **2025**, *16*, 3821.

[339] Q. Guo, A. Pospischil, M. Bhuiyan, H. Jiang, H. Tian, D. Farmer, B. Deng, C. Li, S.-J. Han, H. Wang, Q. Xia, T.-P. Ma, T. Mueller, F. Xia, *Nano Lett.* **2016**, *16*, 4648.
[340] M. Gong, B. Liu, A. Shultz, R. C. Schmitz, H. B. Vargas, S. Alzahrani, F. C. Robles Hernandez, A. Olson, J. Z. Wu, *ACS Nano* **2025**, *19*, 8520.
[341] M. Liu, L. Qi, Y. Zou, N. Zhang, F. Zhang, H. Xiang, Z. Liu, M. Qin, X. Sun, Y. Zheng, C. Lin, D. Li, S. Li, *Nat. Commun.* **2025**, *16*, 2774.
[342] W. Ahmad, J. Liu, J. Jiang, Q. Hao, D. Wu, Y. Ke, H. Gan, V. Laxmi, Z. Ouyang, F. Ouyang, F. Ouyang, Z. Wang, F. Liu, D. Qi, W. Zhang, *Adv. Funct. Mater.* **2021**, *31*, 2104143.
[343] B. Kundu, O. Özdemir, M. Dalmases, G. Kumar, G. Konstantatos, *Adv. Opt. Mater.* **2021**, *9*, 2101378.
[344] X. Liu, J. Zhu, Y. Shan, C. Liu, C. Pan, T. Zhang, C. Liu, T. Chen, J. Ling, J. Duan, F. Qiu, S. Rahman, H. Deng, N. Dai, *Adv. Sci.* **2024**, *11*, 2408299.
[345] J. Wu, J. Zhang, R. Jiang, H. Wu, S. Chen, X. Zhang, W. Wang, Y. Yu, Q. Fu, R. Lin, Y. Cui, T. Zhou, Z. Hu, D. Wan, X. Chen, W. Hu, H. Liu, J. Lu, Z. Ni, *Nat. Commun.* **2025**, *16*, 564.
[346] H. Agarwal, K. Nowakowski, A. Forrer, A. Principi, R. Bertini, S. Batlle-Porro, A. Reserbat-Plantey, P. Prasad, L. Vistoli, K. Watanabe, T. Taniguchi, A. Bachtold, G. Scalari, R. K. Kumar, F. H. L. Koppens, *Nat. Photonics* **2023**, *17*, 1047.
[347] J. Hwang, J. Song, H. Jang, Y. Seok, J. Park, S. Lee, J.-H. Choi, G. Lee, K. Watanabe, T. Taniguchi, et al., *Adv. Funct. Mater.* **2025**, 10113.
[348] D. Kufer, I. Nikitskiy, T. Lasanta, G. Navickaite, F. Koppens, G. Konstantatos, *Adv. Mater.* **2014**, *27*, 176.
[349] Y. Y. Hui, X. Liu, W. Jie, N. Y. Chan, J. Hao, Y.-T. Hsu, L.-J. Li, W. Guo, S. P. Lau, *ACS Nano* **2013**, *7*, 7126.
[350] H. H. Yoon, H. A. Fernandez, F. Nigmatulin, W. Cai, Z. Yang, H. Cui, F. Ahmed, X. Cui, M. G. Uddin, E. D. Minot, H. Lipsanen, K. Kim, P. Hakonen, T. Hasan, Z. Sun, *Science* **2022**, *378*, 296.
[351] M. G. Uddin, S. Das, A. M. Shafi, L. Wang, X. Cui, F. Nigmatulin, F. Ahmed, A. C. Liapis, W. Cai, Z. Yang, H. Lipsanen, T. Hasan, H. H. Yoon, Z. Sun, *Nat. Commun.* **2024**, *15*, 571.
[352] S. Yuan, D. Naveh, K. Watanabe, T. Taniguchi, F. Xia, *Nat. Photonics* **2021**, *15*, 601.
[353] X. Li, J. Wang, F. Yu, J. Chen, X. Chen, W. Lu, G. Li, *Light: Sci. Appl.* **2025**, *14*, 47.
[354] X. Du, Y. Wang, Y. Cui, G. Rao, J. Huang, X. Chen, T. Zhou, C. Wu, Z. Yang, H. Cui, Y. Zhao, J. Xiong, *Nat. Electron.* **2024**, *7*, 984.
[355] L. Du, T. Hasan, A. Castellanos-Gomez, G.-B. Liu, Y. Yao, C. N. Lau, Z. Sun, *Nat. Rev. Phys.* **2021**, *3*, 193.
[356] H. Li, L. Ye, J. Xu, *ACS Photonics* **2017**, *4*, 823.
[357] Y. Xiao, Z. Luo, Z. Qiu, Y. Liang, W. Gao, M. Yang, Y. Zhao, Z. Zheng, J. Yao, J. Li, *Small* **2025**, *21*, 2409843.
[358] S. Mukherjee, G. Samanta, M. N. Hasan, S. Moulick, R. Kulkarni, K. Watanabe, T. Taniguchi, A. Thamizhavel, D. Karmakar, A. N. Pal, *npj 2D Mater. Appl.* **2024**, *8*, 71.
[359] D.-H. Kang, S. R. Pae, J. Shim, G. Yoo, J. Jeon, J. W. Leem, J. S. Yu, S. Lee, B. Shin, J.-H. Park, *Adv. Mater.* **2016**, *28*, 7799.
[360] H. Song, S. Ji, S. G. Kang, N. Shin, *ACS Nano* **2024**, *18*, 19179.
[361] X. Tang, Y. Zheng, B. Cao, Q. Wu, J. Liang, W. Wang, G. Li, *ACS Appl. Nano Mater.* **2022**, *5*, 4515.
[362] H. Ghanbari, A. Abnavi, A. Hasani, F. Kabir, R. Ahmadi, M. R. Mohammadzadeh, M. Fawzy, T. De Silva, M. M. Adachi, *Nanotechnology* **2023**, *34*, 285207.
[363] Y. Zheng, B. Cao, X. Tang, Q. Wu, W. Wang, G. Li, *ACS Nano* **2022**, *16*, 2798.
[364] M. Auge, F. Junge, H. Hofsäss, *Nucl. Instrum. Methods Phys. Res., Sect. B* **2022**, *512*, 96.
[365] K. Xu, Y. Zhao, Z. Lin, Y. Long, Y. Wang, M. Chan, Y. Chai, *Semicond. Sci. Technol.* **2017**, *32*, 124002.
[366] B. Gao, Y. Yan, S. Zhang, Z. Wu, Y. Meng, Y. Zhang, W. Wang, Y. Shen, S. Hu, B. Li, H. Shao, P. Xie, S. Yip, J. C. Ho, *Adv. Funct. Mater.* **2025**, *35*, 2425884.
[367] L. Yang, K. Majumdar, H. Liu, Y. Du, H. Wu, M. Hatzistergos, P. Hung, R. Tieckelmann, W. Tsai, C. Hobbs, P. D. Ye, *Nano Lett.* **2014**, *14*, 6275.
[368] S. Aftab, M. Z. Iqbal, M. W. Iqbal, *Adv. Mater. Interfaces* **2022**, *9*, 2201219.
[369] X. Li, C. Xia, X. Song, J. Du, W. Xiong, *J. Mater. Sci.* **2017**, *52*, 7207.
[370] D. Wang, X.-B. Li, H.-B. Sun, *Nano Lett.* **2021**, *21*, 6298.
[371] D. Lee, J. J. Lee, Y. S. Kim, Y. H. Kim, J. C. Kim, W. Huh, J. Lee, S. Park, H. Y. Jeong, Y. D. Kim, C.-H. Lee, *Nat. Electron.* **2021**, *4*, 664.
[372] L. Lv, F. Zhuge, F. Xie, X. Xiong, Q. Zhang, N. Zhang, Y. Huang, T. Zhai, *Nat. Commun.* **2019**, *10*, 3331.
[373] J. Ye, K. Liao, X. Fu, F. Zhong, Q. Li, G. Wang, J. Miao, *Infrared Phys. Technol.* **2022**, *123*, 104139.
[374] S. Sovizi, S. Angizi, S. A. Ahmad Alem, R. Goodarzi, M. R. R. Taji Boyuk, H. Ghanbari, R. Szoszkiewicz, A. Simchi, P. Kruse, *Chem. Rev.* **2023**, *123*, 13869.
[375] X. S. Chu, A. Yousaf, D. O. Li, A. A. Tang, A. Debnath, D. Ma, A. A. Green, E. J. Santos, Q. H. Wang, *Chem. Mater.* **2018**, *30*, 2112.
[376] R. Kumar, A. K. Shringi, H. J. Wood, I. M. Asuo, S. Oturak, D. E. Sanchez, T. S. K. Sharma, R. Chaurasiya, A. Mishra, W. M. Choi, N. Y. Doumon, I. Dabo, M. Terrones, F. Yan, *Mater. Sci. Eng.: R: Reports* **2025**, *163*, 100946.
[377] C. Kim, T. J. Yoo, M. G. Kwon, K. E. Chang, H. J. Hwang, B. H. Lee, *Nanophotonics* **2022**, *11*, 1041.
[378] C. Liu, T. Zheng, K. Shu, S. Shu, Z. Lan, M. Yang, Z. Zheng, N. Huo, W. Gao, J. Li, *ACS Appl. Mater. Interfaces* **2024**, *16*, 13914.
[379] X. Cui, S. Kim, F. Ahmed, M. Du, A. C. Liapis, J. A. Mu noz, A. M. Shafi, M. G. Uddin, F. Ali, Y. Zhang, D.-H. Kang, H. Lipsanen, S. Kang, H. H. Yoon, Z. Sun, *Appl. Phys. Lett.* **2024**, *125*, 5.
[380] S.-T. Varjamo, C. Edwards, Y. Zhou, R. Fang, S. H. Hosseini Shokouh, Z. Sun, *Nano Lett.* **2025**, *25*, 4379.
[381] S. Wu, J. Deng, X. Wang, J. Zhou, H. Jiao, Q. Zhao, T. Lin, H. Shen, X. Meng, Y. Chen, J. Chu, J. Wang, *Nat. Commun.* **2024**, *15*, 8743.
[382] S. Fan, S. J. Yun, W. J. Yu, Y. H. Lee, *Adv. Sci.* **2020**, *7*, 1902751.
[383] C. Zhou, S. Zhang, Z. Lv, Z. Ma, C. Yu, Z. Feng, M. Chan, *npj 2D Mater. Appl.* **2020**, *4*, 46.
[384] M. Dai, C. Wang, M. Ye, S. Zhu, S. Han, F. Sun, W. Chen, Y. Jin, Y. Chua, Q. J. Wang, *ACS Nano* **2022**, *16*, 295.
[385] A. Abnavi, R. Ahmadi, H. Ghanbari, M. Fawzy, A. Hasani, T. De Silva, A. M. Askar, M. R. Mohammadzadeh, F. Kabir, M. Whitwick, M. Beaudoin, S. K. O'Leary, M. M. Adachi, *Adv. Funct. Mater.* **2023**, *33*, 2210619.
[386] H. Ghanbari, A. Abnavi, R. Ahmadi, M. R. Mohammadzadeh, M. Fawzy, A. Hasani, M. M. Adachi, *Adv. Opt. Mater.* **2024**, *12*, 2401682.
[387] X. Zhang, D. Qiu, P. Hou, *ACS Appl. Mater. Interfaces* **2025, 17, 31543**.
[388] X. Ren, X. Li, X. He, X. An, Y. Li, B. Gao, F. Gao, J. Zhang, P. Hu, *Chem. Eng. J.* **2024**, *496*, 153937.
[389] J. Liu, K. Xing, L. Li, W. Zhao, A. Stacey, I. Robertson, D. A. Broadway, J.-P. Tetienne, D.-C. Qi, M. S. Fuhrer, Y. Hao, Q. Ou, *ACS Nano* **2025**, *19*, 27919.
[390] H. Kim, S. Z. Uddin, N. Higashitarumizu, E. Rabani, A. Javey, *Science* **2021**, *373*, 448.
[391] E. Yablonovitch, E. Kane, *J. Lightwave Technol.* **1988**, *6*, 1292.
[392] S. E. Thompson, M. Armstrong, C. Auth, M. Alavi, M. Buehler, R. Chau, S. Cea, T. Ghani, G. Glass, T. Hoffman, C.-H. Jan, C. Kenyon, J. Klaus, K. Kuhn, Z. Ma, B. Mcintyre, K. Mistry, A. Murthy, B. Obradovic, R. Nagisetty, P. Nguyen, S. Sivakumar, R. Shaheed, L. Shifren, B. Tufts, S. Tyagi, M. Bohr, Y. El-Mansy, *IEEE Trans. Electron Devices* **2004**, *51*, 1790.

[393] Y. Chen, Y. Lei, Y. Li, Y. Yu, J. Cai, M.-H. Chiu, R. Rao, Y. Gu, C. Wang, W. Choi, H. Hu, C. Wang, Y. Li, J. Song, J. Zhang, B. Qi, M. Lin, Z. Zhang, A. E. Islam, B. Maruyama, S. Dayeh, L.-J. Li, K. Yang, Y.-H. Lo, S. Xu, *Nature* **2020**, *577*, 209.
[394] G. Zhang, T. Albrow-Owen, W. Peng, X. Liang, X. Zhang, P. Wang, D. Di, S. Dong, J. Luo, G. Wang, H. Mu, Q. Zhao, X. Guo, Q. J. Wang, T. Hasan, Z. Yang, *Sci. Adv.* **2025**, *11*, eadu4225.
[395] T. L. Vasconcelos, S. N. Vladimirov, T. Pucher, S. Puebla, C. Munuera, E. R. Hernández, A. Castellanos-Gomez, *Nano Lett.* **2025**, *25*, 11333.
[396] M. Jaikissoon, Ç. Köroğlu, J. A. Yang, K. Neilson, K. C. Saraswat, E. Pop, *Nat. Electron.* **2024**, *7*, 885.
[397] I. M. Datye, A. Daus, R. W. Grady, K. Brenner, S. Vaziri, E. Pop, *Nano Lett.* **2022**, *22*, 8052.
[398] L. Hoang, M. Jaikissoon, C. Köroğlu, Z. Zhang, R. K. Bennett, J.-H. Song, J. A. Yang, J.-S. Ko, M. L. Brongersma, K. C. Saraswat, E. Pop, A. J. Mannix, *Nano Lett.* **2024**, *24*, 12768.
[399] C. R. Paul Inbaraj, R. J. Mathew, R. K. Ulaganathan, R. Sankar, M. Kataria, H. Y. Lin, Y.-T. Chen, M. Hofmann, C.-H. Lee, Y.-F. Chen, *ACS Nano* **2021**, *15*, 8686.
[400] H. Kim, S. Z. Uddin, D.-H. Lien, M. Yeh, N. S. Azar, S. Balendhran, T. Kim, N. Gupta, Y. Rho, C. P. Grigoropoulos, K. B. Crozier, A. Javey, *Nature* **2021**, *596*, 232.
[401] Y. Han, L. Gao, J. Zhou, Y. Hou, Y. Jia, K. Cao, K. Duan, Y. Lu, *ACS Appl. Mater. Interfaces* **2022**, *14*, 8655.
[402] P. Kang, K.-H. Kim, H.-G. Park, S. Nam, *Light: Sci. Appl.* **2018**, *7*, 17.
[403] H. Zeng, H. Yu, B. Liu, S. Lu, X. Wei, L. Gao, M. Hong, X. Zhang, Z. Zhang, Y. Zhang, *Adv. Funct. Mater.* **2024**, *34*, 2400712.
[404] K. Yang, Y. Lee, D. Rhee, B. Choi, A. Alfieri, M. Drndić, D. Jariwala, G.-H. Lee, *Adv. Sci.* **2025**, *12*, 06488.
[405] Y. Cao, V. Fatemi, S. Fang, K. Watanabe, T. Taniguchi, E. Kaxiras, P. Jarillo-Herrero, *Nature* **2018**, *556*, 43.
[406] J. H. Pixley, E. Y. Andrei, *Science* **2019**, *365*, 543.
[407] A. L. Sharpe, E. J. Fox, A. W. Barnard, J. Finney, K. Watanabe, T. Taniguchi, M. Kastner, D. Goldhaber-Gordon, *Science* **2019**, *365*, 605.
[408] Y. Cao, V. Fatemi, A. Demir, S. Fang, S. L. Tomarken, J. Y. Luo, J. D. Sanchez-Yamagishi, K. Watanabe, T. Taniguchi, E. Kaxiras, R. C. Ashoori, P. Jarillo-Herrero, *Nature* **2018**, *556*, 80.
[409] K. Tran, G. Moody, F. Wu, X. Lu, J. Choi, K. Kim, A. Rai, D. A. Sanchez, J. Quan, A. Singh, J. Embley, A. Zepeda, M. Campbell, T. Autry, T. Taniguchi, K. Watanabe, N. Lu, S. K. Banerjee, K. L. Silverman, S. Kim, E. Tutuc, L. Yang, L. H. MacDonald, X. Li, *Nature* **2019**, *567*, 71.
[410] K. L. Seyler, P. Rivera, H. Yu, N. P. Wilson, E. L. Ray, D. G. Mandrus, J. Yan, W. Yao, X. Xu, *Nature* **2019**, *567*, 66.
[411] C. Ma, S. Yuan, P. Cheung, K. Watanabe, T. Taniguchi, F. Zhang, F. Xia, *Nature* **2022**, *604*, 266.
[412] J. Yin, H. Wang, H. Peng, Z. Tan, L. Liao, L. Lin, X. Sun, A. L. Koh, Y. Chen, H. Peng, Z. Liu, *Nat. Commun.* **2016**, *7*, 10699.
[413] B. Deng, C. Ma, Q. Wang, S. Yuan, K. Watanabe, T. Taniguchi, F. Zhang, F. Xia, *Nat. Photonics* **2020**, *14*, 549.
[414] F. Wang, S. Zhu, W. Chen, J. Han, R. Duan, C. Wang, M. Dai, F. Sun, Y. Jin, Q. J. Wang, *Nat. Nanotechnol.* **2024**, *19*, 455.
[415] J. Wang, Y. Fang, Y. Jiang, S. Long, X. Ma, X. Fu, Y. She, Q. Zhao, Y. Chen, H. Xu, T. Li, F. Zhong, H. Lin, X. Chen, J. Miao, *Appl. Phys. Lett.* **2024**, *124*, 12.
[416] F. Tan, C. Chang, N. Zhang, J. An, M. Liu, X. Zhao, M. Che, Z. Liu, Y. Shi, Y. Li, Y. Feng, C. Lin, Y. Zheng, D. Li, M. Lanza, S. Li, *Light: Sci. Appl.* **2025**, *14*, 122.
[417] Y. Liu, L. Lin, H.-B. Sun, *J. Phys. Chem. C* **2024**, *128*, 2271.
[418] S.-T. M. Akkanen, H. A. Fernandez, Z. Sun, *Adv. Mater.* **2022**, *34*, 2110152.
[419] A. Venkatakrishnan, H. Chua, P. Tan, Z. Hu, H. Liu, Y. Liu, A. Carvalho, J. Lu, C. H. Sow, *ACS Nano* **2017**, *11*, 713.
[420] F. Ahmed, C. Rodríguez-Fernández, H. A. Fernandez, Y. Zhang, A. M. Shafi, M. G. Uddin, X. Cui, H. H. Yoon, N. Mehmood, A. C. Liapis, L. Yao, H. Caglayan, Z. Sun, H. Lipsanen, *Adv. Funct. Mater.* **2023**, *33*, 2302051.
[421] H. Chang, Y. Yang, R. Zhang, Q. Bai, X. Huang, L. Wan, J. Li, *Adv. Electron. Mater.* **2025**, *11*, 2500064.
[422] J. Zhang, C. Triola, E. Rossi, *Phys. Rev. Lett.* **2014**, *112*, 096802.
[423] A. Avsar, J. Y. Tan, T. Taychatanapat, J. Balakrishnan, G. Koon, Y. Yeo, J. Lahiri, A. Carvalho, A. Rodin, E. O'farrell, G. Eda, A. H. C. Neto, B. Özyilmaz, *Nat. Commun.* **2014**, *5*, 4875.
[424] S. Cha, M. Noh, J. Kim, J. Son, H. Bae, D. Lee, H. Kim, J. Lee, H.-S. Shin, S. Sim, S. Yang, S. Lee, W. Shim, C.-H. Lee, M.-H. Jo, J. S. Kim, D. Kim, H. Choi, *Nat. Nanotechnol.* **2018**, *13*, 910.
[425] D. Khokhriakov, A. M. Hoque, B. Karpiak, S. P. Dash, *Nat. Commun.* **2020**, *11*, 3657.
[426] L. Powalla, J. Kiemle, E. J. König, A. P. Schnyder, J. Knolle, K. Kern, A. Holleitner, C. Kastl, M. Burghard, *Nat. Commun.* **2022**, *13*, 3152.
[427] S. D. Ganichev, E. Ivchenko, V. Bel'Kov, S. Tarasenko, M. Sollinger, D. Weiss, W. Wegscheider, W. Prettl, *Nature* **2002**, *417*, 153.
[428] S. Wu, Y. Chen, X. Wang, H. Jiao, Q. Zhao, X. Huang, X. Tai, Y. Zhou, H. Chen, X. Wang, S. Huang, H. Yan, T. Lin, H. Shen, W. Hu, X. Meng, J. Chu, J. Wang, *Nat. Commun.* **2022**, *13*, 3198.
[429] T. Akamatsu, T. Ideue, L. Zhou, Y. Dong, S. Kitamura, M. Yoshii, D. Yang, M. Onga, Y. Nakagawa, K. Watanabe, T. Taniguchi, J. Laurienzo, J. Huang, Z. Ye, T. Morimoto, H. Yuan, Y. Iwasa, *Science* **2021**, *372*, 68.
[430] Z. Chen, X. Li, J. Wang, L. Tao, M. Long, S.-J. Liang, L. K. Ang, C. Shu, H. K. Tsang, J.-B. Xu, *ACS Nano* **2017**, *11*, 430.
[431] B. Lee, W. Liu, C. H. Naylor, J. Park, S. C. Malek, J. S. Berger, A. C. Johnson, R. Agarwal, *Nano Lett.* **2017**, *17*, 4541.
[432] B. Zeng, Z. Huang, A. Singh, Y. Yao, A. K. Azad, A. D. Mohite, A. J. Taylor, D. R. Smith, H.-T. Chen, *Light: Sci. Appl.* **2018**, *7*, 51.
[433] Q. Guo, R. Yu, C. Li, S. Yuan, B. Deng, F. J. García de Abajo, F. Xia, *Nat. Mater.* **2018**, *17*, 986.
[434] S. Castilla, I. Vangelidis, V.-V. Pusapati, J. Goldstein, M. Autore, T. Slipchenko, K. Rajendran, S. Kim, K. Watanabe, T. Taniguchi, L. Martin-Moreno, D. Englund, K.-J. Tielrooij, R. Hillenbrand, E. Lidorikis, F. H. L. Koppens, *Nat. Commun.* **2020**, *11*, 4872.
[435] J. Wei, Y. Chen, Y. Li, W. Li, J. Xie, C. Lee, K. S. Novoselov, C.-W. Qiu, *Nat. Photonics* **2023**, *17*, 171.
[436] C. Park, S. H. Han, H. J. Jin, W. Hong, S.-Y. Choi, *ACS Nano* **2023**, *17*, 9262.
[437] H. Cai, C. Yang, L. Shen, Y. Yu, X. Zhang, *ACS Photonics* **2024**, *11*, 1565.
[438] H. Jiang, J. Fu, J. Wei, S. Li, C. Nie, F. Sun, Q. Y. S. Wu, M. Liu, Z. Dong, X. Wei, W. Gao, C.-W. Qiu, *Nat. Commun.* **2024**, *15*, 1225.
[439] H. Song, S. Chen, X. Sun, Y. Cui, T. Yildirim, J. Kang, S. Yang, F. Yang, Y. Lu, L. Zhang, *Adv. Sci.* **2024**, *11*, 2403176.
[440] V. Semkin, A. Shabanov, K. Kapralov, M. Kashchenko, A. Sobolev, I. Mazurenko, V. Myltsev, D. Mylnikov, E. Nikulin, A. Chernov, I. Mazurenko, V. Myltsev, D. Mylnikov, E. Nikulin, A. Chernov, E. Kameneva, A. Bocharov, D. Svintsov, *Adv. Opt. Mater.* **2025**, *13*, 2403189.
[441] J. Deng, M. Shi, X. Liu, J. Zhou, X. Qin, R. Wang, Y. Zhen, X. Dai, Y. Chen, J. Wei, Z. Ni, W. Gao, C.-W. Qiu, X. Chen, *Nat. Electron.* **2024**, *7*, 1004.
[442] C. Jung, E. Lee, J. Rho, *Sci. Adv.* **2024**, *10*, eado8964.
[443] G. Kim, D. Kim, S. Ko, J.-H. Han, J. Kim, J. H. Ko, Y. M. Song, H.-H. Jeong, *Microsyst. Nanoeng.* **2024**, *10*, 22.
[444] J. H. Ko, D. H. Seo, H.-H. Jeong, S. Kim, Y. M. Song, *Adv. Mater.* **2024**, *36*, 2310556.

[445] Z. Zhang, T. Cai, Z. Li, B. Wu, Z. Zheng, C. You, G. Jiang, M. Ma, Z. Xu, C. Shen, X.-z. Chen, E. Song, J. Cui, G. Huang, Y. Mei, *Adv. Mater.* **2025**, *37*, 2413771.
[446] F. Han, K. Pilarczyk, Z. Lin, C. Sun, G. A. Vandenbosch, J. Van de Vondel, P. Van Dorpe, X. Zheng, N. Verellen, E. Janssens, *Laser Photonics Rev.* **2025**, *19*, 2402258.
[447] Y. Luo, Z. Sun, Z. Sun, Q. Dai, *Adv. Mater.* **2025**, *37*, 2413748.
[448] L. Chen, T. Lin, J. Chai, Q. Hao, L. Lei, J. Chen, W. Wang, G. Li, *Appl. Phys. Lett.* **2025**, *126*, 12.
[449] P. G. Zotev, P. Bouteyre, Y. Wang, S. A. Randerson, X. Hu, L. Sortino, Y. Wang, T. Shegai, S.-H. Gong, A. Tittl, I. Aharonovich, A. I. Tartakovskii, *Nat. Photonics* **2025**, *19*, 1.
[450] X. Liu, K. Zhao, Q. Mai, Y. Li, J. Wen, F. Tan, B. Li, *Adv. Funct. Mater.* **2025**, 12872.
[451] Z. Wu, H. Dong, T. Xu, Y. Wang, C. Zhou, R. Li, Q. Yin, Y. Ye, J. Zhou, J. Xue, *ACS Photonics* **2025**, *12*, 4886.
[452] P. Pantyukhina, A. Bogdanov, K. Koshelev, *Phys. Rev. B* **2025**, *112*, L081405.
[453] S. Han, J. Kong, J. Choi, W. Chegal, M. S. Jang, *Light: Sci. Appl.* **2025**, *14*, 292.
[454] I. Lee, S. Rathi, D. Lim, L. Li, J. Park, Y. Lee, K. S. Yi, K. P. Dhakal, J. Kim, C. Lee, G.-H. Lee, Y. D. Kim, J. Hone, S. J. Yun, D.-H. Youn, G.-H. Kim, *Adv. Mater.* **2016**, *28*, 9519.
[455] C. Zhang, K. Wu, L. Gan, X. Liu, C. Zhang, S. Wu, X. Yuan, L. Zhang, J. Xi, J. Yang, X. Li, *ACS Nano* **2024**, *18*, 33520.
[456] Y. Chen, C. Tan, Z. Wang, J. Miao, X. Ge, T. Zhao, K. Liao, H. Ge, Y. Wang, F. Wang, Y. Zhou, P. Wang, X. Zhou, C. Shan, H. Peng, W. Hu, *Sci. Adv.* **2022**, *8*, eabq1781.
[457] R. Hu, H. Wang, Y. Gao, Y. Li, A. Cao, Z. Wang, L. Shang, Y. Li, K. Jiang, J. Zhang, L. Zhu, Z. Hu, *ACS Appl. Nano Mater.* **2024**, *7*, 28798.
[458] C. Kim, I. Moon, D. Lee, M. S. Choi, F. Ahmed, S. Nam, Y. Cho, H.-J. Shin, S. Park, W. J. Yoo, *ACS Nano* **2017**, *11*, 1588.
[459] J. Jang, H.-S. Ra, J. Ahn, T. W. Kim, S. H. Song, S. Park, T. Taniguch, K. Watanabe, K. Lee, D. K. Hwang, *Adv. Mater.* **2022**, *34*, 2109899.
[460] X. Liu, M. S. Choi, E. Hwang, W. J. Yoo, J. Sun, *Adv. Mater.* **2022**, *34*, 2108425.
[461] E. Park, S.-H. Kim, S.-J. Min, K.-H. Han, J.-H. Kim, S.-G. Kim, T.-H. Ahn, H.-Y. Yu, *ACS Nano* **2024**, *18*, 29771.
[462] J. S. Ross, P. Rivera, J. Schaibley, E. Lee-Wong, H. Yu, T. Taniguchi, K. Watanabe, J. Yan, D. Mandrus, D. Cobden, W. Yao, X. Xu, *Nano Lett.* **2017**, *17*, 638.
[463] Y. Liu, Z. Qiu, A. Carvalho, Y. Bao, H. Xu, S. J. Tan, W. Liu, A. Castro Neto, K. P. Loh, J. Lu, *Nano Lett.* **2017**, *17*, 1970.
[464] W. Liu, M. Peng, M. Chen, Y. Zhao, Y. Yu, P. Jian, Z. Liu, Y. Zeng, Y. Luo, X. Tian, Z. Gao, J. Dai, C. Chen, F. Wu, W. Hu, *Adv. Sci.* **2025**, *12*, 2417428.
[465] H. Xu, R. Xie, J. Miao, Z. Zhang, H. Ge, X. Shi, M. Luo, J. Wang, T. Li, X. Fu, J. C. Ho, P. Zhou, F. Wang, W. Hu, *Light: Sci. Appl.* **2025**, *14*, 72.
[466] J. Xiao, M. Zhao, Y. Wang, X. Zhang, *Nanophotonics* **2017**, *6*, 1309.
[467] S. Ovesen, S. Brem, C. Linderälv, M. Kuisma, T. Korn, P. Erhart, M. Selig, E. Malic, *Commun. Phys.* **2019**, *2*, 23.
[468] D.-H. Lien, S. Z. Uddin, M. Yeh, M. Amani, H. Kim, J. W. Ager III, E. Yablonovitch, A. Javey, *Science* **2019**, *364*, 468.
[469] S. Zhao, Y. Cheng, L. Tao, *ACS Photonics* **2024**, *11*, 2529.
[470] D. Unuchek, A. Ciarrocchi, A. Avsar, K. Watanabe, T. Taniguchi, A. Kis, *Nature* **2018**, *560*, 340.
[471] Q. Ju, Q. Cai, C. Jian, W. Hong, F. Sun, B. Wang, W. Liu, *Adv. Mater.* **2024**, *36*, 2404371.
[472] S. Poudyal, M. Deka, P. Adhikary, P. K. Barman, R. Yadav, B. Biswal, R. Rajarapu, S. Mukherjee, B. R. K. Nanda, A. Singh, A. Misra, *Nano Lett.* **2024**, *24*, 9575.
[473] C. Chakraborty, K. M. Goodfellow, S. Dhara, A. Yoshimura, V. Meunier, A. N. Vamivakas, *Nano Lett.* **2017**, *17*, 2253.
[474] L. Cavalcante, D. R. da Costa, G. Farias, D. Reichman, A. Chaves, *Phys. Rev. B* **2018**, *98*, 245309.
[475] J. G. Roch, N. Leisgang, G. Froehlicher, P. Makk, K. Watanabe, T. Taniguchi, C. Schonenberger, R. J. Warburton, *Nano Lett.* **2018**, *18*, 1070.
[476] Y. Li, S. Yang, J. Li, *J. Phys. Chem. C* **2014**, *118*, 23970.
[477] H. Yang, J. Heo, S. Park, H. J. Song, D. H. Seo, K.-E. Byun, P. Kim, I. Yoo, H.-J. Chung, K. Kim, *Science* **2012**, *336*, 1140.
[478] Y. J. Choi, S. B. Jo, J. H. Cho, *Adv. Mater.* **2021**, *33*, 2102725.
[479] cS. Kim, S. B. Jo, J. H. Cho, *Chem. Commun.* **2023**, *59*, 974.
[480] C. Strobel, C. A. Chavarin, M. Knaut, C. Wenger, A. Heinzig, T. Mikolajick, *Adv. Opt. Mater.* **2025**, *13*, 2500344.
[481] L. Liu, S. Ni, F. Zhu, Y. Zhu, C. Liu, X. Zhang, H. Zhu, J. Zhang, D. Zhang, C. Pan, L. Han, W. Tang, G. Li, H. Shu, X. Chen, *InfoMat* **2025**, *7*, 12641.
[482] Y. Chen, Y. Wang, Z. Wang, Y. Gu, Y. Ye, X. Chai, J. Ye, Y. Chen, R. Xie, Y. Zhou, Z. Hu, Q. Li, L. Zhang, F. Wang, P. Wang, J. Miao, J. Wang, X. Chen, W. Lu, P. Zhou, W. Hu, *Nat. Electron.* **2021**, *4*, 357.
[483] L. Wei, Z. Wu, Y. Wei, C. Li, Z. Fu, J. Han, X. Yang, J. Xie, Z. Tian, H. Zhou, J. Wang, *Adv. Funct. Mater.* **2024**, *34*, 2411736.
[484] S. Yan, J. Yang, Y. Cai, Y. Wang, S. Li, X. Zhan, F. Wang, J. He, Z. Wang, *Small* **2024**, *20*, 2401996.
[485] Z.-A. Li, C. Pan, P. Wang, Y. Yang, W. Yu, Y. Zhao, G. Ruan, C. Wang, J. Mei, P. Zeng, X. Wang, J. Mei, P. Zeng, X. Wang, Z. Ni, B. Cheng, S.-J. Liang, F. Miao, *ACS Nano* **2025**, *19*, 6263.
[486] X. Xu, J. Chen, H. Wu, D. Guo, J. Li, S. Zhang, Y. Xiao, K. Deng, T. He, H. Wang, Z. Wang, F. Wang, F. Zhong, P. Wang, Q. Li, W. Hu, *ACS Nano* **2025**, *19*, 18747.
[487] W. Gan, M. Li, C. Zhang, G. Peng, Z. Cao, Z. Chen, Y. Li, C. Wu, X. Liu, L. Song, *ACS Appl. Mater. Interfaces* **2025**, *17*, 34086.
[488] S. Wang, X. Wang, W. Wang, T. Han, F. Li, L. Shan, M. Long, *Adv. Sci.* **2025**, *12*, 2413844.
[489] F. Wang, S. Zhu, W. Chen, R. Duan, T. Dai, H. Ma, C. Yan, S. Fang, J. Yu, Y. Zhang, Q. Dong, W. Deng, Z. Liu, Q. J. Wang, *Light: Sci. Appl.* **2025**, *14*, 246.
[490] X. Li, Z. Li, J. Hu, B. Huang, J. Shi, Z. Zhong, Y. Zhuang, Y. Chen, J. Wang, J. Li, L. Zhang, X. Meng, W. Shi, S. Chen, X. Fang, H. Huang, J. Wang, J. Chu, *Nat. Commun.* **2025**, *16*, 2209.
[491] B. Huang, X. Li, J. Shi, J. Hu, Z. Zhong, Y. Zhuang, J. Zhang, W. Shi, X. Fang, H. Huang, J. Wang, J. Chu, *Nanoscale* **2025**, *17*, 23539.
[492] Z. Zhu, L. Liu, S. Deng, N. Xu, *ACS Nano* **2025**, *19*, 3645.
[493] Y. Li, X. He, S.-C. Chen, N. Zhao, *Chem. Rev.* **2025**, *125*, 6977.
[494] M. S. Ergoktas, G. Bakan, E. Kovalska, L. W. Le Fevre, R. P. Fields, P. Steiner, X. Yu, O. Salihoglu, S. Balci, V. I. Fal'ko, K. S. Novoselov, R. A. W. Dryfe, C. Kocabas, *Nat. Photonics* **2021**, *15*, 493.
[495] T. I. Andersen, R. J. Gelly, G. Scuri, B. L. Dwyer, D. S. Wild, R. Bekenstein, A. Sushko, J. Sung, Y. Zhou, A. A. Zibrov, X. Liu, A. Y. Joe, K. Watanabe, T. Taniguchi, S. F. Yelin, P. Kim, H. Park, M. D. Lukin, *Nat. Commun.* **2022**, *13*, 3431.
[496] J.-H. Lee, E. K. Lee, W.-J. Joo, Y. Jang, B.-S. Kim, J. Y. Lim, S.-H. Choi, S. J. Ahn, J. R. Ahn, M.-H. Park, C.-W. Yang, B. L. Choi, S.-W. Hwang, D. Whang, *Science* **2014**, *344*, 286.
[497] M. S. Bresnehan, M. J. Hollander, M. Wetherington, M. LaBella, K. A. Trumbull, R. Cavalero, D. W. Snyder, J. A. Robinson, *ACS Nano* **2012**, *6*, 5234.
[498] H. Yu, M. Liao, W. Zhao, G. Liu, X. Zhou, Z. Wei, X. Xu, K. Liu, Z. Hu, K. Deng, S. Zhou, J.-A. Shi, L. Gu, C. Shen, T. Zhang, L. Du, L. Xie, J. Zhu, W. Chen, r. Yang, D. Shi, G. Zhang, *ACS Nano* **2017**, *11*, 12001.

[499] S. H. Shin, D.-H. Kang, H. H. Yoon, J. Y. Park, M. Song, H. Son, D. Ha, H.-J. Shin, *Nano Lett.* **2025**, *25*, 7224.
[500] J. Joo, J. H. Kang, C.-H. Lee, G.-H. Lee, *2D Mater.* **2025**, *12*, 043003.
[501] H. H. Yoon, J. Y. Park, Y. T. Megra, J. H. Baek, M. Song, D. Akinwande, D. Ha, D.-H. Kang, H.-J. Shin, *npj 2D Mater. Appl.* **2025**, *9*, 68.
[502] P. Bøggild, T. J. Booth, B. S. Jessen, A. Shivayogimath, N. Lassaline, S. Hofmann, O. Burton, K. Daasbjerg, A. Smith, K. Nørgaard, A. Zurutuza, T. Barkan, A. J. Pollard, *Nat. Rev. Phys.* **2025**, *7*, 1.
[503] S. Bianconi, V. K. Sangwan, S. V. Rangnekar, J. Rabinowitz, C.-M. Kang, L. M. Guiney, M. C. Hersam, H. Mohseni, *ACS Photonics* **2025**, *12*, 1507.
[504] S. Goossens, G. Navickaite, C. Monasterio, S. Gupta, J. J. Piqueras, R. Pérez, G. Burwell, I. Nikitskiy, T. Lasanta, T. Galán, E. Puma, A. Centeno, A. Pesquera, A. Zurut, *Nat. Photonics* **2017**, *11*, 366.
[505] S. Fukamachi, P. Solís-Fernández, K. Kawahara, D. Tanaka, T. Otake, Y.-C. Lin, K. Suenaga, H. Ago, *Nat. Electron.* **2023**, *6*, 126.
[506] X. Cai, Y. Luo, B. Liu, H.-M. Cheng, *Chem. Soc. Rev.* **2018**, *47*, 6224.
[507] X. Xu, T. Guo, H. Kim, M. K. Hota, R. S. Alsaadi, M. Lanza, X. Zhang, H. N. Alshareef, *Adv. Mater.* **2022**, *34*, 2108258.
[508] Y. Huang, Y.-H. Pan, R. Yang, L.-H. Bao, L. Meng, H.-L. Luo, Y.-Q. Cai, G.-D. Liu, W.-J. Zhao, Z. Zhou, L.-M. Wu, Z.-L. Zhu, M. Huang, L.-W. Liu, L. Liu, P. Cheng, K.-H. Wu, S.-B. Tian, C.-Z. Gu, Y.-G. Shi, Y.-F. Guo, Z. G. Cheng, J.-P. Hu, L. Zhao, H.-J. Gao, *Nat. Commun.* **2020**, *11*, 2453.
[509] Y.-C. Lee, S.-W. Chang, S.-H. Chen, S.-L. Chen, H.-L. Chen, *Adv. Sci.* **2022**, *9*, 2102128.
[510] Y. Liu, Q. Tang, M. Xu, J. Ren, C. Guo, C. Chen, W. Geng, W. Lei, X. Zhao, D. Liu, *Chem. Eng. J.* **2023**, *468*, 143439.
[511] Z. Cai, B. Liu, X. Zou, H.-M. Cheng, *Chem. Rev.* **2018**, *118*, 6091.
[512] X. Zhang, J. Lai, T. Gray, *Oxford Open Mater. Sci.* **2023**, *3*, itad010.
[513] M. C. Lemme, D. Akinwande, C. Huyghebaert, C. Stampfer, *Nat. Commun.* **2022**, *13*, 1392.
[514] A. Reina, X. Jia, J. Ho, D. Nezich, H. Son, V. Bulovic, M. S. Dresselhaus, J. Kong, *Nano Lett.* **2009**, *9*, 30.
[515] X. Li, Y. Zhu, W. Cai, M. Borysiak, B. Han, D. Chen, R. D. Piner, L. Colombo, R. S. Ruoff, *Nano Lett.* **2009**, *9*, 4359.
[516] S. Jung, H. H. Yoon, H. Jin, K. Mo, G. Choi, J. Lee, H. Park, K. Park, *J. Appl. Phys.* **2019**, *125*, 18.
[517] Y. Zhao, Y. Song, Z. Hu, W. Wang, Z. Chang, Y. Zhang, Q. Lu, H. Wu, J. Liao, W. Zou, X. Gao, K. Jia, L. Zhuo, J. Hu, Q. Xie, R. Zhang, X. Wang, L. Sun, F. Li, L. Zheng, M. Wang, J. Yang, B. Mao, T. Fang, Z. Liu, *PatanèNat. Commun.* **2022**, *13*, 4409.
[518] C. A. Bhuyan, K. K. Madapu, K. Prabakar, A. Das, S. Polaki, S. K. Sinha, S. Dhara, *Adv. Mater. Interfaces* **2022**, *9*, 2200030.
[519] Q. Li, M. Wang, Y. Bai, Q. Zhang, H. Zhang, Z. Tian, Y. Guo, J. Zhu, Y. Liu, F. Yun, T. Wang, Y. Hao, *Adv. Funct. Mater.* **2022**, *32*, 2206094.
[520] M. Nakatani, S. Fukamachi, P. Solís-Fernández, S. Honda, K. Kawahara, Y. Tsuji, Y. Sumiya, M. Kuroki, K. Li, Q. Liu, Y. C. Lin, A. Uchida, S. Oyama, H. G. Ji, K. Okada, K. Suenaga, Y. Kawano, K. Yoshizawa, A. Yasui, H. Ago, *Nat. Electron.* **2024**, *7*, 119.
[521] J. Pyo, J. Lim, J. Byeon, S. Park, S. Kang, S. Park, S.-T. Lee, E. Kim, M. K. Kim, J. I. Sohn, J. Hong, J. Cho, K.-H. Park, S. Cha, S. Park, *ACS Nano* **2025**.
[522] X. Zhang, L. Zhou, S. Wang, T. Li, H. Du, Y. Zhou, J. Liu, J. Zhao, L. Huang, H. Yu, P. Chen, N. Li, *Nat. Commun.* **2025**, *16*, 4468.
[523] K. Xing, D. McEwen, Y. Yin, W. Zhao, A. Bake, D. Cortie, J. Liu, T.-H.-Y. Vu, Y.-H. Chen, J. Hone, A. Stacey, M. T. Edmonds, N. V. Medhekar, K. Watanabe, T. Taniguchi, Q. Ou, D. -C. Qi, M. S. Fuhrer, *ACS Nano* **2025**, *19*, 3579.
[524] J.-Y. Moon, S. Bae, J. Ryu, S.-I. Kim, S. Han, J. S. Kim, J. Choi, S. Kim, J.-H. Lee, S.-G. Choi, T.-R. Liu, S. Ahn, J. Seo, J.-H. Choi, H. J. Kwun, Y. -T. Shao, H.-D. Kim, J.-H. Park, J.-W. Lee, J.-W. Park, J.-H. Lee, J.-H. Ahn, S.-H. Bae, *Adv. Mater.* **2025**, 13080.
[525] V. L. Nguyen, M. Seol, J. Kwon, E.-K. Lee, W.-J. Jang, H. W. Kim, C. Liang, J. H. Kang, J. Park, M. S. Yoo, H. J. Shin, *Nat. Electron.* **2023**, *6*, 146.
[526] H. Al-Mumen, F. Rao, W. Li, L. Dong, *Nano-Micro Lett.* **2014**, *6*, 116.
[527] K.-C. Chen, C.-W. Liu, C. Chen, S.-Y. Lin, *Semicond. Sci. Technol.* **2019**, *34*, 045007.
[528] L. Zeng, D. Wu, J. Jie, X. Ren, X. Hu, S. P. Lau, Y. Chai, Y. H. Tsang, *Adv. Mater.* **2020**, *32*, 2004412.
[529] Z. Gan, E. Najafidehaghani, S. H. Han, S. Shradha, F. Abtahi, C. Neumann, J. Picker, T. Vogl, U. Hübner, F. Eilenberger, A. George, A. Turchanin, *Small Methods* **2022**, *6*, 2200300.
[530] H. H. Yoon, S. Jung, G. Choi, J. Kim, Y. Jeon, Y. S. Kim, H. Y. Jeong, K. Kim, S.-Y. Kwon, K. Park, *Nano Lett.* **2017**, *17*, 44.
[531] H. H. Yoon, W. Song, S. Jung, J. Kim, K. Mo, G. Choi, H. Y. Jeong, J. H. Lee, K. Park, *ACS Appl. Mater. Interfaces* **2019**, *11*, 47182.
[532] A. Allain, J. Kang, K. Banerjee, A. Kis, *Nat. Mater.* **2015**, *14*, 1195.
[533] D. S. Schulman, A. J. Arnold, S. Das, *Chem. Soc. Rev.* **2018**, *47*, 3037.
[534] Y. Wang, M. Chhowalla, *Nat. Rev. Phys.* **2022**, *4*, 101.
[535] Y. Wang, J. C. Kim, R. J. Wu, J. Martinez, X. Song, J. Yang, F. Zhao, A. Mkhoyan, H. Y. Jeong, M. Chhowalla, *Nature* **2019**, *568*, 70.
[536] S. Song, Y. Sim, S.-Y. Kim, J. H. Kim, I. Oh, W. Na, D. H. Lee, J. Wang, S. Yan, Y. Liu, J. Kwak, J.-H. Chen, H. Cheong, J.-W. Yoo, Z. Lee, S.-Y. Kwon, *Nat. Electron.* **2020**, *3*, 207.
[537] G. Kwon, Y.-H. Choi, H. Lee, H.-S. Kim, J. Jeong, K. Jeong, M. Baik, H. Kwon, J. Ahn, E. Lee, M.-H. Cho, *Nat. Electron.* **2022**, *5*, 241.
[538] A.-S. Chou, T. Wu, C.-C. Cheng, S.-S. Zhan, I.-C. Ni, S.-Y. Wang, Y.-C. Chang, S.-L. Liew, E. Chen, W.-H. Chang, C.-I. Wu, J. Cai, H.-S. P. Wong, H. Wang, in *2021 IEEE International Electron Devices Meeting (IEDM)*, IEEE, New York **2021**, pp. 7–2.
[539] J. Li, W. Liu, W. Zhou, J. Yang, H. Qu, Y. Hu, S. Zhang, *Phys. Rev. Appl.* **2022**, *17*, 054009.
[540] H. G. Kim, H.-B.-R. Lee, *Chem. Mater.* **2017**, *29*, 3809.
[541] E. Schilirò, S. Panasci, A. Mio, G. Nicotra, S. Agnello, B. Pecz, G. Z. Radnoczi, I. Deretzis, A. La Magna, F. Roccaforte, R. L. Nigro, F. Giannazzo, *Appl. Surf. Sci.* **2023**, *630*, 157476.
[542] M. Snure, S. R. Vangala, T. Prusnick, G. Grzybowski, A. Crespo, K. D. Leedy, *Sci. Rep.* **2020**, *10*, 14699.
[543] S. J. McDonnell, R. M. Wallace, *Jom* **2019**, *71*, 224.
[544] T. Li, T. Tu, Y. Sun, H. Fu, J. Yu, L. Xing, Z. Wang, H. Wang, R. Jia, J. Wu, C. Tan, Y. Liang, Y. Zhang, C. Zhang, Y. Dai, C. Qiu, M. Li, R. Huang, L. Jiao, K. Lai, B. Yan, P. Gao, H. Peng, *Nat. Electron.* **2020**, *3*, 473.
[545] S. Chang, J. H. Koo, J. Yoo, M. S. Kim, M. K. Choi, D.-H. Kim, Y. M. Song, *Chem. Rev.* **2024**, *124*, 768.
[546] S. Cai, X. Xu, W. Yang, J. Chen, X. Fang, *Adv. Mater.* **2019**, *31*, 1808138.
[547] C. Choi, M. K. Choi, S. Liu, M. Kim, O. K. Park, C. Im, J. Kim, X. Qin, G. J. Lee, K. W. Cho, M. Kim, E. Joh, J. Lee, D. Son, S.-H. Kwan, N. L. Jeon, Y. M. Song, N. Lu, D.-H. Kim, *Nat. Commun.* **2017**, *8*, 1664.
[548] Y. Sun, W. He, C. Jiang, J. Li, J. Liu, M. Liu, *Nano-Micro Lett.* **2025**, *17*, 1.
[549] J.-W. T. Seo, J. Zhu, V. K. Sangwan, E. B. Secor, S. G. Wallace, M. C. Hersam, *ACS Appl. Mater. Interfaces* **2019**, *11*, 5675.
[550] G. Hu, T. Albrow-Owen, X. Jin, A. Ali, Y. Hu, R. C. Howe, K. Shehzad, Z. Yang, X. Zhu, R. I. Woodward, T.-C. Wu, H. Jusssiila, J.-B. Wu, P. Peng, P.-H. Tan, Z. Sun, E. J. R. Kelleher, M. Zhang, Y. Xu, T. Hasan, *Nat. Commun.* **2017**, *8*, 278.
[551] M. Tweedie, C. Lau, L. Hou, X. Wang, Y. Sheng, J. Warner, *Mater. Today Adv.* **2020**, *6*, 100067.
[552] J. S. Austin, N. D. Cottam, C. Zhang, F. Wang, J. H. Gosling, O. Nelson-Dummet, T. S. James, P. H. Beton, G. F. Trindade, Y. Zhou, C. J. Tuck, R. Hague, O. Makarovsky, L. Turyanska, *Nanoscale* **2023**, *15*, 2134.

[553] H. Lee, W. Harden-Chaters, S. D. Han, S. Zhan, B. Li, S. Y. Bang, H. W. Choi, S. Lee, B. Hou, L. G. Occhipinti, J. M. Kim, *ACS Appl. Nano Mater.* **2020**, *3*, 4454.
[554] T. Dong, J. Sim oes, Z. Yang, *Adv. Mater. Interfaces* **2020**, *7*, 1901657.
[555] H. Cheng, J. Wu, M. Li, D.-H. Kim, Y.-S. Kim, Y. Huang, Z. Kang, K. Hwang, J. Rogers, *Appl. Phys. Lett.* **2011**, *98*, 6.
[556] E. Kim, C. Ko, K. Kim, Y. Chen, J. Suh, S.-G. Ryu, K. Wu, X. Meng, A. Suslu, S. Tongay, J. Wu, C. P. Grigoropoulos, *Adv. Mater* **2016**, *28*, 341.
[557] B. Cai, S. Zhang, Z. Yan, H. Zeng, *ChemNanoMat* **2015**, *1*, 542.
[558] T. Wehling, K. Novoselov, S. Morozov, E. Vdovin, M. Katsnelson, A. Geim, A. Lichtenstein, *Nano Lett.* **2008**, *8*, 173.
[559] H. Yoo, K. Heo, M. H. R. Ansari, S. Cho, *Nanomaterials* **2021**, *11*, 832.
[560] H. Ilatikhameneh, F. W. Chen, R. Rahman, G. Klimeck, in *2015 International Workshop on Computational Electronics (IWCE)*, IEEE, New York **2015**, pp. 1–3.
[561] Y. Shen, Z. Dong, Y. Sun, H. Guo, F. Wu, X. Li, J. Tang, J. Liu, X. Wu, H. Tian, T.-L. Ren, *Adv. Mater.* **2022**, *34*, 2201916.
[562] L. Su, Y. Zhang, Y. Yu, L. Cao, *Nanoscale* **2014**, *6*, 4920.
[563] Y. Wang, S. Sarkar, H. Yan, M. Chhowalla, *Nat. Electron.* **2024**, *7*, 638.
[564] J. Jadwiszczak, G. Li, C. P. Cullen, J. J. Wang, P. Maguire, G. S. Duesberg, J. G. Lunney, H. Zhang, *Appl. Phys. Lett.* **2019**, *114*, 9.
[565] B. Kirubasankar, Y. S. Won, L. A. Adofo, S. H. Choi, S. M. Kim, K. K. Kim, *Chem. Sci.* **2022**, *13*, 7707.
[566] Y. Huang, X. Zhou, L. Luo, J. Zou, H. Liu, X. Li, A. Ren, K. Shen, J. Wu, *Adv. Opt. Mater.* **2022**, *10*, 2200539.
[567] W. Huang, Y. Zhang, M. Song, B. Wang, H. Hou, X. Hu, X. Chen, T. Zhai, *Chin. Chem. Lett.* **2022**, *33*, 2281.
[568] W. H. P. Pernice, C. Xiong, C. Schuck, H. Tang, *Appl. Phys. Lett.* **2012**, *100*, 22.
[569] C.-S. Jao, H. Y. Lin, *Appl. Opt.* **2011**, *50*, 5139.
[570] X. Han, Y.-Y. Dai, P.-F. Ding, J. Xing, T.-M. Miao, Z.-Y. Sun, W.-T. Wang, D.-C. Zhang, J.-H. Yan, Y.-K. Zhang, D.-K. Rong, Z.-H. Guo, H. Chen, M.-T. Huang, J.-D. Zhou, L.-J. Du, B.-J. Feng, J.-G. Guo, G.-Y. Zhang, Y. Chai, Y. Huang, Y.-L. Wang, *Adv. Mater.* **2025**, 2417052.
[571] S. Li, J. Wang, M. Huang, *Small* **2025**, *21*, 2500628.
[572] A. N. Broers, A. Hoole, J. M. Ryan, *Microelectron. Eng.* **1996**, *32*, 131.
[573] C. Vieu, F. Carcenac, A. Pepin, Y. Chen, M. Mejias, A. Lebib, L. Manin-Ferlazzo, L. Couraud, H. Launois, *Appl. Surf. Sci.* **2000**, *164*, 111.
[574] D. A. Nguyen, S. Cho, S. Park, D. Y. Park, H. C. Suh, M. S. Jeong, T. P. A. Bach, H. Kim, H. Im, *Nano Energy* **2023**, *113*, 108552.
[575] A. Falin, Q. Cai, E. J. Santos, D. Scullion, D. Qian, R. Zhang, Z. Yang, S. Huang, K. Watanabe, T. Taniguchi, M. R. Barnett, Y. Chen, R. S. Ruoff, L. H. Li, *Nat. Commun.* **2017**, *8*, 15815.
[576] K. Zhang, Y. Feng, F. Wang, Z. Yang, J. Wang, *J. Mater. Chem. C* **2017**, *5*, 11992.
[577] K. Y. Ma, M. Kim, H. S. Shin, *Acc. Mater. Res.* **2022**, *3*, 748.
[578] Z. Ballard, C. Brown, A. M. Madni, A. Ozcan, *Nat. Mach. Intell.* **2021**, *3*, 556.
[579] Z. Zhang, L. Wang, C. Lee, *Adv. Sensor Res.* **2023**, *2*, 2200072.
[580] B. H. Stuart, *Infrared Spectroscopy: Fundamentals and Applications*, John Wiley & Sons, New Jersey **2004**.
[581] H.-H. Perkampus, *UV-VIS Spectroscopy and Its Applications*, Springer Science & Business Media, Berlin **2013**.
[582] J. Luypaert, D. Massart, Y. V. Heyden, *Talanta* **2007**, *72*, 865.
[583] L. Smeesters, F. Venturini, S. Paulus, A.-K. Mahlein, D. Perpetuini, D. Cardone, A. Merla, B. Gac, S. Perrin, D. Trégoat, L. Poffo, A. Fournier, G. Bonifazii, S. Serranti, W. Liao, N. Osseiran, M. Vanwolleghem, R. Peretti, A. Bandyopadhyay, K. Bertling, K. Parameswaran, A. D. Rákic, A. Sengupta, S. Svanberg, M. Kujawinska, D. Cozzolino, D. P. Marín, J. A. E. de León, I. Torres Rodríguez, M. Fodor, et al., *J. Phys.: Photonics* **2025**.
[584] K. B. Beć, J. Grabska, C. W. Huck, *Chem. Eur. J.* **2021**, *27*, 1514.
[585] A. Li, C. Yao, J. Xia, H. Wang, Q. Cheng, R. Penty, Y. Fainman, S. Pan, *Light: Sci. Appl.* **2022**, *11*, 174.
[586] Y. Zhang, E. Yang, H. H. Yoon, Q. Cheng, Z. Sun, T. Hasan, W. Cai, *eLight* **2025**, *5*, 23.
[587] L. Gao, Y. Qu, L. Wang, Z. Yu, *Nanophotonics* **2022**, *11*, 2507.
[588] S. Lee, H. Kim, S. Kim, H. Son, J. S. Han, U. J. Kim, *ACS Sens.* **2024**.
[589] D. S. Bhatti, J. Lee, C. Kim, Y. Choi, H. H. Yoon, H.-N. Lee, *Sci. Rep.* **2025**, *15*, 21232.
[590] W. Deng, Z. Zheng, J. Li, R. Zhou, X. Chen, D. Zhang, Y. Lu, C. Wang, C. You, S. Li, L. Sun, Y. Wu, X. Li, B. An, Z. Liu, Q. J. Wang, X. Duan, Y. Zhang, *Nat. Commun.* **2022**, *13*, 4627.
[591] H. Wang, S. Chen, X. Chen, *Nano Lett.* **2023**, *24*, 326.
[592] X. Cui, F. Nigmatulin, L. Wang, I. Reduto, A. C. Liapis, M. Du, M. G. Uddin, S. Abde Mayeen, F. Ahmed, Y. Zhang, H. H. Yoon, H. Lipsanen, S. Honkanen, T. Aalto, Z. Yang, T. Hasan, W. Cai, Z. Sun, *Sci. Adv.* **2025**, *11*, eado6886.
[593] W. Liang, X. Nan, W. Cai, N. Tan, Q. Zheng, Y. Lu, Y. Huang, J. Yan, D. Lei, L. Wen, Y. Liu, Q. Chen, *Adv. Sci.* **2025**, *12*, 2500830.
[594] L. Bian, Z. Wang, Y. Zhang, L. Li, Y. Zhang, C. Yang, W. Fang, J. Zhao, C. Zhu, Q. Meng, X. Peng, J. Zhang, *Nature* **2024**, *635*, 73.
[595] J. Zhang, R. Su, Q. Fu, W. Ren, F. Heide, Y. Nie, *Sci. Rep.* **2022**, *12*, 11905.
[596] U. J. Kim, S. Lee, H. Kim, Y. Roh, S. Han, H. Kim, Y. Park, S. Kim, M. J. Chung, H. Son, H. Choo, *Nat. Commun.* **2023**, *14*, 5262.
[597] L.-S. Chan, G. T. Cheung, I. J. Lauder, C. R. Kumana, *J. Travel Med.* **2004**, *11*, 273.
[598] V. Farley, A. Vallières, A. Villemaire, M. Chamberland, P. Lagueux, J. Giroux, in *Electro-Optical Remote Sensing, Detection, and Photonic Technologies and Their Applications*, vol. *6739*, SPIE, Bellingham, Washington, USA **2007**, pp. 334–345.
[599] E. Y.-k. Ng, R. U. Acharya, *IEEE Eng. Med. Biol. Mag.* **2009**, *28*, 76.
[600] A. Gholizadeh, L. Borvka, M. Saberioon, R. Vašát, *Appl. Spectrosc.* **2013**, *67*, 1349.
[601] C. A. T. Dos Santos, M. Lopo, R. N. Páscoa, J. A. Lopes, *Appl. Spectrosc.* **2013**, *67*, 1215.
[602] C. B. Pereira, X. Yu, M. Czaplik, R. Rossaint, V. Blazek, S. Leonhardt, *Biomed. Opt. Express* **2015**, *6*, 4378.
[603] T.-V. Dinh, I.-Y. Choi, Y.-S. Son, J.-C. Kim, *Sens. Actuators, B* **2016**, *231*, 529.
[604] N. Prieto, O. Pawluczyk, M. E. R. Dugan, J. L. Aalhus, *Appl. Spectrosc.* **2017**, *71*, 1403.
[605] R. K. Jha, *IEEE Sens. J.* **2021**, *22*, 6.
[606] S. Duan, J. Hu, X. Shi, M. Chen, Y. Wan, Y. Bai, H. Ma, T. Zhao, T. Xu, M. Yuan, Q. Zheng, Q. Li, Q. Wang, F. Zhong, Z. Wang, L. Liao, W. Hu, *ACS Photonics* **2025**, *12*, 6130.
[607] J. Li, X. Ge, J. Mi, H. Wang, J. Chen, R. He, F. Zhong, M. Zhan, C. Hu, Z. Wang, X. Zhou, X. Xu, Z. Xu, P. Martyniuk, A. Rogalski, F. Wang, P. Wang, Z. Liu, Q. Li, L. Li, W. Hu, *Nat. Commun.* **2025**, *16*, 8904.
[608] Y. Dong, S. Duan, S. Long, Y. Jiang, X. Ma, Y. Fang, J. Liu, H. Wu, T. Li, X. Jiang, S. Chen, S. Hu, X. Fu, X. Chen, F. Chen, J. Miao, W. Hu, *Adv. Funct. Mater.* **2025**, *35*, 2422398.
[609] X. Tan, H. Zhang, J. Li, H. Wan, Q. Guo, H. Zhu, H. Liu, F. Yi, *Nat. Commun.* **2020**, *11*, 5245.
[610] Y. Fan, W. Huang, F. Zhu, X. Liu, C. Jin, C. Guo, Y. An, Y. Kivshar, C.-W. Qiu, W. Li, *Nature* **2024**, *630*, 77.
[611] T. Tahara, X. Quan, R. Otani, Y. Takaki, O. Matoba, *Microscopy* **2018**, *67*, 55.
[612] C.-Y. Wang, S.-J. Liang, S. Wang, P. Wang, Z. Li, Z. Wang, A. Gao, C. Pan, C. Liu, J. Liu, H. Yang, X. Liu, W. Song, C. Wang, B. Cheng, X. Wang, K. Chen, Z. Wang, K. Watanabe, T. Taniguchi, J. J. Yang, F. Miao, *Sci. Adv.* **2020**, *6*, eaba6173.

[613] P. Wu, T. He, H. Zhu, Y. Wang, Q. Li, Z. Wang, X. Fu, F. Wang, P. Wang, C. Shan, Z. Fan, L. Liao, P. Zhou, W. Hu, *InfoMat* **2022**, *4*, 12275.
[614] Z. Wang, T. Wan, S. Ma, Y. Chai, *Nat. Nanotechnol.* **2024**, *19*, 919.
[615] G. Gou, Z. Li, X. Xu, H. Wang, H. Gu, L. Gao, T. Zhai, X. Zhou, *Small* **2025**, 2504001.
[616] R. Zhang, S. Zhu, J. Mei, J. Wu, Y. Liu, Y. Chen, J. Meng, X. Cai, *ACS Appl. Mater. Interfaces* **2024**, *16*, 66655.
[617] J. Xiong, Q. Yu, B. Liu, S. Li, Y. Luo, J. Li, J. Zhang, J. Wu, Z. Yang, J. Leng, Y. Sun, Z. Jiang, N. Huo, P. Zhou, *Adv. Funct. Mater.* **2025**, *35*, 2423280.
[618] X. Ma, Z. Wang, Q. Qin, J. Chen, X. Liu, F. Zou, Z. Xu, W. Chen, G. Li, Y. Li, T. Zhaii, L. Li, *Adv. Mater.* **2025**, *37*, 2500572.
[619] W. Liu, J. Lv, L. Peng, H. Guo, C. Liu, Y. Liu, W. Li, L. Li, L. Liu, P. Wang, S. C. Bodequdi, K. Shehzad, G. Hu, K. Liu, Z. Sun, T. Hasan, Y. Xu, X. Wang, C. Gao, B. Yu, X. Duan, *Nat. Electron.* **2022**, *5*, 281.
[620] P. Wu, L. Ye, L. Tong, P. Wang, Y. Wang, H. Wang, H. Ge, Z. Wang, Y. Gu, K. Zhang, Y. Yu, M. Peng, F. Wang, M. Huang, P. Zhou, W. Hu, *Light: Sci. Appl.* **2022**, *11*, 6.
[621] G. Wu, M. Abid, M. Zerara, J. Cho, M. Choi, C. Ó Coileáin, K.-M. Hung, C.-R. Chang, I. V. Shvets, H.-C. Wu, *Nat. Commun.* **2024**, *15*, 676.
[622] F. Tang, J. Wu, T. Albrow-Owen, H. Cui, F. Chen, Y. Shi, L. Zou, J. Chen, X. Guo, Y. Sun, J. Luo, B. Ju, J. Huang, S. Liu, B. Li, L. Yang, E. A. Munro, W. Zheng, H. J. Joyce, H. Chen, L. Che, S. Dong, Z. Sun, T. Hasan, X. Ye, Y. Yang, Z. Yang, *Sci. Adv.* **2024**, *10*, eadr7155.
[623] M. Bertozzi, A. Broggi, A. Fascioli, *Rob. Auton. Syst.* **2000**, *32*, 1.
[624] Y. Ding, Y. Yang, H. Hao, Z.-A. Li, C. Pan, P. Wang, C. Wang, H. Tan, R. Jin, J. Zhang, S. Du, S.-J. Liang, F. Miao, W. Yang, *ACS Nano* **2025**, *19*, 22376.
[625] Y. Yang, C. Pan, Y. Li, X. Yangdong, P. Wang, Z.-A. Li, S. Wang, W. Yu, G. Liu, B. Cheng, Z. Di, S. -J. Liang, F. Miao, *Nat. Electron.* **2024**, *7*, 225.
[626] Y. Hu, Z. Gao, Z. Luo, L. An, *Adv. Mater.* **2025**, *37*, 2501123.
[627] M. Amer, T. Maul, *Artificial Intell. Rev.* **2019**, *52*, 527.
[628] Y. LeCun, Y. Bengio, G. Hinton, *Nature* **2015**, *521*, 436.
[629] Y. Chai, *Nature* **2020**, *579*, 32.
[630] A. Pospischil, M. M. Furchi, T. Mueller, *Nat. Nanotechnol.* **2014**, *9*, 257.
[631] B. W. Baugher, H. O. Churchill, Y. Yang, P. Jarillo-Herrero, *Nat. Nanotechnol.* **2014**, *9*, 262.
[632] J. S. Ross, P. Klement, A. M. Jones, N. J. Ghimire, J. Yan, D. Mandrus, T. Taniguchi, K. Watanabe, K. Kitamura, W. Yao, D. H. Cobden, X. Xu, *Nat. Nanotechnol.* **2014**, *9*, 268.
[633] Y. Yu, M. Zhong, T. Xiong, J. Yang, P. Hu, H. Long, Z. Zhou, K. Xin, Y.-Y. Liu, J. Yang, J. Qiao, D. Liu, Z. Wei, *Adv. Sci.* **2024**, *11*, 2309781.
[634] P.-Y. Huang, B.-Y. Jiang, H.-J. Chen, J.-Y. Xu, K. Wang, C.-Y. Zhu, X.-Y. Hu, D. Li, L. Zhen, F.-C. Zhou, J.-K. Qin, C.-Y. Xu, *Nat. Commun.* **2023**, *14*, 6736.
[635] D. N. Neshev, A. E. Miroshnichenko, *Nat. Photonics* **2023**, *17*, 26.
[636] C. Choi, G. J. Lee, S. Chang, Y. M. Song, D.-H. Kim, *ACS Nano* **2024**, *18*, 1241.
[637] S. Yuan, C. Ma, E. Fetaya, T. Mueller, D. Naveh, F. Zhang, F. Xia, *Science* **2023**, *379*, eade1220.
[638] L. Xu, J. Liu, X. Guo, S. Liu, X. Lai, J. Wang, M. Yu, Z. Xie, H. Peng, X. Zou, X. Wang, R. Huang, M. He, *Nat. Commun.* **2024**, *15*, 9011.
[639] F. Wang, F. Hu, M. Dai, S. Zhu, F. Sun, R. Duan, C. Wang, J. Han, W. Deng, W. Chen, M. Ye, S. Han, B. Qiang, Y. Jin, Y. Chi, S. Yu, D. Nam, S. H. Chae, Z. Liu, Q. J. Wang, *Nat. Commun.* **2023**, *14*, 1938.
[640] G. Currie, K. E. Hawk, E. Rohren, A. Vial, R. Klein, *J. Medical Imaging Radiation Sci.* **2019**, *50*, 477.
[641] M. Wang, K. C. Lee, B. M. Chung, S. V. Bogaraju, H.-C. Ng, J. S. Wong, H. C. Shum, K. K. Tsia, H. K.-H. So, *IEEE Trans. Neural Networks Learn. Syst.* **2021**, *33*, 2853.
[642] R. Song, K. Huang, Z. Wang, H. Shen, *IEEE Trans. Circuits Syst. Video Technol.* **2022**, *32*, 7212.
[643] S. Lee, R. Peng, C. Wu, M. Li, *Nat. Commun.* **2022**, *13*, 1485.
[644] T. Xu, F. Zhong, P. Wang, Z. Wang, X. Ge, J. Wang, H. Wang, K. Zhang, Z. Zhang, T. Zhao, Y. Yu, M. Luo, Y. Wang, R. Jiang, F. Wang, F. Chen, Q. Liu, W. Hu, *Sci. Adv.* **2024**, *10*, eadn0560.
[645] Z. Wu, J. Peng, H. Zheng, J. Li, Y. Lin, H. Dong, J. Fan, Z. Zheng, W. Li, *Adv. Mater.* **2025**, *37*, 2507636.
[646] L. Pi, P. Wang, S.-J. Liang, P. Luo, H. Wang, D. Li, Z. Li, P. Chen, X. Zhou, F. Miao, T. Zhai, *Nat. Electron.* **2022**, *5*, 248.
[647] Y. Zhao, L. Gong, Y. Huang, C. Liu, *Comput. Electron. Agric.* **2016**, *127*, 311.
[648] N. Li, S. Zhang, Y. Peng, X. Li, Y. Zhang, C. He, G. Zhang, *Adv. Funct. Mater.* **2023**, *33*, 2305589.
[649] F. Liao, Z. Zhou, B. J. Kim, J. Chen, J. Wang, T. Wan, Y. Zhou, A. T. Hoang, C. Wang, J. Kang, J.-H. Ahn, *Nat. Electron.* **2022**, *5*, 84.
[650] S. Lee, H. Kim, G. Kim, H. Son, U. J. Kim, *Adv. Mater. Technol.* **2025**, *10*, 2400671.
[651] X. Sun, Z. Lin, Y. Xu, H. Wu, C. Tan, H. Cui, G. Hu, Z. Wang, *Adv. Funct. Mater.* **2025**, 15090.
[652] X. Feng, C. Li, J. Song, Y. He, W. Qu, W. Li, K. Guo, L. Liu, B. Yang, H. Wei, *Nat. Commun.* **2024**, *15*, 577.
[653] T. Park, Y. Han, S. Lee, Y.-H. Kim, H. Yoo, *Nano Lett.* **2024**, *24*, 9544.
[654] J. H. Kim, J. Lee, H. Kim, S. J. Yun, J. Kim, H. S. Lee, Y. H. Lee, *Sci. Rep.* **2019**, *9*, 9164.
[655] Y. Zhang, Y. Wang, Y. Dai, X. Bai, X. Hu, L. Du, H. Hu, X. Yang, D. Li, Q. Dai, T. Hansan, Z. Sun, *Sci. Adv.* **2022**, *8*, eabq8246.
[656] M. M. Islam, A. Krishnaprasad, D. Dev, R. Martinez-Martinez, V. Okonkwo, B. Wu, S. S. Han, T.-S. Bae, H.-S. Chung, J. Touma, Y. Jung, T. Roy, *ACS Nano* **2022**, *16*, 10188.
[657] S. Seo, S.-H. Jo, S. Kim, J. Shim, S. Oh, J.-H. Kim, K. Heo, J.-W. Choi, C. Choi, S. Oh, D. Kuzum, H.-S. P. Wong, J.-H. Park, *Nat. Commun.* **2018**, *9*, 5106.
[658] Y. Wang, X. Li, Z. Jiang, L. Tong, W. Deng, X. Gao, X. Huang, H. Zhou, Y. Yu, L. Ye, X. Xiao, *Nat. Commun.* **2021**, *12*, 5076.
[659] N. Abraham, K. Watanabe, T. Taniguchi, K. Majumdar, *Adv. Funct. Mater.* **2024**, *34*, 2406510.
[660] F. Zhou, Y. Chai, *Nat. Electron.* **2020**, *3*, 664.
[661] T. Guo, B. Zhang, X. Wang, Y. Xiao, B. Sun, Y. N. Zhou, Y. A. Wu, *Adv. Funct. Mater.* **2023**, *33*, 2303879.
[662] Q. Ren, C. Zhu, S. Ma, Z. Wang, J. Yan, T. Wan, W. Yan, Y. Chai, *Adv. Mater.* **2024**, *37*, 2407476.
[663] Y. Shi, N. T. Duong, K.-W. Ang, *Nanoscale Horiz.* **2025**, *10*, 205.
[664] G. Zhang, Q. Luo, J. Yao, S. Zhong, H. Wang, F. Xue, B. Yu, K. P. Loh, Y. Zhang, *Chem. Soc. Rev.* **2025**, *54*, 8196.
[665] K. Kwak, J. B. An, I. S. Lee, Y. S. Hwang, H. J. Son, H. J. Kim, *Device* **2025**, *3*, 100900.
[666] T. Wan, B. Shao, S. Ma, Y. Zhou, Q. Li, Y. Chai, *Adv. Mater.* **2023**, *35*, 2203830.
[667] Y. Xu, X. Xu, Y. Huang, Y. Tian, M. Cheng, J. Deng, Y. Xie, Y. Zhang, P. Zhang, X. Wang, Z. Wang, M. Li, L. Li, M. Liu, *Adv. Mater.* **2024**, *36*, 2402903.
[668] Y. Zhu, Y. Wang, X. Pang, Y. Jiang, X. Liu, Q. Li, Z. Wang, C. Liu, W. Hu, P. Zhou, *Nat. Commun.* **2024**, *15*, 6015.
[669] P. Wang, J. Li, W. Xue, W. Ci, F. Jiang, L. Shi, F. Zhou, P. Zhou, X. Xu, *Adv. Sci.* **2024**, *11*, 2305679.
[670] A. Abubakar, B. Wang, A. Bermak, in *2024 Int. Conf. on Microelectronics (ICM)*, IEEE, New York **2024**, pp. 1–6.
[671] P. Wakale, B. Dierickx, F. Tavernier, *J. Instrum.* **2025**, *20*, C08003.

[672] C. Choi, G. J. Lee, S. Chang, Y. M. Song, D.-H. Kim, *Adv. Mater.* **2024**, *36*, 2412252.
[673] Y. Wang, L. Yin, W. Huang, Y. Li, S. Huang, Y. Zhu, D. Yang, X. Pi, *Adv. Intell. Syst.* **2021**, *3*, 2000099.
[674] M. Zhou, Y. Zhao, X. Gu, Q. Zhang, J. Zhang, M. Jiang, S. Lu, *APL Photonics* **2023**, *8*, 7.
[675] G. S. Syed, Y. Zhou, J. Warner, H. Bhaskaran, *Nat. Nanotechnol.* **2023**, *18*, 1036.
[676] H. Li, J. Hu, Y. Zhang, A. Chen, J. Zhou, Y. Zhao, Y. Xu, B. Yu, *Adv. Funct. Mater.* **2024**, *34*, 2314456.
[677] M. Chen, Y. Ma, N. Aslam, C. Liu, Y. Chen, L. Luo, X. Zhang, K. Mai, H. Xiao, K. Zhu, O. Alharbi, D. Zheng, X. Xu, H. Liao, Y. Yang, H. Wang, Z. Zhou, H. Wang, B. Tian, J. Li, X. He, K. Chang, Y. Wan, A. Shamim, H. N. Alshareef, M. Lanza, T. D. Anthopoulos, Z. Han, F. Xue, X. Zhang, *Nat. Nanotechnol.* **2025**, *20*, 1633.
[678] C.-Y. Wang, C. Wang, F. Meng, P. Wang, S. Wang, S.-J. Liang, F. Miao, *Adv. Electron. Mater.* **2020**, *6*, 1901107.
[679] L. El Srouji, A. Krishnan, R. Ravichandran, Y. Lee, M. On, X. Xiao, S. Ben Yoo, *APL Photonics* **2022**, *7*, 5.
[680] A. Wali, S. Das, *Adv. Funct. Mater.* **2024**, *34*, 2308129.
[681] S. Hadke, M.-A. Kang, V. K. Sangwan, M. C. Hersam, *Chem. Rev.* **2025**, *125*, 835.
[682] X. Yu, C. Cheng, J. Liang, M. Wang, B. Huang, Z. Wang, L. Li, *Adv. Funct. Mater.* **2024**, *34*, 2312481.
[683] S. Mukherjee, D. Dutta, A. Ghosh, E. Koren, *ACS Nano* **2023**, *17*, 22287.
[684] Y. Li, Y. Zhang, Y. Wang, J. Sun, Q. You, M. Zhu, L. Li, T. Deng, *Adv. Funct. Mater.* **2024**, *34*, 2302288.
[685] Y. Deng, S. Liu, X. Ma, S. Guo, B. Zhai, Z. Zhang, M. Li, Y. Yu, W. Hu, H. Yang, Y. Kapitonov, J. Han, J. Wu, Y. Li, T. Zhai, *Adv. Mater.* **2024**, *36*, 2309940.
[686] Z. Yang, S. Huo, Z. Zhang, F. Meng, B. Liu, Y. Wang, Y. Ma, Z. Wang, J. Xu, Q. Tian, Y. Wang, Y. Ding, X. Hu, Y. Xie, S. Fan, C. Pan, E. Wu, *Adv. Funct. Mater.* **2025**, 2509119.
[687] K. Liu, T. Zhu, Y. Tang, Y. Zhang, Y. Gu, Y. Zhang, J. Xing, Y. Dong, B. Feng, X. Li, L. Zhang, M. Jiang, H. Xu, *Adv. Funct. Mater.* **2025**, 09982.
[688] S. Shim, S. Kim, D. Lee, H. Kim, M. J. Kwon, S.-y. Cho, W. A. Lestari, J. Seo, D. Yeo, J. Na, S. S. Kundale, N. Oh, J. H. Park, *Small* **2025**, *21*, 2410892.
[689] B. Pan, L. Zhang, S. Lan, Y. Hong, J. Liang, L. Deng, T. Taniguchi, K. Watanabe, X. Gao, J.-L. Xu, Y.-N. Zhong, J. Miao, Y. Ye, L.-J. Li, S. Wang, W. Hu, S.-D. Wang, P. Wang, *Adv. Funct. Mater.* **2025**, *35*, 2421337.
[690] L. Tong, Y. Bi, Y. Wang, K. Peng, X. Huang, W. Ju, Z. Peng, Z. Li, L. Xu, R. Lin, X. Yu, W. Shi, H. Yu, H. Sun, K. Xue, Q. He, M. Tang, J. Xu, X. Zhang, J. Miao, D. Jariwala, W. Bao, X. Miao, P. Wang, L. Ye, *Nat. Commun.* **2024**, *15*, 10290.
[691] I. Bente, S. Taheriniya, F. Lenzini, F. Brückerhoff-Plückelmann, M. Kues, H. Bhaskaran, C. D. Wright, W. Pernice, *Nat. Rev. Phys.* **2025**, *7*, 439.
[692] A. Autere, H. Jussila, Y. Dai, Y. Wang, H. Lipsanen, Z. Sun, *Adv. Mater.* **2018**, *30*, 1705963.
[693] Y. Wang, F. Iyikanat, X. Bai, X. Hu, S. Das, Y. Dai, Y. Zhang, L. Du, S. Li, H. Lipsanen, F. J. G. d. Abajo, Z. Sun, *Nano Lett.* **2022**, *22*, 8455.
[694] L. J. Maczewsky, M. Heinrich, M. Kremer, S. K. Ivanov, M. Ehrhardt, F. Martinez, Y. V. Kartashov, V. V. Konotop, L. Torner, D. Bauer, A. Szameit, *Science* **2020**, *370*, 701.
[695] M. S. Kirsch, Y. Zhang, M. Kremer, L. J. Maczewsky, S. K. Ivanov, Y. V. Kartashov, L. Torner, D. Bauer, A. Szameit, M. Heinrich, *Nat. Phys.* **2021**, *17*, 995.
[696] D. Smirnova, D. Leykam, Y. Chong, Y. Kivshar, *Appl. Phys. Rev.* **2020**, *7*, 2.
[697] S. Parhizkar, M. Prechtl, A. L. Giesecke, S. Suckow, S. Wahl, S. Lukas, O. Hartwig, N. Negm, A. Quellmalz, K. Gylfason, D. Schall, M. Wuttig, G. S. Duesberg, M. C. Lemme, *ACS Photonics* **2022**, *9*, 859.
[698] W. Bogaerts, L. Chrostowski, *Laser Photonics Rev.* **2018**, *12*, 1700237.
[699] C. Li, R. Tian, X. Chen, L. Gu, Z. Luo, Q. Zhang, R. Yi, Z. Li, B. Jiang, Y. Liu, A. Castellanos-Gomez, S.-J. Chua, X. Wang, Z. Sun, J. Zhao, X. Gan, *ACS Nano* **2022**, *16*, 20946.
[700] C. Yang, Z. Liu, H. Cai, D. Li, Y. Yu, X. Zhang, *ACS Nano* **2025**, *19*, 8661.
[701] D. J. Moss, R. Morandotti, A. L. Gaeta, M. Lipson, *Nat. Photonics* **2013**, *7*, 597.
[702] S. Zhu, Y. Zhang, Y. Ren, Y. Wang, K. Zhai, H. Feng, Y. Jin, Z. Lin, J. Feng, S. Li, Q. Yang, N. H. Zhu, E. Y.-B. Pun, C. Wang, *Adv. Photonics Res.* **2023**, *4*, 2300045.
[703] H. Zhao, S. Pinna, B. Song, L. Megalini, S. T. Š. Brunelli, L. A. Coldren, J. Klamkin, *IEEE J. Sel. Top. Quantum Electron.* **2018**, *24*, 1.
[704] T. He, H. Ma, Z. Wang, Q. Li, S. Liu, S. Duan, T. Xu, J. Wang, H. Wu, F. Zhong, P. Martyniuk, A. Rogalski, P. Wang, L. Li, H. Lin, W. Hu, *Nat. Photonics* **2024**, *18*, 60.
[705] X. Cui, M. Du, S. Das, H. H. Yoon, V. Y. Pelgrin, D. Li, Z. Sun, *Nanoscale* **2022**, *14*, 9459.
[706] F. Li, J. Zheng, Q. Yao, Y.-Q. Bie, *Opt. Mater. Express* **2021**, *11*, 3298.
[707] P.-L. Chen, T. Ahmed, C. Kuo, C.-C. Lu, D.-H. Lien, C.-H. Liu, *Small Methods* **2024**, *9*, 2401550.
[708] A. Zalogina, C. Li, I. Zhigulin, N. Coste, H. Alijani, O. C. Schaeper, H. Charlton, J. Ward, H. Ren, I. Aharonovich, *ACS Photonics* **2025**, *12*, 3901.
[709] C. Sun, M. T. Wade, Y. Lee, J. S. Orcutt, L. Alloatti, M. S. Georgas, A. S. Waterman, J. M. Shainline, R. R. Avizienis, S. Lin, B. R. Moss, R. Kumar, F. Pavanello, A. H. Atabaki, H. M. Cook, A. J. Ou, J. C. Leu, Y.-H. Chen, K. Asanović, R. J. Ram, M. A. Popović, V. M. Stojanović, *Nature* **2015**, *528*, 534.
[710] A. H. Atabaki, S. Moazeni, F. Pavanello, H. Gevorgyan, J. Notaros, L. Alloatti, M. T. Wade, C. Sun, S. A. Kruger, H. Meng, K. A. Qubaisi, I. Wang, B. Zhang, A. Khilo, C. V. Baiocco, M. A. Popović, V. M. Stojanović, R. J. Ram, *Nature* **2018**, *556*, 349.
[711] S. Shekhar, W. Bogaerts, L. Chrostowski, J. E. Bowers, M. Hochberg, R. Soref, B. J. Shastri, *Nat. Commun.* **2024**, *15*, 751.
[712] S. Daudlin, A. Rizzo, S. Lee, D. Khilwani, C. Ou, S. Wang, A. Novick, V. Gopal, M. Cullen, R. Parsons, K. Jang, A. Molnar, K. Bergman, *Nat. Photonics* **2025**, *19*, 1.
[713] C. A. Brackett, *IEEE J. Sel. Areas Commun.* **1990**, *8*, 948.
[714] M. Wade, E. Anderson, S. Ardalan, W. Bae, B. Beheshtian, S. Buchbinder, K. Chang, P. Chao, H. Eachempatti, J. Frey, E. Jan, A. Katzin, A. Khilo, D. Kita, U. Krishnamoorthy, C. Li, H. Lu, F. Luna, C. Madden, L. Okada, M. Patel, C. Ramamurthy, M. Raval, R. Roucka, K. Robberson, et al., in *Optical Fiber Communication Conference*, Optica Publishing Group, Washington, DC **2021**, pp. F3C–6.
[715] M. Wade, E. Anderson, S. Ardalan, P. Bhargava, S. Buchbinder, M. L. Davenport, J. Fini, H. Lu, C. Li, R. Meade, C. Ramamurthy, M. Rust, F. Sedgwick, V. Stojanovic, D. V. Orden, C. Zhang, C. Sun, S. Y. Shumarayev, C. O'Keeffe, T. T. Hoang, D. Kehlet, R. V. Mahajan, M. T. Guzy, A. Chan, T. Tran, *IEEE Micro* **2020**, *40*, 63.
[716] K. Hosseini, E. Kok, S. Y. Shumarayev, D. Jeong, A. Chan, A. Katzin, S. Liu, R. Roucka, M. Raval, M. Mac, C.-P. Chiu, T. Tran, K. A. Singh, S. Raman, Y. Ke, C. Li, L.-F. Yang, P. Chao, H. Lu, F. Luna, X. Li, T. T. Hoang, A. Sarkar, A. Toda, R. Mahajan, N. Deshpande, C. O'Keeffe, U. Krishnamoorthy, V. Stojanovic, C. Madden, et al., in *2022 IEEE Symposium on VLSI Technology and Circuits (VLSI Technology and Circuits)*, IEEE, New York **2022**, pp. 260–261.
[717] B. Pezeshki, F. Khoeini, A. Tselikov, R. Kalman, C. Danesh, E. Afifi, in *Optical Fiber Communication Conference*, Optica Publishing Group, Washington, DC **2022**, pp. W1E–1.

[718] F. Khoeini, B. Pezeshki, E. Afifi, A. Tselikov, R. F. Kalman, B. Hadidian, E. Afshari, *IEEE J. Solid-State Circuits* **2023**, *59*, 1578.
[719] B. Pezeshki, in *2024 IEEE Silicon Photonics Conference (SiPhotonics)*, IEEE, New York **2024**, pp. 1–2.
[720] F. Testa, M. T. Wade, M. Lostedt, F. Cavaliere, M. Romagnoli, V. Stojanović, *J. Lightwave Technol.* **2021**, *40*, 393.
[721] N. Flöry, P. Ma, Y. Salamin, A. Emboras, T. Taniguchi, K. Watanabe, J. Leuthold, L. Novotny, *Nat. Nanotechnol.* **2020**, *15*, 118.
[722] R. Maiti, C. Patil, M. Saadi, T. Xie, J. Azadani, B. Uluutku, R. Amin, A. Briggs, M. Miscuglio, D. Van Thourhout, S. D. Solares, T. Low, R. Agarwal, S. R. Bank, V. J. Sorger, *Nat. Photonics* **2020**, *14*, 578.
[723] P. Zhang, Q. Liang, Q. Zhou, J. Chen, M. Li, Y. Deng, W. Liang, L. Zhang, Q. Zhang, L. Gu, C. Ge, K.-j Jin, C. Zhang, G. Yang, *Light: Sci. Appl.* **2024**, *13*, 67.
[724] D. Shahwar, H. H. Yoon, S.-T. Akkanen, D. Li, S. t. Muntaha, M. Cherchi, T. Aalto, Z. Sun, *npj Nanophotonics* **2024**, *1*, 35.
[725] B. Carey, N. K. Wessling, P. Steeger, R. Schmidt, S. Michaelis de Vasconcellos, R. Bratschitsch, A. Arora, *Nat. Commun.* **2024**, *15*, 3082.
[726] Z. Liu, M. Liu, L. Qi, N. Zhang, B. Wang, X. Sun, R. Zhang, D. Li, S. Li, *Light: Sci. Appl.* **2025**, *14*, 68.
[727] N. Youngblood, M. Li, *Nanophotonics* **2017**, *6*, 1205.
[728] W. Jie, Z. Yang, G. Bai, J. Hao, *Adv. Opt. Mater.* **2018**, *6*, 1701296.
[729] J. G. Marin, D. Unuchek, K. Watanabe, T. Taniguchi, A. Kis, *npj 2D Mater. Appl.* **2019**, *3*, 14.
[730] L. Cheng, X. Qin, A. T. Lucero, A. Azcatl, J. Huang, R. M. Wallace, K. Cho, J. Kim, *ACS Appl. Mater. Interfaces* **2014**, *6*, 11834.

Junheon Ha received his B.S. in Electrical Engineering from Incheon National University in 2025 and joined the Department of Semiconductor Engineering at Gwangju Institute of Science and Technology in the same year to pursue his M.S. studies. His research interests lie in 2D materials for artificial intelligence sensors, infrared photodetectors, nanophotonics, and their applications in non-contact remote gas sensing and on-site drug screening.

Yingshan Ma received her B.S. degree in Applied Physics from Hebei University in 2023 and joined the School of Integrated Circuits and Electronics at Beijing Institute of Technology to pursue an integrated M.S.-Ph.D. course. Her research interests focus on nonlinear optics, fabrication and characterization of novel semiconductor materials, and investigation of their physical properties.

Yong Nam An received his B.S. degree in Materials Science and Engineering from Inha University in 2023. He worked on thin film process development and semiconductor equipment evaluation in the CVD/ALD team at ULVAC Korea Institute of Advanced Technology. He then joined the Department of Semiconductor Engineering at Gwangju Institute of Science and Technology in 2025 to pursue an integrated M.S.-Ph.D. program. His research interests include the growth and electrical characterization of 2D topological semimetals, as well as the industrial implementation of ultra-low-k dielectrics.

Sung- Un An received his B.S. degree in Physics from Chungnam National University in 2023 and joined the Department of Electrical Engineering and Computer Science at Gwangju Institute of Science and Technology in the same year to pursue an integrated M.S.-Ph.D. course. His research interests include band structure engineering, light-induced doping, lithography, and their applications in the nanoscale fabrication of 2D materials-based electronic and optoelectronic devices.

Dong-Ho Kang received his Ph.D. degree in Electrical Engineering from Sungkyunkwan University in 2019 and served as a postdoctoral researcher at Nanyang Technological University from 2019 to 2021. He then joined the Department of Semiconductor Engineering (Full) and Department of Electrical Engineering and Computer Science (Adjunct) at Gwangju Institute of Science and Technology in 2021 as an Assistant Professor. His research focuses on 2D materials-based in-memory computing, neuromorphic computing, and advanced photonic applications.

Hyeon-Jin Shin received her M.S. degree in Chemistry from Korea University in 2002 and her Ph.D. in Nano Science from Sungkyunkwan University in 2010. She worked as a Principal Researcher and Project Leader for 2D materials research at the Samsung Advanced Institute of Technology, Samsung Electronics, from 2002 to 2023. She joined the Department of Semiconductor Engineering (Full) and Department of Electrical Engineering and Computer Science (Adjunct) at Gwangju Institute of Science and Technology in 2023 as an Associate Professor. Her research focuses on the science and technology of next-generation integrated semiconductor devices based on 2D materials, including graphene, transition metal dichalcogenides, boron nitride, and topological insulators. Scientifically, she investigates advanced growth techniques, novel material properties, and new device concepts. Technologically, she develops high-performance, CMOS-compatible integration processes that enable seamless transition from lab-scale demonstrations to industrial manufacturing.

Yunyun Dai obtained her Ph.D. in Condensed Matter Physics from Fudan University in 2017. She worked as a visiting scholar at the Technical University of Denmark in 2014 and as a Postdoctoral Researcher at the Department of Electronics and Nanoengineering, Aalto University from 2017 to 2021. She joined the Beijing Institute of Technology in 2022 as an Associate Professor and was promoted to Professor the same year. She received the E. Fermi Scholarship at the International School of Quantum Physics from the Italian Physical Society in 2018, the LaserLab-Europe funding from the European Union's Horizon 2020 in 2019, and funding for the research project as a host from the National Natural Science Foundation of China in 2024. The Chinese government recognized her as a National Outstanding Young Talent in 2022. Her research interests include nanophotonics, nonlinear optics, ultrafast optics, and plasmonics of 2D materials.

Hoon Hahn Yoon double majored in Device Physics & Mechanical System Design and Manufacturing for his B.S. degree from the Ulsan National Institute of Science and Technology and delivered the graduation speech as a valedictorian at the commencement ceremony in 2014. He received his Ph.D. in Physics from the same university in 2020. He worked as an Intern Researcher at the Single-Electron Quantum Device Team, Quantum Technology Institute, Korea Research Institute of Standards and Science in 2012, a Postdoctoral Researcher at the Department of Physics, Ulsan National Institute of Science and Technology in 2020, a Postdoctoral Researcher at the Department of Electronics and Nanoengineering, Aalto University from 2020 to 2022, and a Staff Engineer at the Device Part, Process Architecture Team, Foundry Business Department, Samsung Electronics from 2022 to 2023. He then joined the Department of Semiconductor Engineering (Full) and Department of Electrical Engineering and Computer Science (Adjunct) at the Gwangju Institute of Science and Technology in 2023 as an Assistant Professor. He was awarded the Global Ph.D. Fellowship from the National Research Foundation of Korea in 2015, the Academy Research Fellowship from the Academy of Finland in 2022, and the 2DM Emerging Young Scientists Award from the Journal *2D Materials* by IOP Publishing in 2025. His research interests focus on 2D materials for artificial intelligence sensors, more than Moore devices, electron quantum optics, and quantum phase transitions.